Effect of Pore Diameter Variation of Fe-W/SBA-15 Supported Catalysts on Hydrotreating of Heavy Gas Oil from Athabasca Bitumen

A Thesis submitted to the College of Graduate Studies & Research

in Partial Fulfillment of the requirements for the

Degree of Master of Science

in the Department of Chemical Engineering,

University of Saskatchewan

Saskatoon, SK

By

Philip Effah Boahene

April, 2011

COPYRIGHT

Abstract

The pore diameter of a catalyst support controls the diffusion of reactant molecules to the catalytic active sites; thus, affecting the rates and conversions of the hydrotreating reactions. Desirable textural properties of SBA-15 makes it a potential alternative to the conventionally used γ-Al_2O_3 support due to the fact that its pore size can be manipulated via controlling the synthesis parameters, while maintaining relatively high surface area. Larger pore diameter SBA-15 supports may facilitate the diffusion of bulky molecules as that of the asphaltenes present in the heavy petroleum fractions, making it a potential catalyst support for hydrotreating operations.

Considering the very sour nature of Canada's bitumen with high sulfur contents in the range of 2-6 wt %, the appreciably high sulfur contents particularly present in Athabasca derived heavy gas oils (about 4 wt % sulfur), the rising demand for cleaner fuels, and also the increasing stringency on environmental standards, the need for novel and improved hydrotreating catalysts cannot be overemphasized. By varying the molar ratio of hexane to ammonium fluoride, the pore channels of SBA-15 could be varied. Controlling the pore diameter of these supports via micelle swelling facilitated the production of larger pore diameter SBA-15-supported catalysts.

In this project, four mesoporous silica SBA-15 catalyst supports with pore diameters in the range of 5-20 nm were synthesized in the preliminary phase using hexane as the micelle swelling agent and subsequently utilized for the loading of 2 wt.% Fe and 15 wt.% W catalyst metals, respectively. The hexagonal mesoscopic

structure of these materials were characterized using powder small-angle X-ray scattering (SAXS), N_2 adsorption-desorption isotherms, TEM and SEM images. Powder XRD analysis evidenced inhomogeneous metal dispersion on the largest pore diameter catalyst. An optimum pore diameter of 10 nm was found for Cat-B and subsequently used to obtain the optimum Fe and W loadings required to achieve the best hydrodesulfurization (HDS) and hydrodenitrogenation (HDN) activities.

The optimum catalyst was found to be Cat-H with metal loadings of 3 wt.% Fe and 30 wt.% W. At these loadings and temperatures of 375°C, 388°C, and 400°C, HDS activities of 53.4%, 64.1%, and 73.3% with corresponding HDN activities of 21.9%, 26.2%, and 38.3%, respectively, were recorded. Catalytic performance evaluations conducted on equal mass loading using a reference commercial γ-Al_2O_3-supported FeW catalyst offered HDS activities of 69.3%, 80.4%, and 89.1%, with corresponding HDN activities of 16.4%, 32.4%, and 49.3% at the same temperatures studied. However, no significant changes in HDS and HDN activities were observed for similar evaluations on volume percent metals loading basis.

Kinetic studies performed with the optimum FeW/SBA-15 catalyst suggested activation energies of 147.2 and 150.6 kJ/mol for HDS and HDN, respectively, by the Langmuir-Hinshelwood's model. Similar results were predicted by the Power Law and Multi-parameter models for HDS (129.6 and 126.7 kJ/mol, respectively), which does not conclusively make the latter model clearly stand out as the best. Data fitting by the Power Law suggested reaction orders of 2 and 1.5 for HDS and HDN, which seem to be consistent for the hydrotreatment of heavy gas oil. Finally, a long-term

deactivation study spanning a period of 60 days time-on-stream showed the optimum catalyst to be stable under hydrotreating experiments conducted in a downward flow micro-trickle bed reactor at temperature, pressure, liquid hourly space velocity (LHSV), and gas/oil ratio of 375–400˚C, 8.8 MPa, $1h^{-1}$, and 600 mL/mL (at STP), respectively.

ACKNOWLEDGEMENT

I would first like to extend the warmest appreciation to my two supervisors, Dr. Ajay Dalai and Dr. John Adjaye, for their mentorship, valued guidance and critical supervision throughout the planning, execution, and communication of my thesis work. I am extremely thankful to the time devoted by both supervisors to critically review and constructively criticize my written materials. Special thanks also go to the other two members of my evaluation committee: Drs. Jafar Soltan and Hui Wang, for their valuable contribution and guidance to my graduate studies. I also want to be grateful to Dr. Lee Wilson for accepting to be my external examiner.

Secondly, I would also like to thank Drs. Kapil Soni and Chandra Mouli for their post-doctoral guidance, contribution and encouragement. Thanks also go to Mr. Richard Blondin, Mr. Dragan Cekic and Miss Heli Eunike for their assistance in the laboratory work that contributed to my project. A special thanks go to Dr. Christian Botchwey, Majak Mapiour and Stefan Sigurdson for their counsel, friendship, constant support, and countless hours for proof-reading my works. Also, thanks are due to all members of the Catalysis and Chemical Reaction Laboratories for their support throughout my study. My gratitude also goes to the Natural Science and Engineering Research Council of Canada (NSERC) and Syncrude Canada Limited for their much-needed financial assistance.

Lastly, I would like to thank all the professors, post-doctorate fellows and graduate students who have contributed to my studies at the University of Saskatchewan. Most of all, I would like to thank my mother (Beatrice Kwofie), father

(Tonny Effah Gyamfi), and all my siblings for always supporting and believing in me. To all I say, thanks so much for your love.

TABLE OF CONTENTS

LIST OF TABLES

LIST OF FIGURES

NOMENCLATURE

α	proportionality constant relating system pressure to H_2 partial pressure, dimensionless
β_{HDN}	isothermality ratio for the catalyst pellet in a hydrodenitrogenation reaction, dimensionless
β_{HDS}	isothermality ratio for the catalyst pellet in a hydrodenitrogenation reaction, dimensionless
γ_P	tortuosity of the catalyst pellets, dimensionless
$\Delta\rho_T$	temperature density correlation, lbs/ft^3
$\Delta\rho_P$	pressure density correlation, lbs/ft^3
$\Delta H_{R,HDN}$	heat of the hydrodenitrogenation reaction, kJ/mol
$\Delta H_{R,HDS}$	heat of the hydrodesulfurization reaction, kJ/mol
ε	catalyst bed porosity, dimensionless
ε_P	porosity of the catalyst pellets, dimensionless
$[\eta_O]_N$	effectiveness factor at the inlet of the hydrodenitrogenation reaction, dimensionless
$[\eta_O]_S$	effectiveness factor at the inlet of the hydrodesulfurization reaction, dimensionless
$[\eta_P]_N$	effectiveness factor at the outlet of the hydrodenitrogenation reaction, dimensionless
$[\eta_P]_S$	effectiveness factor at the outlet of the hydrodesulfurization reaction, dimensionless
$[\Phi_O]_N$	dimensionless Thiele modulus at the inlet of the hydrodenitrogenation reaction, dimensionless
$[\Phi_O]_S$	dimensionless Thiele modulus at the inlet of the hydrodesulfurization reaction, dimensionless

$[\Phi_P]_N$	dimensionless Thiele modulus at the outlet of the hydrodenitrogenation reaction, dimensionless
$[\Phi_P]_S$	dimensionless Thiele modulus at the inlet of the hydrodesulfurization reaction, dimensionless
λ_{H2}	hydrogen solubility in HGO, mL/(kg·MPa)
λ_N	adsorption energy for all nitrogen heteroatoms within heavy gas oil, J/mol
λ_S	adsorption energy for all sulfur heteroatoms within heavy gas oil, J/mol
μ_L	viscosity of HGO at the operating temperature, g/(s·cm)
$\rho_{15.6}$	density of HGO at 15.6°C, g/mL
ρ_{20}	density of HGO at 20°C, g/mL
ρ_L	density of HGO at the operating conditions, g/mL
a_L	interfacial surface area over unit volume of a catalyst, cm^{-1}
a_S	liquid/solid interfacial surface area, cm^{-1}
$°API$	American Petroleum Institute gravity of petroleum liquids, dimensionless
A	surface area of catalysts and catalyst supports found from BET analysis, m^2/g
A_{HDN}	Arrhenius constant for the hydrodenitrogenation reaction rate, $s^{-1}\cdot(mol/L)^{(1-v)}$
A_{HDS}	Arrhenius constant for the hydrodesulfurization reaction rate, $s^{-1}\cdot(mol/L)^{(1-n)}$
$[C_S]_S$	catalyst surface concentration of sulfur species, mol/mL
$[C_N]_S$	catalyst surface concentration of nitrogen species, mol/mL
C_{AA}	concentration of aromatic amines, mol/L

C_{H2}	hydrogen concentration in the liquid phase at equilibrium, mol/mL
C_i	concentration of species ***i*** heteroatom, mol/L
C_O	feed concentration of species ***X*** heteroatom, mol/L
C_P	product concentration of species ***X*** heteroatom, mol/L
C_N	concentration of all nitrogen heteroatoms within heavy gas oil, mol/L
C_S	concentration of all sulfur heteroatoms within heavy gas oil, mol/L
C_{SA}	concentration of saturated quinoline, mol/L
C_X	concentration of species ***X***, mol/L
C_Y	concentration of ammonia, mol/L
d	average pore diameter of catalysts and catalyst supports, nm
d_P	average diameter of the catalyst particles, cm
$[D_N]_E$	effective diffusivity of organonitrogen compounds, cm^2/g
$[D_S]_E$	effective diffusivity of organosulfur compounds, cm^2/g
D_L	diffusivity of hydrogen in HGO, cm^2/s
D_N	bulk diffusivity of organonitrogen compounds, cm^2/g
D_S	bulk diffusivity of organosulfur compounds, cm^2/g
E_{HDN}	activation energy for the hydrodenitrogenaton reaction, J/mol
E_{HDS}	activation energy for the hydrodesulfurization reaction, J/mol
G/L	ratio of volumetric flow rates between hydrogen gas and coker light gas oil, dimensionless (mL/mL)
H_{H2}	Henry's constant for hydrogen in HGO, $MPa \cdot m^3/mol$
k_{AX}	apparent rate constant for the consumption of species ***X***, $s^{-1} \cdot C_X^{(1-n)}$
k_B	rate constant of butene, $mol/(L \cdot s)$
k_{HDN}	rate constant of hydrodenitrogenation, $s^{-1} \cdot (mol/L)^{(1-v)}$

k_{HDS}	rate constant of hydrodesulfurization, $s^{-1}\cdot(mol/L)^{(1-n)}$
k_L	H_2/HGO mass transfer coefficient – gas/liquid side, cm/s
k_{OVR}	overall mass transfer coefficient for hydrogen, cm/s
k_S	H_2/HGO mass transfer coefficient – liquid/solid side, cm/s
k_t	thermal conductivity of the FeW/SBA-15 catalyst pellet, J/(cm·K)
k_T	rate constant of thiophene, mol/(L·s)
k_X	rate constant for the consumption of species X, $s^{-1}\cdot C_X^{(1-n)}\cdot P_{H2}^{(1-m)}$
K_A	adsorption equilibrium constant for butane, Pa^{-1}
K_{AA}	adsorption equilibrium constant for aromatic amines, Pa^{-1}
K_B	adsorption equilibrium constant for butene, Pa^{-1}
K_{H2}	adsorption equilibrium constant for hydrogen gas, Pa^{-1}
K_{H2S}	adsorption equilibrium constant for hydrogen sulfide, Pa^{-1}
K_i	adsorption equilibrium constant for species i heteroatom, L/mol
K_N	adsorption equilibrium constant for nitrogen heteroatoms within heavy gas oil, L/mol
K_S	adsorption equilibrium constant for sulfur heteroatoms within heavy gas oil, L/mol
K_{SA}	adsorption equilibrium constant for saturated quinoline, Pa^{-1}
K_T	adsorption equilibrium constant for thiophene, Pa^{-1}
K_Y	adsorption equilibrium constant for ammonia, Pa^{-1}
L_A	liquid mass flow over cross-sectional area, $g/(s\cdot cm^2)$
$LHSV$	liquid hourly space velocity, h^{-1}
m	reaction order constant for the denominator of the HDS rate model, dimensionless
M_{AVE}	average molecular weight of HGO, g/mol

n	reaction order constant for the numerator of the HDS rate model, dimensionless
N_λ	proportionality constant for the nitrogen adsorption equilibrium constant expression, L/mol
N_E	proportionality constant for the HDN reaction rate constant expression, $s^{-1}\cdot(mol/L)^{(1-v)}\cdot(Pa)^{(-p)}$
$N_{E\alpha}$	proportionality constant for the HDN reaction rate constant expression after system pressure substitution, $s^{-1}\cdot(mol/L)^{(1-v)}\cdot(Pa)^{(-p)}$
p	reaction order constant for H_2 partial pressure term, dimensionless
P	system pressure, Pa
P_A	partial pressure of butane, Pa
P_B	partial pressure of butene, Pa
P_{H2}	partial pressure of hydrogen gas, Pa
P_{H2S}	partial pressure of hydrogen sulfide, Pa
P_T	partial pressure of thiophene, Pa
r_B	reaction rate of butene, mol/(L·s)
r_{HDN}	rate of the overall hydrodenitrogenation reaction, mol/(L·s)
r_{HDS}	rate of the overall hydrodesulfurization reaction, mol/(L·s)
r_{ij}	rate of change of species i heteroatom for reaction j, mol/(L·s)
r_T	reaction rate of thiophene, mol/(L·s)
r_X	reaction rate of species X, mol/(L·s)
R	universal gas constant, 8.314 J/(mol·K)
$(R^2)_{HDN}$	coefficient of regression for the hydrodenitrogenation reaction models, dimensionless
$(R^2)_{HDS}$	coefficient of regression for the hydrodesulfurization reaction models, dimensionless

$(R^2_A)_{HDN}$	adjusted coefficient of regression for the hydrodenitrogenation reaction models, dimensionless
$(R^2_A)_{HDS}$	adjusted coefficient of regression for the hydrodesulfurization reaction models, dimensionless
S_λ	proportionality constant for the sulfur adsorption equilibrium constant expression, L/mol
S_E	proportionality constant for the HDS reaction rate constant expression, $s^{-1}\cdot(mol/L)^{(1-n)}\cdot(Pa)^{(-p)}$
$S_{E\alpha}$	proportionality constant for the HDS reaction rate constant expression after system pressure substitution, $s^{-1}\cdot(mol/L)^{(1-n)}\cdot(Pa)^{(-p)}$
SG	specific gravity of HGO at 15.6°C, dimensionless
T	reaction temperature, K
T_b	average boiling point of HGO, K
T_S	pellet surface temperature, K
u	reaction order constant for the denominator of the HDN rate model, dimensionless
v	reaction order constant for the numerator of the HDN rate model, dimensionless
v_C	critical specific molar volume of HGO, mL/mol
v_C^m	critical specific mass volume, mL/g
v_i	molar volume of sulfur/nitrogen molecules under standard conditions, mL/mol
v_L	molar volume of HGO under standard conditions, mL/mol
v_N	hydrogen molar volume at standard conditions, L/mol
V	total pore volume found for catalysts and catalyst supports, cc/g
V_b	hydrogen molar volume at the normal boiling point, mL/mol
V_C	volume of loaded catalyst, mL

x_{HDN}	stoichiometric ratio of hydrogen consumption over nitrogen removal, dimensionless
x_{HDS}	stoichiometric ratio of hydrogen consumption over sulfur removal, dimensionless
X	association parameter, dimensionless

1.0 INTRODUCTION

The quest for sustainable growth and eco-friendly gaseous emissions from internal combustion engines give good reasons to constrain the activities of refining industries worldwide so as to produce cleaner fuels. Considering the degraded feedstocks being handled, mostly products from residua upgrading, then suffice it to say that the removal of heteroatoms from these feedstocks will present a considerable challenge to refiners. That notwithstanding, the refining industry is also faced with the challenge to find more flexibility in operations so as to meet the growing demand of diesel and gasoline. The story ends with the hard fact that hazardous gaseous emissions be reduced to the barest minimum as possible. This means basically rejecting carbon from every barrel of crude processed, preferably not as CO_2, transferring hydrogen from naphtha and heavy ends towards middle distillates, and removing heteroatoms (Toulhoat et al., 2001).

The world wide conventional crude oil production is anticipated to reach its peak in 2014 due to the rapid growth in global oil consumption (www.sciencedaily.com, 2010). As a result of this forecasted downward surge in the global oil demand outlook, processing of alternative sources such as unconventional oil reserves will be of dire necessity if rising future demands are to be met. Alberta's oil sands located in the Western province ranks second only to Saudi Arabia in global-proven energy reserves (Podlubny, 2008). Most of these reserves are found in the oil sands. Oil sands are naturally occurring mixtures of sand or clay, water and an extremely dense and viscous form of petroleum known as bitumen.

The Athabasca oil sands consists of a large deposits of bitumen (extremely heavy crude oil) located in northeastern Alberta, Canada. The constituents of Athabasca bitumen are complex hydrocarbons extracted from the oil sands, leaving mostly clay and water components as residues. Further processing of the extracted bitumen yields fractions such as naphtha, light gas oil (LGO), and heavy gas oil (HGO) liquid products. However, the unconventional crude oil fractions derived from oil sands are of much lower quality compared to conventional crude oil. They have relatively high contents of organo-sulfur and nitrogen compounds; making end products difficult to meet standard emission specifications. They are also highly aromatic in nature resulting in low quality products where especially diesel fuel is desired. Moreover, downstream processing of these feedstocks is a major challenge due to the high nitrogen contents, which tends to deactivate noble metals in the fluid catalytic cracking (FCC) unit. In order to find application as transportation fuel to meet stringent environmental specifications, they need to be subjected to intensive upgrading by way of hydrotreating (Speight, 2000).

The noxious gaseous emissions produced from the combustion of fuels derived from such high sulfur content feedstocks in internal combustion engines is identified as a significant problem that may limit the application of bitumen-derived gas oils as fuel. As a result, the world-wide concerns raised by environmental regulatory bodies to curb this issue have received significant attention. For instance, the maximum permissible sulfur content in gasoline was mandated to be lowered from 150 to 30 ppm as of June 1, 2005 all across Canada (Canadian EPA, 1999). Moreover,

a similar constraint was imposed on diesel fuels imported to or produced in Canada to be used in on-road vehicles to meet the ultra-low sulfur diesel (ULSD) specifications by September 1, 2007. The cut down of about 97% on the maximum allowable sulfur content in diesel fuel from 500 ppm to 15 ppm is of great concern to refiners and thus, demands drastic measures. It is anticipated that effective June 1, 2012, all types of off-road diesel engines must meet this standard specifications (www.ec.gc.ca, 2009); thus suggesting a more efficient hydrotreating operations.

During a typical hydrotreatment operation, the petroleum fraction is subjected to a catalytic hydrogenation process at high temperatures (370–400°C) and moderate pressures (6.9 – 9.7 MPa) so as to remove the organo-sulfur and nitrogen compounds in the form of H_2S and NH_3, respectively. The removal of sulfur and nitrogen under such reaction conditions are termed hydrodesulfurization (HDS) and hydrodenitrogenation (HDN), respectively. Although, this upgrading process is principally advisable mostly for the protection of downstream noble catalysts, it should not be carried out at the detriment of the environment since the evolution of NO_x and SO_x after combustions in IC engines are considered noxious pollutants and have severe health hazards. It is well-known that the high concentrations of organo-nitrogen compounds are responsible for the deactivation of reforming and hydrocracking catalysts. Nevertheless, during the hydrotreating process, it is also known that these N-containing compounds are the most common precursors of catalyst poisoning due to their reactivity on catalyst active sites. The basic nature of these compounds causes them to strongly adsorb onto Lewis acid sites on the catalyst

surface; thus inhibiting the availability of the sites. Depending on the hydroprocessing conditions, catalyst active site poisoning may be reversible or irreversible (Furimsky et al, 1999).

Over the years, heterogeneous catalysis has found industrial applications in the field of oil hydroprocessing. In a typical hydrotreating catalyst, metal components having activities for HDS and HDN are generally dispersed by way of impregnation on inorganic oxide supports with high porosity. The bimetallic catalytic system commonly used constitutes an active metal sulfide phase (MoS_2 or WS_2), promoted by Ni or Co. In most cases, the support provides the needed surface area for the dispersion of the metal species and also improves the mechanical strength of the catalyst pellets.

Petroleum feedstocks handled from Athabasca bitumen contains appreciably high amounts of sulfur and nitrogen compounds in the range of 4-4.5 wt.% and 0.2 – 0.35 wt.%, respectively. Due to the low quality of these fractions, significant importance must be allotted to the catalysts used in the hydrotreating of such feedstocks. Efficient approaches towards performance improvement of the catalysts used in such processes include: changing the active phase (carbide, nitride, phosphide, etc.), using a different catalyst preparation method (co-precipitation, chemical vapor deposition, etc.) or applying new types of catalyst supports (CNTs, mesoporous silicas such as Santa Barbara Amorphous (SBA-15)). These ordered mesoporous materials are considered ideal hosts for nanoparticles due to their large surface area and well-defined pore structure. Most importantly, their pore sizes can be tuned within the

nanometer range and the pore surface can be functionalized with various metal oxides and organic groups. Among these materials, SBA-15 silica has been extensively studied due to their 2-D structure with interconnected pores (Ryoo et al., 2000). SBA-15 is a mesoporous silica molecular sieve with high surface area, tuneable uniform hexagonal channels ranging from 5 to 30 nm and thick framework walls (3-6 nm), which is characteristic for it being thermally and hydro-thermally robust (Zhao et al., 1998; Cao et al., 2003). Such attractive textural properties of SBA-15 makes it a potential alternative to the commonly used γ-Al_2O_3 support due to the fact that its pore size can be manipulated via controlling the synthesis parameters, while maintaining relatively high surface area.

In this thesis, the hydrotreatment of heavy gas oil using SBA-15-supported FeW catalysts was investigated. Iron-tungsten catalysts prepared from these siliceous SBA-15 supports were characterized and screened for their catalytic performance. For purpose of comparison, an equivalent mass and volume loadings of a reference Fe-W catalyst supported on commercial γ–Al_2O_3 were also prepared and screened. Catalytic performance of these catalysts was based on the HDS and HDN activities displayed during the hydrotreating of HGO derived from Athabasca bitumen.

1.1 Knowledge Gaps

It is shown herein that the limited number of studies applying Fe-W/SBA-15 catalyst for hydrotreating reactions present opportunities for exploring the characteristic performance of such catalysts. The synthesis approach followed to vary the pore diameter of SBA-15 supports is considered effective towards obtaining the

optimum pore diameter of the support. The application of larger pore diameter SBA-15 supports synthesized using low initial synthesis temperature in the presence of swelling agent (hexane) and subsequently employed for hydrotreating catalyst purposes would be of great interest. From the review of available literature (Chapter 2) regarding the application of different pore diameter SBA-15 supports and their effect on hydrotreating activities of HGO using Fe-W catalysts, relevant knowledge gaps were identified and discussed as follows:

- Though the pore diameter of a catalyst plays a vital role in the diffusion of reactant molecules to catalytic active sites; thereby affecting the rate of conversions of the hydrotreating reactions, limited studies have been devoted to this subject in the open literature.
- In fact limited studies have been conducted on the Fe-W catalyst system and its application for hydrotreating activities.
- No specific study was found whereby SBA-15 was used to support Fe-W catalyst system or wherein the effect of pore diameter of such catalyst on the HDT activities of HGO derived from Athabasca bitumen was investigated.
- Lastly, there are limited studies on the long-term deactivation rate of the Fe-W catalyst system.

1.2 Hypotheses

- Adjusting initial synthesis temperature and the addition of swelling agent to the synthesis medium can help control the pore diameters of SBA-15. The amount of

swelling agent added to the synthesis medium will also allow the pore diameter of the resulting SBA-15 materials to be controlled. The initial synthesis temperature is critical in the gelation step. Thus by maintaining a low initial synthesis temperature and varying the amount of swelling agent used, the textural properties (surface area, pore volume and pore diameter) of the SBA-15 support can be tuned to produce an optimum catalyst that will facilitate the diffusion of bulky HGO molecules to the active metal sites; thus enhancing the HDS and HDN activities over the Fe-W/SBA-15 catalyst.

- The larger pore diameter of SBA-15 support will help reduce the effect of catalyst deactivation by pore mouth blockage that is most prevalent in commercial γ-Al_2O_3 support during processing of heavier feedstocks. This will prolong the activity of the Fe-W/SBA-15 catalyst as a result of time-on-stream as compared to the Fe-W catalyst supported on the commercial γ-Al_2O_3.
- Catalytic activity has a relation with the amount of metals loaded on the support. The high surface area of the SBA-15 support will provide sufficiently vast area for metal loading; thereby enhancing metal dispersion on the support.
- Incorporation of Fe to the W/SBA-15 or W/γ-Al_2O_3 catalyst will promote the synergistic effect between Fe and W; enhancing the HDS and HDN activities of such catalysts.

1.3 Research Objectives

The main focus of this research work was to investigate the effect of varying the pore diameter of sulfided Fe-W/SBA-15 catalysts and correlating the pore

diameter variation with hydrotreating performance based on screening activities of the different pore diameter Fe-W/SBA-15 catalysts using HGO derived from Athabasca bitumen. The optimum catalyst produced will be selected based on the optimum pore diameter of SBA-15 support produced and the optimum amounts of metal loading (Fe and W, wt.%) yielding the optimum HDS and HDN activities. To monitor progress of the overall objectives, activities have been categorized into the following five phases:

- **Phase I: SBA-15 supports syntheses, optimization and characterization**

This phase of the project was designed to synthesize SBA-15 supports of large pore diameter in the range 5 – 20 nm by using the sol-gel method. The initial synthesis temperature was chosen and maintained at 15°C and the amount of micelle expanders (hexane) used was varied to examine how the pore diameter changes. These supports were characterized by the small-angle X-ray scattering, N_2 adsorption/desorption analysis, scanning electron microscopy and transmission electron microscopic techniques.

- **Phase II: Pore diameter variation of SBA-15 supports and catalytic performance test**

Specifically, four SBA-15 catalysts of pore diameters 5.7, 10.1, 15.7 and 18.5 nm were synthesized, characterized and screened for their HDS and HDN activities using HGO. Equivalent amounts of Fe & W (2 wt.% and 15 wt.%) respectively were loaded on these supports and subsequently screened for their catalytic performance. Their effectiveness was based on the total sulfur and nitrogen conversions.

- **<u>Phase III</u>: Catalyst performance optimization and characterization**

  After obtaining the optimum pore diameter SBA-15 catalyst support, the optimum metals (both Fe and W) loadings were also determined. The incipient wetness co-impregnation techniques was employed to load calculated wt.% of Fe and W on the SBA-15 support surface. After catalysts drying and calcination procedures, the inductively coupled plasma mass spectroscopic (ICP/MS) analysis was used to ascertain the actual amount of metals loaded in the catalyst. The changes to the characteristics and behavior of the catalysts due to metal loading changes were further classified by N_2 adsorption/desorption, CO chemisorption, and DRIFTS of CO adsorption.

- **<u>Phase IV</u>: Kinetics study for the optimum Fe-W/SBA-15 catalyst**

Hydrotreating activities using heavy gas oil was carried out on all the various catalysts prepared and the optimum composition for the Fe-W/SBA-15 catalyst was determined based on their performance for the HDS and HDN reactions. Process parameters study was also carried out to help investigate the kinetics of the hydrotreating reactions. With regards to this, the effects of reaction temperature, pressure, LHSV and gas-to-oil ratio was determined for the HDS and HDN of the heavy gas oil. For the kinetic study, the three basic models (power law, Langmuir-Hinshelwood, and Multi-parameter models) were adapted to correlate the HDS and HDN activities of the optimum Fe-W/SBA-15 catalysts. These models for the Fe-

W/SBA-15 catalysts were developed to make it possible for the prediction of HDS and HDN reaction kinetics under different operation conditions other than that used to develop them.

- **<u>Phase V</u>: Longevity study for optimum Fe-W/SBA-15 catalyst**

This phase of the project was designed to investigate the HDS and HDN activities of the optimum Fe-W/SBA-15 catalyst as a result of extended time-on-stream. A long-term activity study plan was carried out over a 60 day period so as to gain an idea about how the catalyst will perform under the prolonged industrial running conditions.

2.0 LITERATURE REVIEW – PETROLEUM HYDROTREATING

In this chapter, general concepts of the hydrotreating activities are reviewed. The first section discusses the background and concepts relating the hydrotreating of petroleum. This includes bitumen upgrading, definition of bitumen, gas oil, and heavy gas oils. Some chemical compounds present in heavy gas oils are also presented in this chapter. The two pertinent hydrotreating reactions (hydrodesulphurization and hydrodenitrogenation) and catalysts used therein are also discussed. Kinetic models commonly used to mimic the behavior of these reactions are also reviewed. Finally, factors contributing to hydrotreating catalyst deactivation are also discussed.

2.1 Bitumen upgrading

The second major step after oil sand is mined is bitumen extraction. Bitumen is a mixture of organic liquids (hydrocarbons) that are highly viscous, black, sticky and composed primarily of highly condensed chemical compound (www.saocl.com, 2010). Bitumen is the residual or by product obtained by fractional distillation of crude oil. It is the heaviest and thickest form of petroleum fraction with the highest boiling point. It is a complex mixture of constituents of variable molecular weights and compositions of which 80% of saturates present in bitumen are associated with distillates of heavy gas oil fractions (Zhao et al., 2000). Bitumen and heavy gas oil fractions are characterized in terms of their physical properties (see Table 2.1).

Table 2.1: **Definition of heavy oils and bitumen (Gray, 1994)**

Fraction	Viscosity (mPa.s)	Density (g/cm^3)	API gravity (°)
Heavy oil	10^2 - 10^5	0.935 - 1.0	10 - 20
Bitumen	$>10^5$	>1.0	<10

Heavy crude oil does not flow easily. Because of its high density or specific gravity, it is mostly referred to as "heavy"; a generic term applied to any liquid petroleum fraction with API gravity less than 20° (Dusseault, 2008). The American Petroleum Institute (API) gravity gives a measure of how heavy or light a petroleum fraction is compared to water. It is related to specific gravity in such a way that an increase in API gravity corresponds to a decrease in specific gravity. Thus a fraction with API gravity greater than 10 is lighter than water; hence, will float on water. Typically, the API gravity of heavy oil is mostly in the range of 10-15°. The API gravity of Athabasca bitumen is in the range 7.7-9.0°.

The fraction of petroleum feedstock that distills off in the temperature range of 315-425°C is normally termed as heavy gas oil (HGO). This fraction is commonly used as a catalytic cracking feedstock or as light lubricating oil after suitable treatment. It is mostly obtained by vacuum distillation of crude petroleum.

In order to improve the commercial value of bitumen, it must be upgraded to lighter hydrocarbons. Upgrading of bitumen is mostly targeted into changing the

complex bitumen to lighter synthetic crude oils. This involves changing some physical and chemical properties of the bitumen. The two major stages of the upgrading process are: primary and secondary upgrading. Hydrotreating of gas oils falls under secondary upgrading process.

2.2 Hydrotreating and hydrotreating reactions

Hydrotreating or catalytic hydrogenation treatment is desired to remove objectionable materials from petroleum fractions by selectively reacting these materials with hydrogen in a reactor at relatively high temperatures and moderate pressures (Gruia, 2006). Schematically, the hydrotreating reaction process can be represented as shown below:

$$Feed \xrightarrow{CATALYST\ ,H_2,T,P} H/C + H_2S + NH_3 + H_2O \qquad \textbf{(Eqn. 2.1)}$$

These objectionable materials include, but are not solely limited to, sulfur, nitrogen, olefins, and aromatics. Olefins (which form gum and do not burn cleanly) are converted to clean-burning paraffins by the chemical addition of hydrogen. The lighter materials such as naphtha are generally treated for subsequent processing in catalytic reforming units, and the heavier distillates, ranging from jet fuel to heavy vacuum gas oils, are treated to meet strict product quality specifications or for use as feedstocks elsewhere in the refinery. Because these streams have high concentrations of sulfur, nitrogen and unsaturates, hydrotreating plays a key role towards reducing the high concentrations of these hetero-compounds (mostly S and N) to meet product quality specifications stipulated by environmental regulatory bodies.

During the hydrotreating process, organo-sulfur compounds are removed as H_2S, which is further processed in the Claus plant to yield elemental sulfur. This process of using hydrogen to remove sulfur from the petroleum fraction is termed hydrodesulfurization (HDS). Similarly, organo-nitrogen compounds are removed as NH_3 in a process known as hydrodenitrogenation (HDN) and burned in the utilities plant. Other reactions that occur in the hydrotreating process are hydrodeoxygenation (HDO), i.e. the removal of oxygen in the form of H_2O, and hydrodemetallization (HDM), i.e. the removal of metals such as nickel, vanadium, arsenic, etc. In spite of variable compositions of feedstocks handled, which is mostly dependent on the location, age of oil field as well as the depth of the individual oil, the prime motivation of these hydrotreating processes is to improve the quality of petroleum streams through a catalytic reaction with hydrogen gas so as to meet the progressively stringent emission standards. The most common reason for any hydrotreating application is for the purpose of preventing the emission of oxide pollutants (i.e. NO_X and SO_2) when the product is applied as a combustion engine fuel. Furthermore, pre-treating petroleum fractions for downstream processes such as catalytic cracking and reforming is essential to prevent excessive catalysts poisoning by heteroatom contaminants (Leffler, 2000). In as much as all the aforementioned hydroprocessing reactions are important, for any gas oil derived from Athabasca bitumen, hydrotreating is essentially important for the removal of contaminant sulfur and nitrogen organic compounds. The concern of sulfur emissions and downstream catalyst poisoning from nitrogen compounds make hydrodesulfurization and

hydrodenitrogenation the two principle processes for hydrotreating bitumen-derived gas oils due to their high concentrations of sulfur and nitrogen compounds.

2.2.1 Hydrodesulfurization (HDS)

As aforementioned, the HDS reaction principally eliminates sulfur from the organic petroleum feedstock through interaction with hydrogen on a solid catalyst surface. Organo-sulfur compounds found throughout petroleum fractions differ in the range of many hundreds of organic sulfur compounds. These sulfur compounds present in petroleum fractions can be classified into one of the following six sulfur types: mercaptans, sulfides, di-sulfides, thiophenes, benzo-thiophenes, and di-benzo-thiophenes. Typically, a schematic representation of the overall HDS reaction can be exemplified by the following:

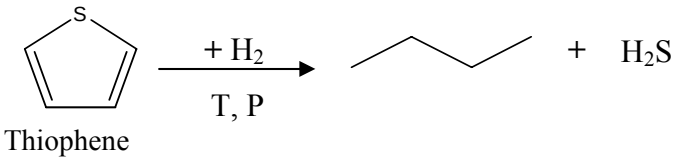

Thiophene **(2.2)**

The reaction in eqn. 2.2 shows the removal of a sulfur heteroatom from the thiophenic molecule in the form of H_2S gas. Figure 2.1 shows examples of typical reactions for the various organosulfur molecules that are commonly found in petroleum fractions.

Mercaptans

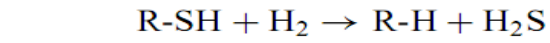

Sulfides

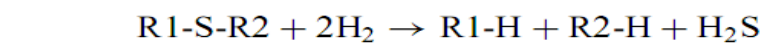

Di-sulfides

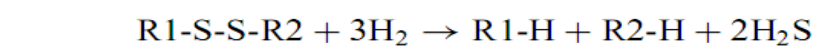

Thiophenes

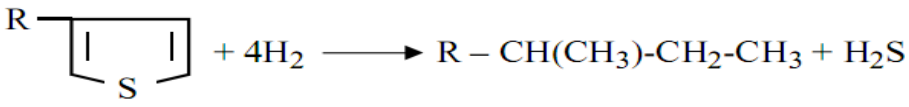

Benzo-thiophenes

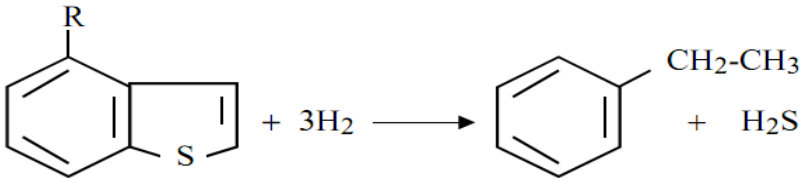

Di-benzo-thiophenes

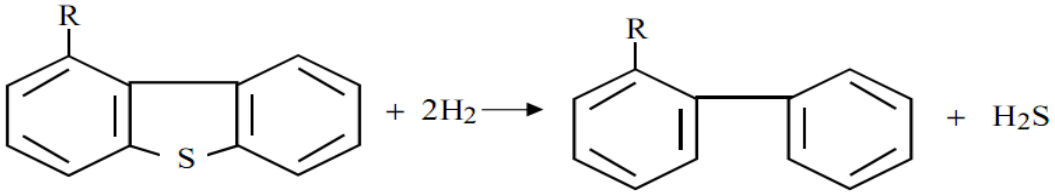

Figure 2.1: Reactions of typical organosulfur constituents of petroleum crude (Gruia, 2006).

The removal of sulfur from linear alkyl compounds such as mercaptans, sulfides, disulfides can proceed with ease. However, difficulty arises when the organo-sulfur species is embedded in a thiophenic ring. Gruia et al. 2006, demonstrated that depending on the types of sulfur present, the relative ease of

removing sulfur from a particular hydrocarbon fraction varies in the order as shown below:

Increasing difficulty of sulfur removal ⟶

Mercaptans → Sulfides → Disulfides → Thiophenes → Benzo-thiophenes →Dibenzothiophenes

Gas oil fractions are particularly difficult to hydrotreat as compared to naphtha fractions since most of the sulfur is present as benzo-thiophenes and di-benzo-thiophenes. Moreso, the more refractory sulfur species are found in the heavier fractions; making the hydrotreatment of heavy gas oils a more challenging task than light gas oils. In comparing the relative degree of difficulties of desulfurizing organo-sulfur compounds, Gruia et al. 2006 concluded that if the difficulty of converting diethyl-sulfide were on a level of 1, thiophene would be approximately a 5, benzo-thiophene would be a 15, and dibenzothiophene would be a 20 (Gruia, 2006). Under typical industrial hydrotreating processing conditions (e.g. 340-425°C and 5.6-17 MPa), HDS reactions are exothermic and irreversible (Speight, 1981). Thus increasing temperature decreases the equilibrium constant accordingly in consonance with the exothermic nature of the reaction.

As shown above, the reactivities of organosulfur compounds decrease with an increase in the number of aromatic rings; indicating dibenzothiophene to be the least reactive in the HDS conversion. The increase in the difficulty of conversion for these organo-sulfur compounds has been attributed to the delocalization of the lone-pair

electrons belonging to the sulfur atoms. This lowers the exposure of the sulfur groups and decreases their adsorptivity onto catalyst active sites (Girgis and Gates, 1991). Moreso, the reactivity further decreases with the occurrence of methyl substituent groups in the 4^{th} and 6^{th} positions (a typical case of 4, 6-dimethyl-dibenzothiophene). More specifically, the low reactivity of 4, 6-DMDBT is attributable to the steric hindrance effect. This makes it particularly difficult for the sulfur molecule to adsorb onto active sites of catalysts. This steric hindrance imposes an extent of difficulty for ring opening to occur prior to the heteroatom removal.

2.2.2 The HDS reaction mechanism

The change in the reactivity trends of HDS reactions is by reason of the fact that HDS reactions proceed via two possible pathways (see Figure 2.2). The structure of organo-sulfur compound to be removed determines the preferred pathway (Breysse, 2003). There are two main pathways by which HDS of thiophenic compounds occur:

1. Direct hydrogenolysis or direct sulfur extraction
2. Ring hydrogenation prior to hydrogenolysis

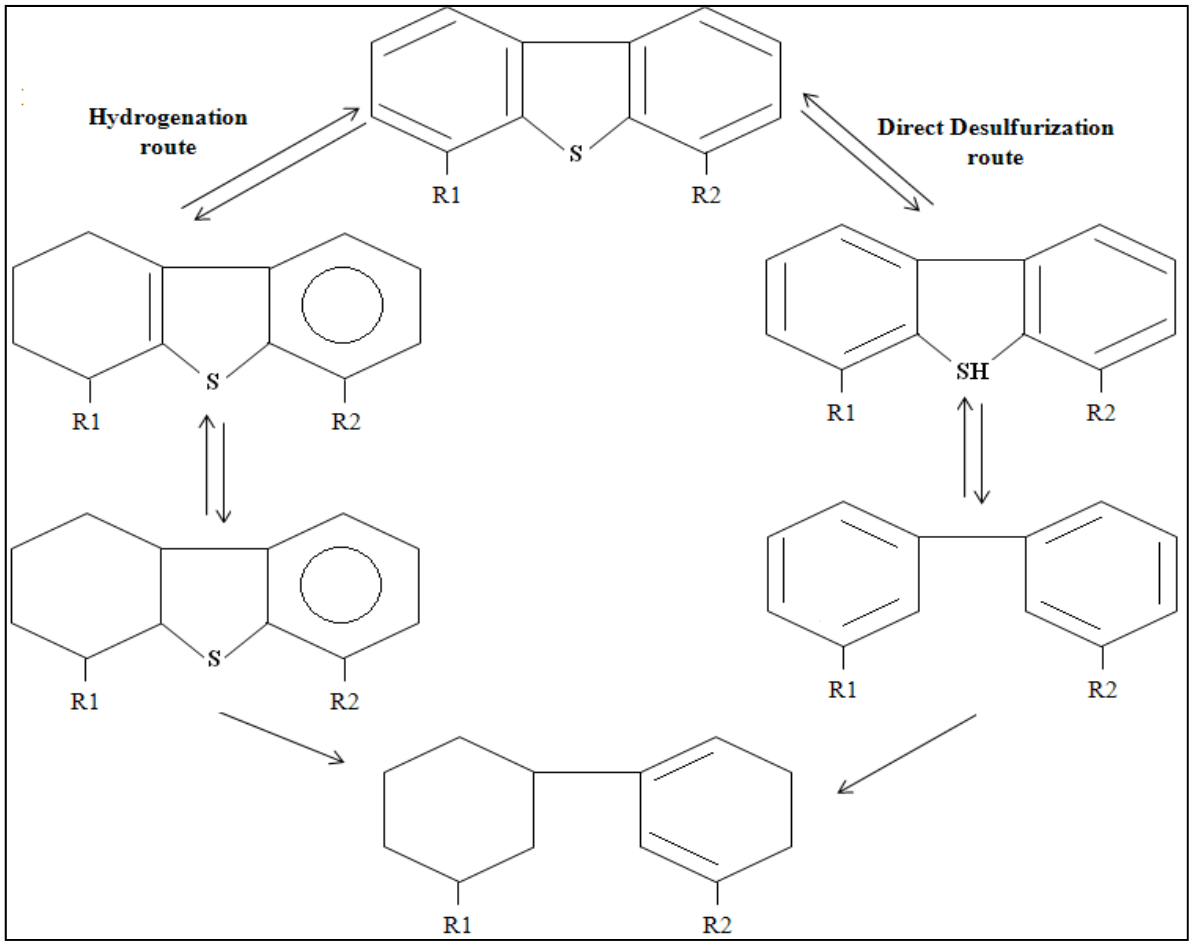

Figure 2.2: Proposed mechanism of HDS of 4, 6 DMDBT (Breysse et al., 2003)

As shown in Figure 2.2, the proposed HDS mechanism by Breysse et al., 2003, for the conversion of 4,6-DMDBT involves two main routes. The first pathway involves direct sulfur atom abstraction from the thiophenic ring without prior hydrogenation of the C=C ring containing the sulfur atom. However, in the second reaction pathway, the ring containing the sulfur atom is hydrogenated (saturated) prior to the sulfur-carbon bond scission (Breysse et al., 2003). The probability of one reaction pathway

being more favorable than the other is heavily dependent on reaction conditions, the feedstock compositions, and also the characteristics of the catalyst used in the reaction. For instance, whereas higher hydrogen pressure has been reported to favor the second pathway for a $NiMo/Al_2O_3$ catalyst (Girgis and Gates, 1991), a general preferable route for the HDS reaction proceeds via direct sulfur extraction; resulting in less hydrogen consumption and higher octane ratings. However, it should be noted that the second route could be limited by equilibrium conditions, especially at high temperatures since equilibrium constants vary inversely with temperature.

2.2.3 Hydrodenitrogenation (HDN)

Section 2.2 above describes the HDN reaction as the conventional method for effective removal of organonitrogen compound in the form of NH_3 via the interaction of the petroleum fraction with hydrogen gas on the surface of a solid catalyst. Organonitrogen compounds in the petroleum crude are mainly present as heterocyclic aromatic compounds. Other compounds present in smaller amounts include aliphatic amines and nitriles. As a result of their reactivity, the HDN of aliphatic amines and nitriles is very fast and these are hydrodenitrogenated more rapidly. The HDN of heterocyclic nitrogen compounds generally requires hydrogenation of nitrogen containing aromatic ring before removal of nitrogen molecule. The reactivity of such compounds varies in the following order (Clausen et al., 1996):

Quinoline > Pyridine > Isoquinoline > Indole > Pyrrole.

Generally, the two forms of heterocyclic nitrogen compounds mostly found in petroleum fractions include: the non-basic derivatives of pyrrole and indole and the basic derivatives of pyridine as shown in Figure 2.3 (Girgis and Gates, 1991).

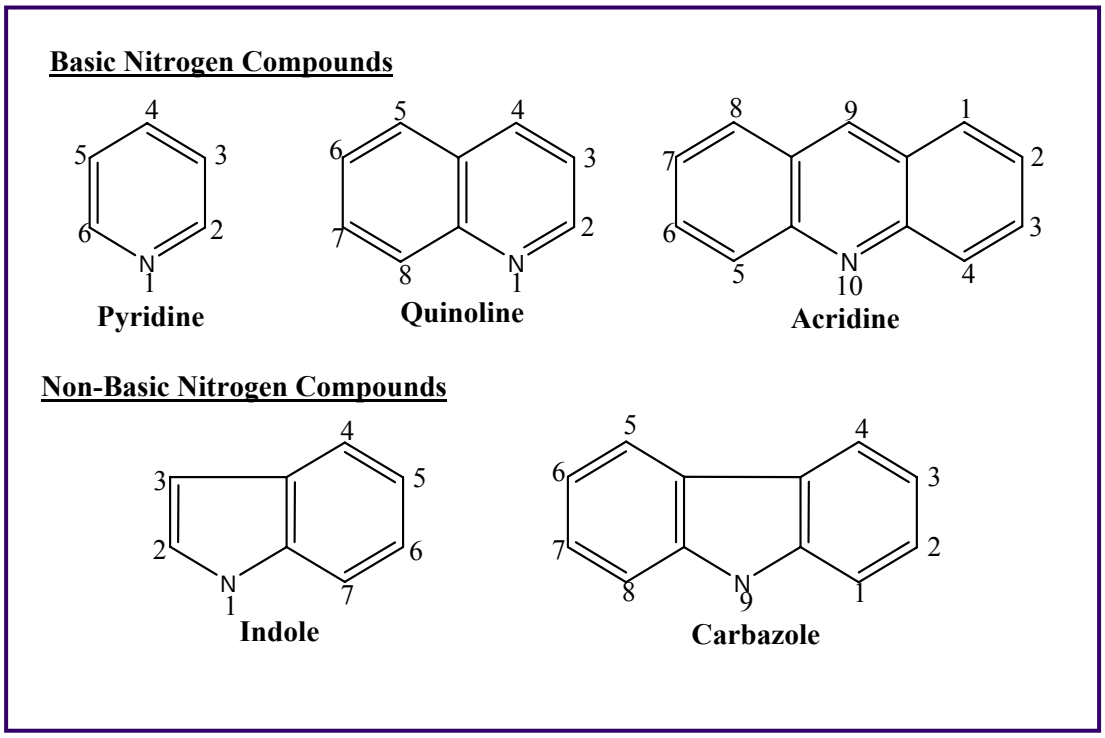

Figure 2.3: Examples of nitrogen compounds in petroleum distillates (Girgis and Gates, 1991)

Basic nitrogen compounds are the compounds with the nitrogen contained in a six-ringed structure. In these basic nitrogen compounds, the lone pair of electrons on the nitrogen atom is not delocalized in the ring containing the atom and so makes it readily available for reaction with acidic catalyst as a Lewis base. In other words, the nitrogen-containing ring is electron deficient due to the electron withdrawing

tendency of the nitrogen atom. Compounds with the nitrogen atom contained in at least one five-ringed member are referred to as non-basic nitrogen compounds. The lone pair of electrons in the non-basic compounds is delocalized over the aromatic ring and is unavailable for donation to a Lewis acid.

In comparing basicity of organonitrogen compounds, it is accepted that basic compounds are more reactive compared to non-basic compounds due to their stronger adsorption properties on catalyst active sites (Girgis and Gates, 1991, Zeuthen et al., 2001). This is the result of the lone pair electrons of the non-basic nitrogen heteroatom being delocalized within the aromatic ring and being inaccessible for donation as a Lewis base (Ho, 1988). The HDN conversion rates of organonitrogen compounds generally decrease as the molecular size of the aromatic compound increases, similar to the trend shown by organosulfur compounds for HDS. The reactivity of the basic nitrogen compounds would decrease in the order pyridine, quinoline, and acridine, while the reactivity of non-basic nitrogen compounds would decrease in the order of pyrrole, indole and carbazole (Topsoe et al., 1996).

2.2.4 The HDN reaction mechanism

A generic representation of the overall HDN reaction can be described by equation 2.3 below:

$$R-N+2H_2 \xrightarrow{CATALYST,T,P} R-H+NH_3 \qquad \textbf{2.3}$$

The resultant reaction is the replacement of the nitrogen heteroatom by hydrogen and the formation of ammonia gas. The generally accepted pathway for this

reaction to occur follows (i) hydrogenation of the aromatic ring structure, followed by (ii) hydrogenolysis of the energetically strong C-N bond. Equation 2.4 gives a simplified HDN reaction mechanism for pyridine under industrial conditions:

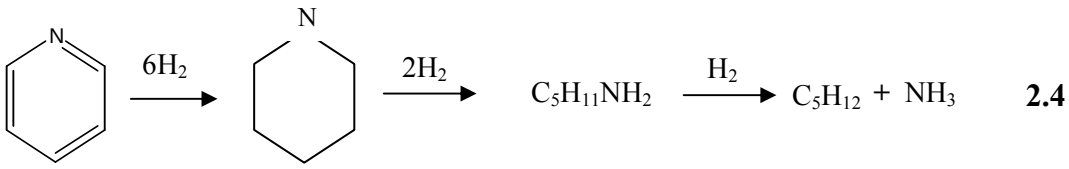

2.4

Due to the dual functionality of the catalyst, two different reaction sites are believed to be present on the hydrotreating catalyst (i.e. hydrogenation site and hydrogenolysis site). The catalysts require a balance between the relative activities of these two processes, and this balance will depend on compounds reacting. As mentioned earlier, unlike the HDS mechanism, the HDN reaction mechanism of heterocyclic compounds proceeds via one reaction pathway (see equation 2.4). The basic requirement for the HDN reaction is that the nitrogen-containing ring must first be hydrogenated (hydrogenation reaction) before nitrogen extraction can occur (hydrogenolysis reaction) (Girgis and Gates, 1991; Landau et al., 1997). Hydrogenation of the nitrogen-containing ring is necessary to reduce the relatively high bond energy of the C=N bond (615 kJ/mole) prior to C-N bond (389 kJ/mole) scission (Landau, 1997). This suggests that the HDN reaction is also limited by equilibrium effects. Hydrogenation of the nitrogen-associated aromatic ring structures is very dependent on the hydrogen partial pressure and is the rate limiting step of the

overall HDN reaction. Thus, high hydrogen partial pressures are usually used in the industry to force equilibrium towards the products side; hence, making the HDN reaction irreversible. Nevertheless, reaction pathways that minimize hydrogen consumption and maximize the fuel applicability of the petroleum feeds are not thermodynamically favored at typical industrial operating conditions (Cocchetto and Satterfield, 1981). Furthermore, the hydrogenation step in HDS mechanism is not considered to be critical (Girgis and Gates, 1991) since the bond energies of C=S and C-S bond are equal (536 kJ/mol). However, this step for the HDN reaction has been identified as very crucial (Girgis and Gates, 1991; Ho, 1988). This suggests that by using a specialized catalyst, the hydrogenation of the organonitrogen molecule could be selectively performed. Also, understanding the kinetic behavior of such catalysts would elucidate more on the reaction mechanisms of both the HDS and HDN reactions.

2.3 Development of kinetic models - Considerations

Internal and external mass transfer diffusions contribute significantly to the reaction rate of heterogeneous catalytic reactions. As shown in Figure 2.4, external diffusion is important when the reactants have to diffuse from the bulk of the fluid to the surface of the catalyst pellet. Subsequently, internal diffusion is important when the reactants move from the surface to the internal parts of the pellet.

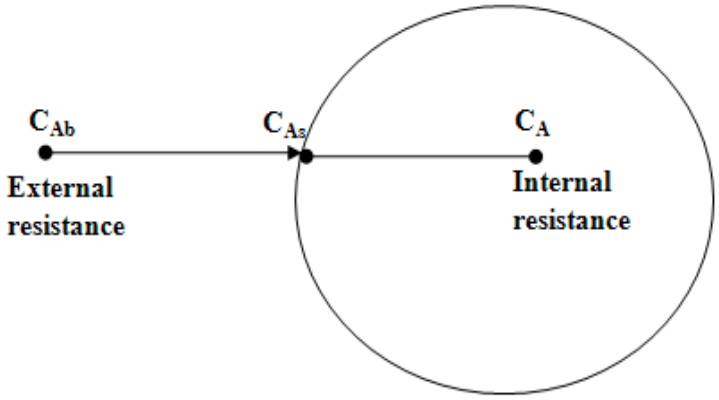

Figure 2.4: Mass transfer and reaction steps for a catalysts pellet.

These two resistances play a major role in the transfer rate of reactants to heterogeneous catalysts; and thus the study of intrinsic rates of reaction. Therefore the effects of internal and external mass diffusion have to be eliminated to get meaningful kinetic data. Otherwise, incorporation of the mass transfer parameters should take place in the reaction rate equation.

2.3.1 External mass transfer limitations

In many industrial reactors, rate of mass transfer of bulk reactants and products between the bulk fluid and the catalyst surface is small and limits the overall rate of the reaction. Generally laboratory reactors should be operated at high fluid velocities or with small catalysts particle size to eliminate the external mass transfer resistances. To study the effect of external mass transfer limitation, Mears proposed the criterion as follows;

$$C_m = \frac{-r'_A \rho_b Rn}{k_c C_{Ab}} < 0.15 \qquad \textbf{(2.5)}$$

Where, C_m is the ratio of reaction rate to the external diffusion rate. r_A, ρ_b, R, n, k_c, and C_{Ab} are the reaction rate per unit mass of catalyst (kmol/kg-s), bulk density of the catalyst bed (kg/m^3), catalyst particle radius (m), reaction order, mass transfer coefficient (m/s), and bulk concentration (kmol/m^3) respectively, and;

$$\rho_b = (1 - \varepsilon)\rho_c \qquad \textbf{(2.6)}$$

where; ε = catalyst bed porosity; ρ_c = catalyst density. If C_m value is less than 0.15, then external diffusion resistance is negligible.

2.3.2 Internal mass transfer limitations

Catalytic sites are also present in the inner pore channels of the catalysts. The concentration of a particular reactant at the outer surface of the catalysts is different than the concentration at the inner channels as shown in Figure 2.5.

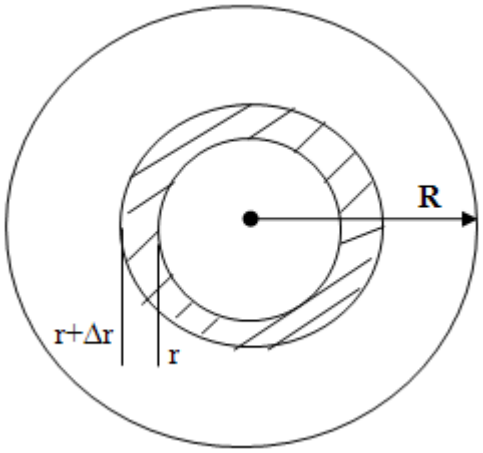

Figure 2.5: Internal mass transfer shell balance

If diffusion through the channels is slow with low diffusion mass transfer coefficients, then the overall rate of reaction will be controlled by internal mass transfer limitations. Effectiveness factor (η) is a parameter that describes the effect of internal diffusion resistance on the overall rate of the reaction. It can be defined as the ratio of the actual overall rate of reaction to the rate of reaction that would result if the entire interior surfaces were exposed to the external pellet surface conditions (C_{As}, T_s). It can be mathematically expressed as:

$$\eta = \frac{3}{\phi_1^2}\left(\phi_1 \coth \phi_1 - 1\right) \qquad \textbf{(2.6)}$$

where ϕ_n is the Thiele modulus for nth order reaction and is given by:

$$\phi_n^2 = \frac{k_n \rho_c S_a C_{As}^{n-1} R^2}{D_e} = \text{Surface reaction rate of "A" / Diffusion rate of "A"} \qquad \textbf{(2.7)}$$

and k_n = rate constant for nth order reaction, $(mol/m^3)^n$ (m/s); C_{As} = concentration of A at the catalyst surface (mol/m^3); ρ_c = catalyst density (kg/m^3); S_a = catalyst surface area (m^2/kg catalyst); R = radius of catalyst particle (m); D_e = effective diffusivity (m^2/s), defined as:

$$D_e = \frac{D_{AB}\phi_p\sigma}{\xi} \qquad \textbf{(2.8)}$$

where; D_{AB} = the bulk or Knudsen diffusivity of A in B; Φ_p = pellet porosity = (Volume of void space/total volume (voids and solids)); σ = constriction factor, and ξ = tortuosity (actual distance a molecule travels between two points/shortest distance between those two points).

If the Thiele modulus is large ($\varphi > 3$) and effectiveness factor, η, is less than 0.3, then internal diffusion limits the rate of the reaction. However, if the Thiele modulus is small ($\varphi < 1$) and effectiveness factor is greater than 0.7, then surface reaction is rate limiting.

Also used is the Weisz-Prater criterion, which uses the measured values of observed rate of reaction to determine whether the internal diffusion is significant or not. The Weisz-Prater parameter is given by:

$C_{WP} = \eta \phi_n^2$ = Actual reaction rate of "A" / Diffusion rate of "A"

$$C_{WP} = \frac{-r_{A\,obs}\,\rho_c\,R^2}{D_e\,C_{As}} \qquad \textbf{(2.9)}$$

If $C_{WP} << 1$, then internal diffusion resistance is negligible. Similarly, if $C_{WP} >> 1$, then internal diffusion limits the reaction.

2.3.3 Heat transfer considerations

The effects of heat generated by the hydrotreating reaction on the reactor performance must be considered at three levels namely intra-particle temperature gradients, inter-phase heat transport and temperature distribution in the reactor. The intra-particle temperature gradients depend on two parameters:

$$\beta = \frac{C_{As}\,(-\Delta H_r)\,D_{eff}}{\lambda_{eff}\,T_s} \qquad \text{(Prater number)} \qquad \textbf{(2.10)}$$

$$\gamma = \frac{E}{RT_s} \qquad \text{(Arrhenius number)} \qquad \textbf{(2.11)}$$

Also, the solid–fluid temperature differences are instead governed by the Biot number of the particle:

$$(B_i)_p = h_s d_p / \lambda_{eff} \qquad \textbf{(2.12)}$$

Where h_s is the heat transfer coefficient calculated from Chilton-Colburn analogy and d_p is particle diameter. The absence of intra-pellet heat transport limitation can be evaluated by comparing internal heat transfer resistance to that of external heat by means of Biot number (Ramirez et al., 2004). Thus, a Biot's number less than ten means that the internal resistance within the solid is negligible comparing to the external resistance across the fluid boundary, and thus uniform temperature distribution can be assumed across the solid (Anchyeta et al., 2002; Gierman, 1988; Baldi et al., 1986). It was demonstrated by Baldi et al., 1986 that the gradients inside a catalyst pellet with pores filled by liquid are very weak due to the low value of D_{eff} and the relatively high value of λ_{eff}. Moreover, if the particle is in contact with flowing liquid, $(Bi)_p$ is quite high because of the high value of the heat transfer coefficient. This means that if the particle is evenly and effectively wetted, there are no temperature gradients and the reaction at the particle level occurs isothermally (Giuseppe et al., 1999).

However, at low liquid velocities, thermal instability can take place in trickle-bed reactors because of the uneven liquid distribution at the particle scale (Germain, 1981). Stagnant liquid zones with very poor liquid renewal are very ineffective for heat transfer. The heat generated near these zones may give rise to a remarkable

increase of temperature that may eventually lead to evaporation of the liquid. In the dry zone then, a much faster gas phase reaction can take place that enhances evaporation and increases the local temperature. A hot spot so generated can extend to all parts of the reactor in particular operating conditions. This phenomenon has been observed at the bench scale by Germain et al., (1981) and Hanika et al., (1976).

Both the HDS and HDN reactions are irreversible and exothermic (de Brujn, 1976); thus formation of hot spots may result due to the heat generated in the reaction. High gas flow rates are used during the hydrotreating reaction to quickly dissipate this heat generated (Bej et al., 2001). Furthermore, diluting the catalyst with SiC greatly improves the heat transfer rate in the catalyst bed (Bej et al., 2001). Mostly in the open literature isothermality assumption is achieved when carrying out kinetic studies in micro-trickle bed reactors. However, a simulation work conducted by Botchwey et al. (2006) in a downward flow micro-trickle bed reactor concluded that the maximum temperature deviation between the reactor wall and the centre of the catalyst bed was about 4 °C. Due to this temperature uniformity in the axial direction and the fact that the diameter of the reactor was very small, isothermal condition was assumed. Nonetheless, the case may be different under reaction conditions. The distribution of temperature in the reactor is essentially caused by a convective mechanism. Gas and liquid are assumed to be at thermodynamic equilibrium (i.e. equal temperature, gas phase saturated by the liquid).

2.4 Modeling the kinetics of HDS and HDN reactions

Modeling the kinetic behavior of the hydrotreating process is vital towards gaining understanding of how reaction parameters such as temperature, pressure, LHVS, etc., affect the overall rate of species conversion in the hydrotreating reaction. Generally, the two main kinetic models commonly used to represent the overall rate of hydrodesulfurization and hydrodenitrogenation in the hydrotreating process are: the Power Law Model and the Langmuir-Hinshelwood Model. Due to its simplicity, the power law model is typically applicable to represent of the overall rate law for the various reactions taking place in the HDS and HDN processes. However, the Langmuir-Hinshelwood model is a bit more complicated since it takes into account the inhibition effects in the hydrotreating reaction processes.

2.4.1 Power Law Model

The power law model is the simplest model used by most researchers to fit kinetic data in order to obtain kinetic parameters. However, this model does not account for inhibition effects of other components present in the feedstock (Girgis and Gates, 1991; Smith, 1956; Botchwey et al., 2006). The overall reaction scheme for HDS and HDN are:

$$\text{Organosulfur compounds} + H_2 \longrightarrow \text{Saturated hydrocarbons} + NH_3 + H_2S \qquad \textbf{(2.13)}$$

$$\text{Organonitrogen compounds} + H_2 \longrightarrow \text{Saturated hydrocarbons} + NH_3 + H_2S \qquad \textbf{(2.14)}$$

Thus the power law model for both HDS and HDN takes the form:

$$-r_i = -\frac{dC_i}{dt} = k_i C_i^{\,n} \qquad \textbf{(2.15)}$$

where C_i = concentration of species i (S or N) in petroleum fraction, k_i = apparent rate constant of species i, n = reaction order, and t = residence time. Integrating and solving equation 2.15 yields three solutions depending on value of n as follows:

$$\boxed{C_f - C_p = \frac{k_i}{LHSV} \qquad for\ n = 0} \qquad \textbf{(2.16)}$$

$$\boxed{\ln\left(\frac{C_p}{C_f}\right) = -\frac{k_i}{LHSV} \qquad for\ n = 1} \qquad \textbf{(2.17)}$$

$$\boxed{\left[\frac{1}{C^{n-1}{}_p} - \frac{1}{C_f^{\,n-1}}\right] = (n-1)\frac{k_i}{LHSV} \qquad for\ n \neq 0,1} \qquad \textbf{(2.18)}$$

where r_i = the rate of change in the heteroatom concentration, k_i = the apparent rate constant, C_f and C_p = concentrations of heteroatoms i (S or N, wt.%) in feed and hydrotreated products, respectively, and $LHSV$ = liquid hourly space velocity (i.e. the inverse of residence time). The apparent rate constant is used in the above kinetic expressions since it takes into account the effect of diffusion due to mass transfer limitations. The main kinetic parameters that can be obtained from power law model are: the reaction order (n) and the apparent rate constant (k_i).

The activation energy, defined as the minimum amount of energy that must be overcome in order for a chemical reaction to proceed or start the reaction can then be determined by the Svante Arrhenius equation:

$$E_a = -RT \ln\left(\frac{k_i}{k_o}\right) \qquad \textbf{(2.19)}$$

or can be expressed as:

$$k_i(T) = k_o e^{-E_a/RT} \qquad \textbf{(2.20)}$$

where: k_o = pre-exponential factor; k_i = apparent rate constant; E_a = activation energy (kJ/mol); R = universal gas constant (kJ/mol.K); T = temperature (in Kelvin).

For the hydrotreating of gas oil applications, the power law model has been used to predict reaction orders in the range of 0.5 to 1.5 for HDN reactions (Bet et al., 2001; Callejas et al., 1999). The reaction order for HDS mostly varies considerably with changes in the feedstock compositions. Specifically, a trend of increasing molecular weights for organic sulfur compounds corresponds to an increasing order for the overall HDS reaction (Anchyeta et al., 2002). Based on the power law model, kinetics studies of model feeds generally follow first order (Speight, 2000; Girgis and Gates, 1991; Anchyeta et al., 2002). For real feeds, the reaction order depends on the type of feed and the catalyst, and can range between 1.0 – 2.5 for HDS and 1.0 – 2.0 for HDN (Anchyeta et al., 2002; Aoyagi et al., 2003). A summary of kinetic studies of real feedstocks from the open literature are presented in Table 2.2.

Table 2.2: Some literature data of reaction orders and activation energies for heavy petroleum fractions

References	Feed boiling range (°C)	Kinetic model	Reaction order		Activation energy, kJ/mol	
			HDS	HDN	HDS	HDN
Boahene et al., 2011						
Mapiour et al., 2009	260-592	P-L	2.0	1.5	101	79
Mapiour et al., 2009	260-592	L-H	1st pseudo	1st pseudo	99	69
Mapiour et al., 2009	260-592	M-P	2.68	2.02	119	112
Ferdous et al., 2006	185-576	L-H	1.0	1.5	87	74
Yui et al., 2006	286-541	P-L	1.5	1.0	151	132
Duan et al., 2005	214-559	M-P	1.5	1.6	141	94
Botchwey et al., 2004	210-600	L-H	1st pseudo	1st pseudo	114.2	93.5
Marin et al., 2002	LGO/SRGO	P-L	1.5	1.5	77.8	64.2
Bej et al., 2001 a	210-655	P-L	1.5	-	-	-
Bej et al., 2001 b	210-655	P-L	-	2.0	80	-

2.4.2 Langmuir-Hinshelwood Models

As a result of the diverse nature of composition of compounds present in petroleum fractions, application of the simple power law equation might not give the actual representation of the kinetic behavior of the system. Furthermore, the different reactivities of these compounds result in different rates of adsorption on the catalyst surface. This contributes to the margin of error of kinetic parameters obtained from the power model since it does not account for the competitive adsorption rates of the various species in the petroleum fraction. The Langmuir-Hinshelwood model takes into account the percentage of catalyst active sites that are occupied by the adhered reactant at steady state, as well as the percentage of sites that are vacant or inhibited by other adhered compounds from the feed stream. Thus the Langmuir-Hinshelwood models give better kinetic representation of the HDS and HDN as compared to the power law model. However, the use of the Langmuir-Hinshelwood type of kinetic modeling of feed is very complicated due to the many coefficients that need to be determined and the resulting difficulty of their determination (Botchwey et al., 2006; Mapiour et al., 2009).

The development of the Langmuir-Hinshelwood model was based on mechanistic steps as outlined in the following (Mapiour et al., 2009; Owusu-Boakye et al., 2005):

1. Adsorption of reactants onto the active sites present on the surface of the catalyst.

2. Surface reaction between the adsorbed reactants on the catalyst's surface and reactants present from bulk fluid or between adsorbed reactants on the surface of the catalyst.
3. Products desorption from the active sites into bulk solution.

Various forms of expression of the Langmuir-Hinshelwood model exist in the open literature. However, the most frequently cited rate equation used to model the HDS and HDN reaction kinetics is as follows (Mapiour et al., 2009; Owusu-Boakye et al., 2005; Botchwey et al., 2006):

$$-r_i = -\frac{dC_i}{dt} = \frac{k_i K_i K_{H2} P_{H2} C_i}{1 + K_i C_i + K_{H2} P_{H2} + K_{H2S} P_{H2S}} \qquad \textbf{(2.21)}$$

where $-r_i$ = reaction rate of species *i* (S or N); K_i, K_{H2}, K_{H2S} = adsorption equilibrium constants of species i, H_2 and H_2S; k_i = apparent rate constant (which is defined by equation 2.20).

Assumptions that are considered in the above model development include:

- Reactions occurring at the surface of the catalyst are the rate-limiting.
- All reactions are pseudo-first order.
- Reactions occur in a plug-flow regime with negligible axial dispersion.
- Both HDS and HDN reactions are inhibited by the presence of H_2S.

The solution obtained for the model by using Maple V software to solve equation 2.22 is as follows:

$$C_i(t) = \frac{(1+K_{H_2}P_{H_2}+K_{H_2S}P_{H_2S})\,\text{LambertW}\left(K_i \exp\left(\frac{\left(t+\frac{C_{io}K_i+\ln(C_{io})+\ln(C_{io})K_{H_2}P_{H_2}+\ln(C_{io})K_{H_2S}P_{H_2S}}{K_{H_2}P_{H_2}K_ik_i}\right)K_{H_2}P_{H_2}K_ik_i}{1+K_{H_2}P_{H_2}+K_{H_2S}P_{H_2S}}\right)\right)}{K_i}$$

where:

$$\text{LambertW}(x) = x - x^2 + \frac{3}{2}x^3 - \frac{8}{3}x^4 + \frac{125}{4}x^5 - \frac{54}{5}x^6 + (0)^7$$

and **(2.22)**

$$x = \left(K_i \exp\left(\frac{\left(t+\frac{C_{io}K_i+\ln(C_{io})+\ln(C_{io})K_{H_2}P_{H_2}+\ln(C_{io})K_{H_2S}P_{H_2S}}{K_{H_2}P_{H_2}K_ik_i}\right)K_{H_2}P_{H_2}K_ik_i}{1+K_{H_2}P_{H_2}+K_{H_2S}P_{H_2S}}\right)\right)$$

The above equations can then be solved with Excel solver. A trial-and-error approach can be used to obtain the apparent rate constants and adsorption equilibrium constants (Ferdous et al., 2006). The partial pressures of H_2 and H_2S can be obtained from HYSYS analysis.

2.4.3 Multi-parameter Model

This kinetic model is similar to the generic power law model. However, to improve the degree of accuracy of kinetic parameters obtained from the power law model, additional hydrotreating operating conditions namely hydrogen partial pressures and gas/oil ratio are taken into consideration in the overall rate expression as well as LHSV and temperature. Obviously, this model would give a better representation of the kinetics of the hydrotreating reaction due to the fact that the effect of process variables can be observed. The multi-parameter model is shown below in equation 2.23 (Mapiour et al., 2009; Duan et al. 2005):

$$-r_i = -\frac{dC_i}{dt} = -k_i \times P_{H2}^m \times C_i \times \left(G/O\right)^q \qquad \textbf{(2.23)}$$

The solutions for equation 2.23 for different values of n are given below:

$$\ln\left(C_f/C_p\right) = \frac{k_o \times e^{(-s/T)} \times P_{H2}^m \times \left(G/O\right)^q}{\left(LHSV\right)^c}; n = 1 \qquad \textbf{(2.24)}$$

$$\frac{1}{n-1}\left[\frac{1}{C_p^{n-1}} - \frac{1}{C_f^{n-1}}\right] = \frac{k_o \times e^{(-s/T)} \times P_{H2}^m \times \left(G/O\right)^q}{\left(LHSV\right)^c}; n > 1 \qquad \textbf{(2.25)}$$

where: C_f and C_p = the nitrogen or sulfur concentrations in feed and product, respectively; k_o = pre-exponential factor; s = E_a/R, where E_a = activation energy and R = gas constant; n = reaction order; m, q, and c = empirical regression factors. P_{H2} = reactor pressure; G/O = gas-to-oil ratio; LHSV = liquid space velocity.

2.5 Hydrotreating catalysts

The use of catalysts in any industrial chemical reaction is primarily to accelerate the reaction. Characteristics of various catalysts make it possible for the formation of bonds with the reacting molecules (i.e. adsorption), such that they can react toward a particular product formation, which detaches itself from the catalyst surface (i.e. desorption), and leaves the catalyst unaltered so as to render its surface regenerable for the interaction with the next set of molecules. In fact, the catalytic reaction can be described as a cyclic process (van Santen et al., 1995), in which the catalyst participates in the reaction and is recovered in its original form at the end of the cycle. A catalyst cannot alter the chemical equilibrium of a given reaction; it only creates a favorable reaction pathway. This is done by decreasing the activation energy barrier ($E_{a,\ cat}$) compared to the gas phase reaction ($E_{a,\ gas}$) and thus increasing the reaction rate (see Figure 2.6) (Coulier, 2001).

Consequently, the reaction can take place at lower temperatures and pressures, which decreases costs and amounts of energy for e.g. a chemical plant. Furthermore, if for a certain reaction, different paths are possible that lead to various products formation, the catalyst can selectively decrease the activation energy of one of the possible reaction paths, thereby altering the selectivity of the reaction. In general, a successful catalyst increases the yield of the desired product while decreasing that of other products, which has advantages for both economic and environmental reasons (van Santen et al., 1995).

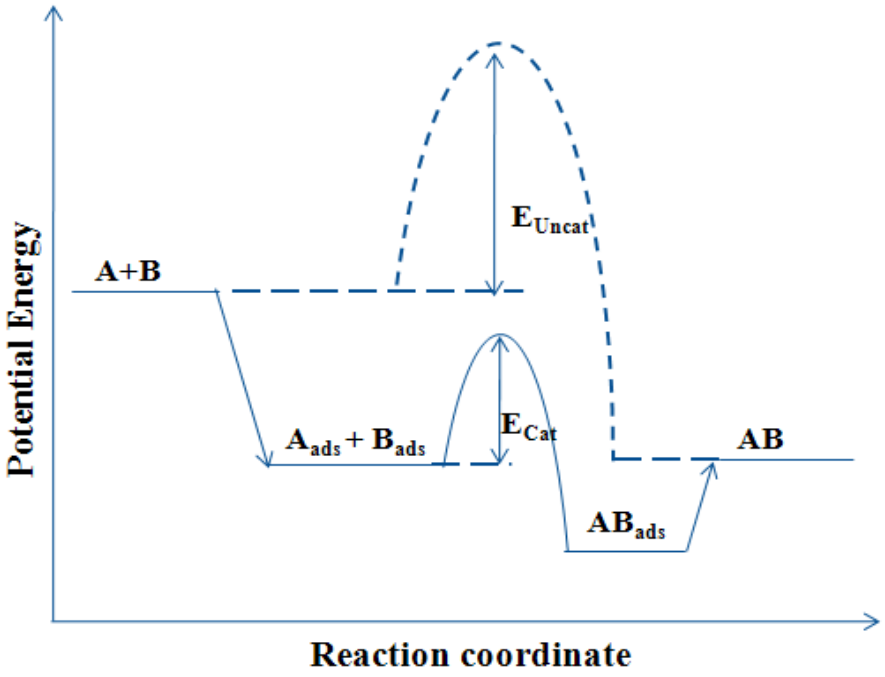

Figure 2.6: A typical potential energy diagram for a heterogeneous catalytic reaction and non-catalytic reactions

The principal roles of the hydrotreating catalysts is to promote the removal of undesired feed constituents such as sulfur, nitrogen, and metals up to specified levels and also to increase the rate at which the overall hydrotreating reactions of interest approach complete conversion. Typical characteristics of all types of hydrotreating catalysts are that they are high surface area pellets consisting of an active component (i.e. Mo or W) and one or more promoters (eg. Ni, Co, Fe). These materials exist in the form of nanometer-sized particles that are dispersed on the surface of a catalyst support.

The type of catalysts used for hydrotreating processes is mainly dependent on the specific reaction and process requirements. In general, catalysts for hydrotreating reactions consist of mixed sulfides of CoMo, NiMo, or NiW supported on high

surface area carriers. Generally, whereas NiMo sulfide catalysts are excellent in hydrodenitrogenation (HDN) and hydrogenation (HYD) reactions, CoMo sulfides are effective for hydrodesulfurization (HDS) reactions (Topsoe et al., 1996). For most industrial applications, the commonly used active phase for hydrotreating catalyst is MoS_2. Preparation of this active phase mostly follows the incipient wetness impregnation technique in which Mo present in the form of aqueous ammonium heptamolybdate solution is dispersed onto a high surface area catalyst support (e.g. Al_2O_3, SBA-15, etc). This is then dried and calcined after which the oxidic MoO_3 species is formed. It is known that the hydrotreating catalysts in their oxidic state are not active or selective enough to perform their required functions (i.e. make their required cuts). Thus to make them more active and selective, they must be sulfided (Gaylord, 2007).

The oxide form of the catalyst is transformed to the sulfidic state by reduction and reaction with sulfur, usually in a hydrogen environment *in situ* the reactor via a sulfidation process. The sulfidation process is normally carried out using H_2S or a specialized sulfidation solution containing a low-boiling sulfur compounds such as dimethyl di-sulfide, carbon-di-sulfide and butanethiol (Vishwakarma et al., 2007) Sulfidation is commonly done within a temperature range of 180-350 °C and a pressure greater than 1.0 MPa. For real feed operations, the commonly used temperatures are 193 and 343°C at 9.0 MPa (Speight, 2000). Prior to sulfidation, if a considerable amount of the oxidic precursor exists in the form of MoO_2, then there is the likelihood that a greater percentage of the oxide catalyst will remain unconverted

into the sulfide phase, and the catalyst will not achieve its maximum potential activity (Satterfield, 1991).

Tungsten sulfide (WS_2) is another active phase commonly used in hydrotreating applications. A similar preparation procedure is followed as in MoS_2 phase formation by using aqueous ammonium metatungstate salt precursor for the support impregnation. Tungsten sulfide is commonly accepted to provide less HDS and HDN activity than molybdenum sulfide, but can perform better aromatic and olefin hydrogenation (Frank et al., 1981). For instance, NiW sulfide catalysts are very promising for hydrocracking of aromatics, hydrogenation at low H_2S concentrations and conversion of alkylated dibenzothiophenes, whereas supported noble metal catalysts such as platinum or palladium are used for sulfur and nitrogen-free feedstock due to their high hydrogenation activity (Stanislaus et al., 1994). However, these noble metal catalysts are sensitive towards poisoning by sulfur compounds. Interestingly, CoW sulfide catalysts seem somehow not to be a good combination for application in industrial hydrotreating processes. In general, the characteristics of the feedstock and the desired product specifications will determine which catalyst (or combination of catalysts) to be used.

As a common practice, the industrial hydrotreating catalyst is formulated with metal promoters to facilitate the synergistic effect between active components to increase the HDS and HDN activity of the catalysts. Cobalt and nickel are the most common metals used to serve this purpose in conjunction with molybdenum or tungsten to give a bimetallic catalyst. It is a common rule of thumb that the maximum

catalytic synergy is achieved when the molar ratio of the promoter to the total catalyst metals present in a given ratio (i.e. Co(Ni)/[Co(Ni) + Mo(W)] ≈ 0.3). This metal proportion holds relatively constant for all types of hydrotreating catalysts (Gates et al., 1979).

For most industrial hydrotreating applications, the catalyst support mostly employed is γ–Al_2O_3, irrespective of the catalyst metals chosen for a hydrotreating application. A major role of the catalyst support is to provide a high surface area for the homogeneous dispersion of metal species and also to provide a defined pore structure so as to facilitate the diffusion of variable size molecules present in the petroleum fractions.

2.5.1 Active components

The most commonly used active components for industrial hydrotreating applications include MoS_2 or WS_2. The coordination geometry of these MS_2 (where M = Mo or W species) active phases are such that each M (IV) atom is surrounded by a trigonal prismatic coordination of sulfur atoms, with each sulfur atom adjacent to a pyramidal geometry of molybdenum atoms (Wypych et al., 1992). For instance, the morphology of MoS_2 phase on the surface of a catalyst support as observed by Satterfield et al, 1991 was believed to compose of layered hexagonal crystal structure with weak interactions occurring between the sulfur atoms in the connecting layers; forming hexagonal layers of stacks of the crystallite. Similarly, the tungsten sulfide (WS_2) phase has identical layered crystal structural morphology as the active catalytic phase.

Despite the enormous amount of research work on hydrotreating catalysts over the years, the structure of the active phase has been a matter of great debate. Although the presence of MoS_2 and WS_2 slabs has been generally accepted, the function and location of the promoter (Co or Ni) was the main subject of debate (Coulier, 2001). Many researchers have proposed theories to facilitate the explanation of synergy existing between the active phase metals and sulfur that make these crystal structures effective catalysts for hydrotreating reactions (Voorhoeve et al., 1971; Farragher et al., 1973; Delmon et al., Ratnasamy et al., 1980; Topsoe et al., 1983). The most simplified model developed by Daage and Chianelli (1994) attempts to explain how the morphology of the MoS_2 or WS_2 crystal structure affects the reaction pathway selectivity (hydrogenation versus direct desulfurization) of the overall hydrodesulfurization reaction. This "rim-edge" model as depicted in Figure 2.7, illustrates this reactivity concept. The selectivity of the process is dependent on the stack height of the metal sulfide slabs of a given diameter *d*, which is attainable by varying the ratio of rim sites to edge sites. The theory suggests the rim sites are active in hydrogenation and C-S bond breaking, while edge sites participate only in C-S bond breaking. The basal plane consists entirely of sulfur atoms and is considered dormant.

Eijsbouts et al. (1997) reviewed the various structural models for CoMoS based on the fact that catalysts are dynamic and flexible while small clusters of Co-sulfide particles are present at higher ratios. In the extreme case of very high Co/Mo

ratios, Co_9S_8-like particles decorate the MoS_2- slabs, corresponding structurally to the contact synergy model (Eijbouts, 1997).

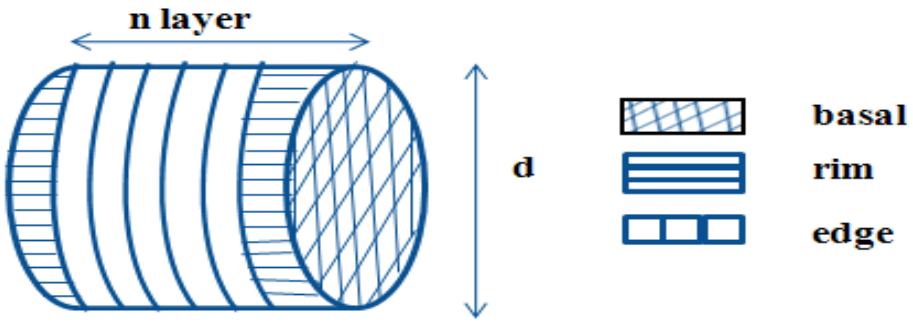

Figure 2.7: Illustration of the "rim-edge" model (Chianelli et al., 2009).

For commercial catalysts the Co/Mo ratio lies between the two extreme cases, hence usually a distribution of Co sulfide particles with different particle size and ordering is present on these catalysts (see Figure 2.8).

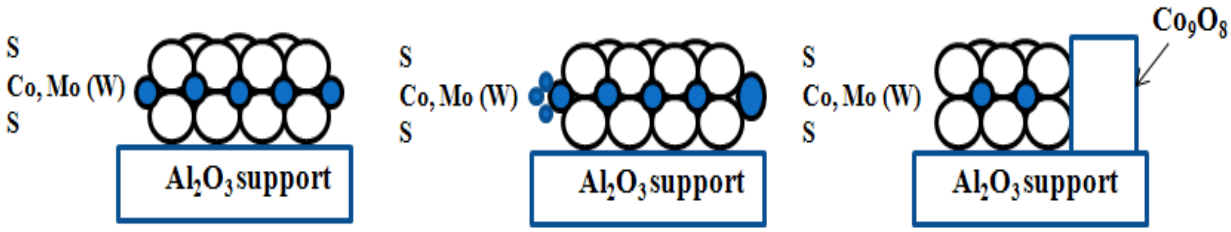

CoMoS model:

- Co atoms on the edges of MoS_2 slabs
- Low Co/Mo ratio

Actual situation:

- Co sulfide with different particle size and/or ordering
- Medium Co/Mo ratio

Contact synergy model:

- Co_9O_8 bulk sulfide in contact with MoS_2 slabs
- High Co/Mo ratio

Figure 2.8: Relation between different proposed models for the active phase in CoMo(W) catalysts (Coulier et al., 2001).

Figure 2.9 shows that the CoMoS phase is not the only species present on commercial $CoMo/Al_2O_3$ catalysts (Topsoe et al., 1996). The figure shows that besides the active phase, i.e. the CoMoS phase, bulk Co sulfide, unpromoted MoS_2 and $Co:Al_2O_3$ interacting species are likely to be present, indicating that characterizing these catalysts is not straightforward.

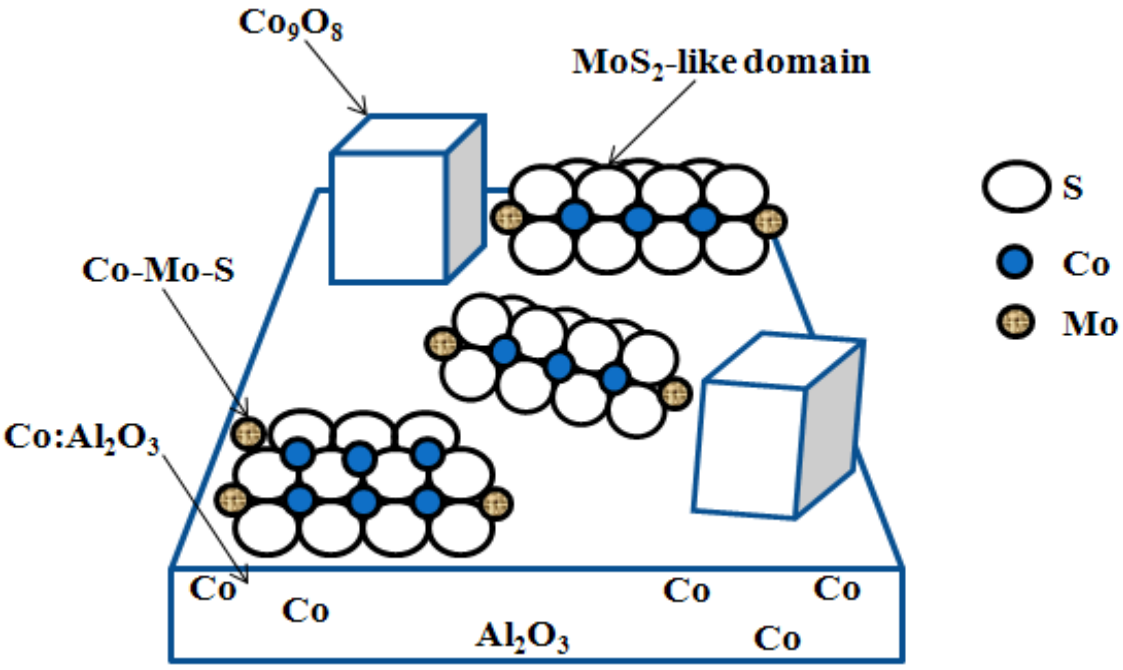

Figure 2.9: Schematic picture of different phases present in sulfided alumina-supported CoMo catalysts (Adopted from Coulier et al., 2001).

The two main structures proposed for the CoMoS phase present on $CoMo/Al_2O_3$ are namely: type I phase (i.e. CoMoS I) and type II phase (CoMoS II). The type I is mostly thought to be incompletely sulfided and to consist mainly of MoS_2 monolayers interacting with the support via Mo-O-Al bonds (Coulier et al., 2001). CoMoS II phases are thought to be fully sulfided and consist often of stacked

MoS_2 particles that are only weakly interacting with the support via van der Waals interactions. It has been reported that the CoMoS II phase is twice as active as CoMoS I in gas phase thiophene HDS (van Veen et al., 1993; Bouwens et al., 1994). Similarly, for dibenzothiophene HDS in trickle flow, CoMoS I was found to be more active than CoMoS II (van Veen et al., 1982). However, since the difference in activity between CoMoS I and CoMoS II is dependent on the reactivity of heteroatoms present in the feedstock, this conclusion may not be drawn as in the case of model compound applications.

For unpromoted catalysts the active sites are believed to be located at the MoS_2-edges and consist of coordinately unsaturated Mo sites (CUS), i.e. sulfur anion vacancies (Gaylord, 2007). These sites are also believed to be relatively more active in hydrogenation (HYD), than the active sites in promoted catalysts (Coulier et al., 2001). The rim edge model of Daage and Chianelli (1994) states that for stacked MoS_2 layers, the top and bottom layer, i.e. rim sites, are responsible for both HYD and HDS, whereas the intermediate layers, i.e. edge sites, are only responsible for HDS. The model indicates that the rim and edge sites consist of molybdenum/tungsten atoms that are accessible to reactants due to sulfur anion vacancies in the metal sulfide crystal structure. These unsaturated sites, or active sites, are continually generated and degenerated by sulfur atoms reacting with the H_2 of the hydrotreating system to release H_2S in a reversible reaction. Sulfur or nitrogen heteroatoms from the feedstock molecules continuously bind to these active sites. These molecules potentially undergo some extent of hydrogenation (essential to

HDN) if adsorbed at a rim site before the molecule is released back into the hydrotreating system. The removed heteroatom remains to saturate the active site, and the process repeats itself.

The high activity of promoted catalysts as explained by the IR measurements of NO adsorbed on the catalyst conducted by Topsøe et al. (1996) suggested that the metal-sulfur bond strength in CoMoS is lower than that in MoS_2, which could be the reason for the promoting effect of Co. A bond-weakening effect has also been reported by Byskov et al. (1997) using theoretical calculations to confirm the weakening of the Mo-S bond by Co enabling the easy creation of surface vacancies.

In the case of nitrogen heteroatoms, the atoms are strongly adsorbed and difficult to remove by NH_3 production; thus acting as a poison to the active catalyst sites. This model suggests that the extent of hydrogenation that occurs in a hydrotreating process can be predicted by the number of metal sulfide layers (*n*) that make up each hexagonal stack. From this theory, catalysts with predominantly single layer metal sulfide structures will have a greater selectivity for hydrogenated organic molecules, while increasing catalyst particle sizes will result in less extensive hydrogenation.

2.5.2 Promoters

The catalytic performance of the active phase can be markedly improved by the incorporation of a second (or sometimes third) transition metal in relatively small amounts during the catalyst formulation so as to impart better catalytic activity, selectivity, and stability. Such transition metals generally referred to as promoters,

commonly used for the hydrotreating catalyst applications include cobalt (CoMo) and nickel (NiMo). Another promoter seldomly used is Fe. Iron compounds are commonly used as powdered or impregnated additives, due to their low cost. For example, iron oxide forms iron sulfide *in situ*, and help to promote hydrogen transfer reactions (Gray, 1994). The promoter mostly has the effect of substantially increasing (approximately 100-fold) the activity of the active metal sulfide (Gruia, 2006).

On performance basis, the "rim-edge" model does not explain the influence of doping of such promoters (Co and Ni) on the overall catalytic performance of MoS_2 and WS_2 hydrotreating catalysts. Various researchers have proposed theories to explain the role of promoters to the synergy exhibited by hydrotreating catalysts. The remote control or contact synergy theory, and the edge decoration or "CoMoS" theories are the two most widely discussed theories in the open literature. Delmon and associates (Hagenbach et al., 1973) proposed that interactions between separate MoS_2 and Co_9S_8 sulfide phases on a CoMo catalyst surface were created from their close proximity. These interactions were described as their "contact synergy". In this model, the physical contact between separate MoS_2 and Co_9S_8 crystallites provides an explanation for the promotional effect, the first one causing spill–over hydrogen that increases the activity of the MoS_2 phase (Delmon et al., 1990). This control mechanism gives an indication that organosulfur molecules would be adsorbed at MoS_2 active sites before reacting with dissociated hydrogen atoms arriving from the Co_9S_8 active sites. Although this theory is less accepted today compared to the edge decoration model, it does provide the concept of synergy/cooperation between two

separate sulfide phases as opposed to a second metal simply promoting the activity of a metal sulfide (Chianelli et al., 2009).

Ratnasamy and Sivasanker suggested that promoter ions are located at the edges of the MoS_2 layers (Ratnasamy et al., 1980). This edge decoration model was then experimentally proven by Topsøe and Topsøe on the basis of IR studies of NO molecules adsorbed on these catalysts. By employing Mössbauer Emission Spectroscopy (MES), Topsøe et al. (1981) assigned a specific Co signal to a so–called 'Co–Mo–S' interaction phase different from Co_9S_8. Electron microscopy is an excellent tool to visualize the MoS_2 structures (monolayer vs. multilayer) (Lauritsen et al., 2007). The section of the monolayer MoS_2 slab shows what possibly is a Co atom at the periphery of the MoS_2 (Craje, 1992). ^{57}Co Mössbauer Emission Spectroscopy (MES) is applied to study the local structure of Co in this type of catalysts and can be used as a fingerprint for different Co phases (Hughes, 1984). The Quadrupole Splitting (QS) values for the different Co phases (i.e., Co_9S_8, 'Co–Mo–S' and cobaltaluminate) were used to identify these phases present of the catalyst (Furimsky, 2007).

Wivel et al. (1984) also observed a linear correlation between the amount of Co promoter ions present in this 'Co–Mo–S' phase and the thiophene HDS activity and theorized that the activity of the bimetallic catalysts originates from a separate phase created between the promoter, the active component, and the sulfur active phase. It is accepted that the highest catalyst activity is achieved when Co and Ni metals in their sulfide phase are doped along the outer surface area of the MoS_2 and

WS_2 hexagonal slabs. The Co and Ni atoms substituted into the Mo and W positions within the crystal lattice exclusively along the exterior of the metal sulfide particles. These substituted metal promoters create a crystal phase between the active component and active phase (i.e. Mo/W and S), which was referred to as the "CoMoS" phase (Zandbergen et al., 1997). Scanning tunneling microscopy studies have been performed to verify this theory, providing atomic-scale images of active MoS_2 nanoclusters promoted by both Co and Ni at the edge and rim sites (Craje, 1992). This theory has become the most widely accepted method of explaining the function of catalyst promoters in hydrotreating.

2.5.3 Catalyst deactivation

One major issue associated with the use of heterogeneous catalysts is the loss of catalytic activity and/or selectivity with time on stream. Similarly, hydrotreating catalysts undergo this same deactivation phenomenon, leading to the gradual loss of the catalyst's ability to produce the desired specifications product unless reactor temperatures are increased (or feed rate is decreased) (Gruia, 2006). However, increasing the reactor temperature to compensate for catalyst deactivation as the run progresses has considerable costs implications in industrial hydrotreaters. A critical cause of deactivation of catalysts is related to coverage or loss of catalyst active sites. This catalyst deactivation phenomenon has been classified by Hughes et al (1984) based on reasons causing loss of catalyst activity as: 1) poisoning of catalysts by impurities (i.e. S or N) present in the reaction mixture; 2) sintering of the catalyst; 3) changes in catalytic activity initiated by intermediate formations (e.g. carbocations)

which are a constituent part of the mechanism. It should be noted that if not stabilized, carbocations can combine to higher molecular weight species and eventually to coke (Barholdy et al., 1993; Sigurdson et al., 2009).

In the long run, deactivation of HDS catalysts can be divided into three regimes: the initial rapid fouling caused by coke, the subsequent gradual fouling by metal and the final catastrophic fouling by pore mouth plugging (Ledoux et al., 1990; Maity et al., 2008). Furimsky and Massoth (1999) also summarized the four basic factors responsible for the deactivation of catalyst as follows:

1) Active site poisoning by a strongly adsorbing species (i.e. nitrogen).
2) Active site coverage by deposition (i.e. coke, nickel, vanadium).
3) Pore mouth constriction and/or blockage from coking.
4) Sintering of the active phase.

A rapid deactivation of the catalyst occurs during the initial stages of the hydrotreating reaction. This has been attributed to the formation of "soft" coke that quickly reaches equilibrium levels during the early part of the catalyst cycle (Gruia, 2006). During the rest of the cycle, the total amount of coke remains almost constant, however further structural changes occur to produce what is often referred to as 'hard' coke. Thus, the observed catalyst deactivation during a cycle is primarily the result of structural changes to the coke rather than an actual marked increase in the total amount of coke. Continued deactivation over the course of the operation is due to pore constriction from coke formation and from feed contaminants, either through metal deposits or adsorbed nitrogen. Since the catalyst life is determined mainly by

the length of middle-of-run (MOR), the catalyst deactivation rate at the MOR is the most important (Maity, 2008). Finally, catastrophic losses in feed conversion occur when ultimate pore blockage occurs for the catalyst support.

HDS catalysts are poisoned as a result of strong adsorption of predominantly N-based compounds onto the coordinately unsaturated sites (Sigurdson et al., 2009), even though compounds such as organic sulfur and oxygen may also contribute to active site poisoning. Catalyst active site poisoning may be reversible or irreversible, depending on the characteristics of the feed and the operating conditions (Furimsky et al., 1999). Irreversible poisoning is the result of polymer formation that occurs around the adsorbed nitrogen heteroatom. For the case of Athabasca bitumen-derived gas oils, considerable organonitrogen concentrations poison not only the HDN reactions, but the HDS reactions as well. For these gas oils, the nitrogen compounds appear to simply enhance the initial rapid deactivation from coke formation before reaching pseudo steady-state conditions (Luck, 1991).

Catalyst deactivation caused by the deposition of metals is not reversible (Gruia, 2006). The metals may come into contact with the catalyst via feedstock contaminants namely as Pb, Fe, As, P, Na, Ca, Mg, or as organo-metallic compounds in the feed primarily containing Ni and V. The deposition of Ni and V takes place at the pore entrances or near the outer surface of the catalyst, creating a 'rind' layer, which eventually blocks access to the interior part of the catalyst, where most of the surface area resides (Gruia, 2006). Hydrodemetallization (HDM) reactions are carried out to remove these metals so as to reduce their poisoning effects on downstream

catalysts. A deleterious aspect of catalyst deactivation by metal deposition is that unlike nitrogen poisoning, the metal deposition does not reach a steady-state but continuously builds during the course of a hydrotreating run (Breysse, 2008). As compared to crude oils derived from Maya (with high nickel and vanadium concentrations up to 0.01 wt.% and 0.05 wt.%, respectively), the contents of these metal contaminants do not pose significant problems in the hydroprocessing of Athabasca bitumen-derived gas oils (Luck, 1991; Besenbacher et al., 2008).

Unlike deactivation of the hydrotreating catalyst by active site poisoning and by metals deposition, which are vastly dependent on the characteristics of feedstock being handled and not directly dependent on the textural properties of the catalysts, the choice of catalyst support plays a significant role in the catalyst deactivation resulting from pore constriction/blockage and active phase sintering. By employing catalysts of improved textural properties such as larger pore diameters and high surface area, issues of pore constriction and blockage by coke formation as well as catalyst particles sintering or agglomeration can be resolved. The larger pore diameters provide sufficient room for the diffusion of bulky molecules into active sites located inside the pores while high surface area enhances the dispersion of catalyst metals with minimal interaction effects with the metal oxide precursors. Thus the discovery of support materials with some of the aforementioned desirable textural properties has attracted the interest of various researchers in this field of study over the past decade.

2.5.4 Support Materials

Catalyst supports principally provide the required platform for homogeneous dispersion of metal nanoparticles. The support material may or may not take part in the catalytic reaction. The support is usually a surface such as a metal oxide or carbon material. The support and catalyst may bond together in such a way to enhance the reactivity of the catalyst; in other cases, the support may be inactive and provide a high surface area substrate to increase the collisions of the reactants with the catalysts.

The majority of all metal sulfide hydrotreating catalysts are distributed as adsorbed particles over a catalyst support structure before being applied as pellets in a hydrotreating reactor. The distribution of the adsorbed nanoparticles over the high surface support enhances the activity of the catalyst by increasing the exposure of the active sites to the reactants while still maintaining the mechanical strength of the material. As previously stated, γ-alumina is almost exclusively used as a hydrotreating catalyst support in industry. Significant efforts have been made in an attempt to improve upon the effectiveness of alumina. Important characteristics of an effective catalyst as outlined by Luck (1991) are as follows:

1) Improving the dispersion of the bimetallic sulfides.
2) Reducing the strong interaction between the active component and the support while the active component is in the initial oxide phase.
3) Decrease the spinel phase concentration of γ-alumina, increasing the usability of the catalyst promoters.
4) Improve the recovery potential for catalyst metals.

5) Reducing catalyst deactivation from coke formation.

Improvement of the dispersed bimetallic sulfides on a higher surface area catalyst support as compared to the conventional γ–Al_2O_3 support would result in increased catalytic activity. Porous materials such as zeolites, MCM-41, HMS, SBA-15, etc., have been known to have surface areas that far exceed those of commercial γ–Al_2O_3 supports. However, a very critical question that intrigues discussion is whether most of these surface areas are accessible by the molecules of petroleum fractions being processed. Furthermore, a candidate for an effective catalyst support should be able to address the issue of strong metal-support interactions (SMSI) between the catalyst metal oxide precursors and the support, that is the prevailing problem of the commercial γ–Al_2O_3 supports. Due to the strong metal-support interactions, the complete sulfidation and activation of the oxidic catalyst becomes difficult, resulting in the formation of metal aluminates (Lauritsen et al., 2007; Netzel et al., 1996). The strong surface interactions also contribute to the rapid catalyst deactivation occurring due to sintering of the catalyst's active phase (Kabe et al., 1999). Moreover, hydrotreating catalysts contain sulfur, as the metals are in a sulfide form (Gruia, 2006). Thus, it would be beneficial to have a support that could be easily separated from the catalyst to provide recovery of the metals once the catalyst itself can no longer be effectively regenerated. When regenerating catalysts after extensive deactivation has occurred, it is impossible to achieve the initial activity of the fresh catalyst due to sintering effects (Song, 2002). However, recovering the catalyst metals from the alumina support is a difficult procedure. Finally, researchers have

underscored the fact that by improving the pore diameters of the catalyst support, a reduced effect of pore mouth constriction mainly caused by coke formation can be achieved (Kwak et al., 1999).

2.6 Effect of catalyst support and hydrotreating

A growing interest in the removal of sulfur from gasoline and diesel oil by means of deep hydrodesulfurization (DHDS) is due to the implementation of more stringent fuel specifications in order to reduce exhaust emissions. The requirement of production of ultra-clean diesel fuel with low sulfur content (less than 50 ppm) makes imperative the development of new hydrotreating catalysts, highly active and selective for hydrodesulfurization (HDS) of the refractory polyaromatic sulfur compounds (Clausen et al., 1996; Breysse et al., 2003; La Parola et al., 2002). In order to achieve this goal, different approaches have been tried, for example, the use of novel supports (carbon, TiO_2, TiO_2–Al_2O_3, MCM-41, etc.) and of novel active phases (noble metals, transition metal phosphides, etc.) or the incorporation of additives in the formulation of conventional HDS catalysts (Topsoe et al., 1984; Shimada et al., 1988; Dhar et al., 2000; Lee et al., 2005). Development of novel supports seems to be an interesting and practical option because the supports nature and characteristics play an important role in the catalytic activity. Support plays an important role in determining nature and number of active sites, and consequently, in the activity of the catalysts. With a view to find out better materials for supporting active components such as Mo and W, a wide variety of materials have been evaluated for their

suitability as support especially with reference to hydrotreating and related reactions (Breysse et al., 1991).

The efficiency of a hydrodesulfurization catalyst is markedly affected by the interaction between the active phases and the support. Metal–support interactions influence not only the dispersion of the active components, but also their reducibility and sulfidability. For instance, metal-support interactions affect the morphology of the sulfide active phase and interactions of chemical environment of acid sites. The development of new supports for hydrotreatment catalysts have been actively urged due to stringent regulations concerning the restricted level of sulfur admitted in fuels. Some results have been summarized in reviews and open literatures concerning hydrotreatment catalyst and deep hydrodesulfurization. Moreover, it is also well known that hydrotreating catalyst undergoes significant structural changes during the sulfidation (Rana et al., 1999), which depends on the nature of support as well as the method of catalysts preparation (Dhar et al., 2003). Thus, nature of the support is of great importance to the design of the hydrotreating catalyst. By means of an adequate support design, it is possible to significantly increase the HDS, HYD and HDN functionalities of hydrotreating catalysts. Semiconducting supports like TiO_2 can improve the HDS and HYD activities by exerting electronic effects on the active phase, leading to the formation of sulfur vacancies. Alumina support modified by SiO_2 can facilitate the sulfidation of the active species, leading to better-promoted type II active sites with increased HDS and HYD catalyst functionalities. The nature

of the support affects the sulfidation and dispersion of HDS catalysts even when chelating agents are used during catalyst preparation.

In the past, it was considered that the hydrotreating catalyst support is inert. However, this is not always true but in many cases the support interacts with the active component leading to beneficial or detrimental effect on catalytic activity. The earlier view that the role of the support in hydrotreating catalysts was just to stabilize the active component as small particles, thus increasing the dispersion without influencing the catalyst activity has drastically changed in the light of different studies that have shown that the rate and selectivity of hydrotreating reactions over sulfided NiMo (W) or CoMo (W) catalysts are significantly affected by the support nature (Han et al., 2001; Trong-On et al., 2001; Kooyman et al., 2003; Linares et al., 2008).

The recent discoveries of various mesoporous molecular sieves such as HMS, MCM-41 and SBA-15 have brought a new dimension to the design of catalysts due to the flexibility they offer in pore diameters fine-tuning during their synthesis. Their potential is currently under intense study in a very large variety of catalytic applications such as hydrotreating. Other desirable properties these materials posses include high surface area, large and uniform cylindrical mesoporous channels and high hydrothermal stability. That notwithstanding, each of the aforementioned supports has its own merits that might work well for model compound studies, none has succeeded in providing as a practical alternative to γ–Al_2O_3 for the hydrotreatment of real petroleum fractions.

Outstanding among these support combinations is the ordered mesoporous silica (OMSs) supports such as MCM-41 and SBA- 15, which have specifically attracted immense attention due to their high surface areas and large volumes of uniform mesopores (pores with diameters between 2 and 50 nm). Nonetheless, the poor hydrothermal stability of MCM-41 type of materials renders it impracticable, especially in the hydroprocessing of real petroleum fractions (Kruk et al., 2000) mostly performed under severe HDS and HDN reactions condition of high temperatures and H_2 partial pressures. In addition to its high thermal and hydrothermal stability (Sun et al., 2005; Brodie-Linder et al., 2008), it is conceivable that the large and ordered pore diameter of SBA-15 would enhance the relatively easier access of reactant molecules into the pores; thus increasing the rate of HDT reactions. Furthermore, SBA-15 with relatively large pore diameters could be envisaged to minimize the effects of catalyst coking by pore mouth blocking, which is profound with γ–Al_2O_3 support during the HDT reactions. With their high surface areas, a great dispersion of supported metals could be achieved so as to increase the amount of catalyst metals converted from the oxide phase to the sulfide phase. These attractive properties of SBA-15 materials make this support a potential to be explored in HDT applications.

2.6.1 Synthesis of SBA-15 materials and pore diameter variation

Mesoporous materials with ordered morphology are considered ideal hosts for nanoparticles due to their large surface area and well-defined pore structure. More importantly, the pore size of ordered mesoporous material can be tuned within the

nanometer range and the pore surface can be functionalized with various metal oxide and organic groups. Mesoporous silica materials such as SBA-15 has been extensively studied among these materials due to their 2-D structure with interconnected pores (Schmidt-Winkel et al., 1999; Blin et al., 2002; Kruk et al., 2007). This type of material was first discovered by Stucky and coworkers (1998) whereby successful synthesis was achieved with a triblock copolymer P123 as the structure-directing agent (SDA) and has since then been labelled as one of the most promising developments in this field of research due to its desirable properties as aforementioned.

2.6.2 Factors affecting pore size variation of SBA-15 materials

In the preparation of mesoporous SBA-15 materials, depending on the end use and subsequent applications, the pore size can be tuned accordingly. This can be achieved during the synthesis by controlling synthesis parameters like synthesis medium (acidic or basic), reaction time and temperature, swelling agents such as organic molecules, surfactants of different chain length, post synthesis treatment, aging of the material during synthesis, calcination conditions, etc.

2.6.2.1 pH of synthesis media (acidic or basic)

One of the ingredients for the synthesis of mesoporous silicate materials is the silica precursor. Typically used silica precursors are the alkoxysilanes with general formula $Si(OR)_4$, where R groups are often methyl or ethyl groups. These alkoxysilanes can undergo hydrolysis either at high (basic) or low (acidic) pH values.

The hydrolysis could be either acid catalyzed to produce protonated silicic acid or base catalyzed to yield anionic silicate (Cao et al., 2009). The protonated silicic acid can then undergo condensation reaction to form polymeric silica network. During this process, protonated silicic acid can interact with anionic, neutral or nonionic surfactants to form highly ordered mesoporous silicates and anionic silicates can interact with cationic surfactant to do same (Suman et al., 2004).

Hydrolysis of the Si–O–Si bridges present in mesoporous silicate materials leads to the pore lattice collapse. Therefore, structural stability is dependent on the level of condensation in walls (related to wall thickness) and to the surface density of silanol groups. This explains why thicker wall materials such as those synthesized using triblock copolymers as surfactants, exemplified by SBA-15, are more stable than MCM-41 type solids (Okamoto et al., 2003).

2.6.2.2 Reaction time and temperature

Kruk *et al.* (2000) studied the thermal stability of SBA-15 structure and its complementary porosity. It was observed that the complementary porosity was retained to a significant extent even after calcination at 900°C, but most likely completely disappeared at 1000°C. The heat treatment was accompanied not only by a significant decrease in the specific surface area and pore volume but also narrowing of the pore size distribution at temperatures up to 900°C. Thus, they were able to demonstrate for the first time that the SBA-15 sample with nitrogen adsorption properties similar to those of MCM-41 can be obtained via calcination at temperatures

as high as 1000 °C. However, the pore volume and specific surface area obtained for the SBA-15 material was relatively low (Suman et al., 2004).

Brodie-Linder *et al.* (2008) investigated the effect of temperature changes within the first 20 minutes of TEOS polymerization during the synthesis of SBA-15. Thermal treatments before and after precipitation during the synthesis of SBA-15 materials were also studied. It was found that thermal treatments in a range of 28–55 °C during the first 10 min of TEOS polymerization had an effect on surface silanol groups and the amount of microporosity in the final SBA-15 materials. Moreover, FTIR analysis of the obtained SBA-15 materials indicated that a change in the distribution of the type of surface silanol groups occurred when the initial reaction temperature was raised to 55 °C.

2.6.2.3 Effect of additives

By using inorganic additives like NH_4F and KCl, Zhang *et al.* (2005) were able to modulate the pore sizes of SBA-15 materials continuously by controlling the micelle properties of block copolymer $EO_{20}PO_{70}EO_{20}$ (P123). It was observed that the addition of F^- dramatically improved the structural periodicity and integrity of the SBA-15 materials and also enlarged the pore sizes at the same time. However, the introduction of KCl into the synthetic system only improved the structural ordering without evident effect on the pore sizes. It was suggested that the changes of micellar properties caused by the salts (KCl, NH_4F) should be responsible for the variation of the pore sizes of the resultant SBA-15 (Zhao et al., 1998).

2.6.2.4 Effect of swelling agents

The addition of swelling agents such as trimethyl benzene (TMB) and alkanes have proven to be the most effective way in expanding the pore size of MCM-41 silicas (2–10 nm) (Dhar et al., 2004). By using TMB as micelle expander, the pore size of SBA-15 has been tuned in the range of 5–30 nm (Zhao et al., 1998). However, subsequent studies showed that a phase transition from highly ordered SBA-15 (7–12 nm) to mesoporous cellular foams (MCF) with large nodded pore structures (~ 22 – 42 nm) occurred with increasing amounts of TMB (Vradman et al., 2003).

In the search for effective swelling agents for the synthesis of large pore diameter and highly ordered SBA-15 materials, alkanes of different chain lengths have also been investigated (Sun et al, 2005). However, improved pore size of the highly ordered SBA-15 was obtained as the chain length decreased. Furthermore, when alkanes with longer chain length (such as nonane, octane, etc.) were employed, disordered MCF silicas were produced under the temporal reaction conditions. It was observed that the shorter the alkane chain length, the more of it could be accommodated in the micelles cores, and resulted in larger micelles dimensions; thus increased pore diameter. They concluded that the higher solubilization capacity of shorter length alkanes (such as hexane) determines the ultimate pore diameter of SBA-15 silicas.

Following the work of Sun *et al.* (2005), larger pore SBA-15 silicas have been prepared by Kruk *et al.* (2007) using hexane as micelle expander and initial synthesis temperature of 15°C. Small-angle X-ray scattering data showed that the highly

ordered 2-D hexagonal SBA-15 structure formed at 15°C, and was preserved even after 5 days of hydrothermal treatment at 130°C. This was evidenced in the characteristic peaks identified at (100), (110), (200) and (210) which is a reflection of mesoporous 2-D hexagonal structure of the synthesized SBA-15 material. Up to date, the largest pore diameter SBA-15 so far produced has been that reported by Cao *et al.* (2009) by employing 1, 3, 5-triisopropyl benzene (TIPB) as the micelle expander and varying the initial synthesis temperature to a low as 11.4°C.

2.6.2.5 Effect of initial synthesis temperature

The initial reaction temperature is very critical in the synthesis of highly ordered SBA-15, especially in the presence of swelling agents such as the alkanes. Report shows that those SBA-15 materials prepared with short chain alkanes such as nonane or octane were always disordered large-pore mesoporous cellular foams (MCF) under the temporal synthesis conditions (Suman et al., 2004). Zhang *et al.* (2005) successfully prepared highly ordered SBA-15 with large cylindrical mesopores using short chain alkanes by controlling the initial reaction temperature. For each alkane, there existed a temperature where a phase transition from highly ordered mesoporous structure to disordered one (e.g. MCF) occurred. For example, in the case of hexane, the reaction temperature should be strictly lower than 17ºC; otherwise, other structures (such as, MCF materials) would form (Sun et al., 2005). In the case of heptane and nonane, the initial temperature should be lower than 22ºC and 27ºC, respectively. They also observed that apart from the alkane's chain length chosen, in order to obtain highly ordered SBA-15 silicas; the shorter the chain length of alkanes,

the lower the reaction temperature should be chosen. However, when the initial reaction temperature is lower than 283 K, only amorphous silica gels are obtained for all alkanes. Therefore, the preparation of highly ordered materials should be carried out in a specific temperature range for each alkane. Within this range, a higher temperature on the initial reaction stage will lead to a slight shift of the (100) diffraction peaks to lower angles, indicating a slight increase of the pore size of the obtained SBA-15.

2.6.3 Effect of pore diameter of support on hydrotreating

The effect of pore diameter of catalyst support on catalytic HDT is of great importance since the alteration of catalytic activities due to change in support may arise as a result of important factors like porosity, dispersion of active metals on the support and morphology of active component (Breysse et al., 2003).

For instance, the diffusion limitation associated with the traditional γ–Al_2O_3 support while in operation with heavy petroleum fractions becomes a major drawback to its full utility in the hydroprocessing operations due to pore blockage by coke deposition. For an enhanced HDT activity, the pore size distribution of the support should concentrate around a particular diameter; and the pore diameter should be large enough to overcome most diffusional restrictions (Gary et al., 2004). However, too large a pore diameter also leads to further decrease in surface area, which might result in decreased HDT activity. Supports that provide larger pore diameters while maintaining desirably high surface areas for great dispersion of supported metals will help minimize the major diffusional problem of γ–Al_2O_3 support.

2.6.4 Effect of promoters on hydrotreating

The HDT catalyst is mostly composed of active metal components showing favorable activities for HDS and HDN, dispersed on inorganic oxide supports with high surface area and porosity. Promoters are typically added in relatively small amounts in the catalyst preparation so as to impart better catalytic activity, selectivity, and stability (Satterfield, 1991). Commonly used active metal is molybdenum (Mo), which is mostly promoted by cobalt (Co) or nickel (Ni). Tungsten also shows a good activity for hydrogenation, and it is relatively cheaper than Mo (~ 20 US$/kg cheaper) (Eijsbout et al., 2007). Iron is generally considered an inferior promoter in comparison to Co and Ni (Hubaut et al., 2003); however, it can be a desirable option due to its relatively low cost (Gary, 1994).

2.6.5 Application of siliceous SBA-15 as HDT catalyst support

The evaluation of purely siliceous mesoporous SBA-15 as a potential HDT catalyst support in the preparation of Mo, CoMo, and NiMo catalysts was demonstrated by Vradman *et al*. (2003). It is known that the active component of the HDT catalyst responsible for the removal of sulfur is the MoS_2 phase; with its edge sites being more active for sulfur removal (Sundaramurthy et al., 2008). They correlated the catalytic activities with the quantity of oxygen chemisorbed on the vacancies of the above mentioned sulfided catalysts. The good correlation found between the catalytic activities and oxygen chemisorption was attributed to the formation of a patchy monolayer as a result of oxygen chemisorption at the anionic vacant sites of the MoS_2 catalysts. An activity comparison with γ-Al_2O_3-supported

catalysts clearly indicated the SBA-15-supported catalysts as superior to its γ-Al_2O_3 counterpart prepared in similar manner.

In the hydrodesulfurization of dibenzothiophene and the hydrogenation of toluene using pure SBA-15 supported NiW-S catalyst, Vradman *et al*. (2003) reported an increased catalytic activity of the order of 1.4 and 7.3 times higher, respectively, than that of the sulfided commercial $CoMo/Al_2O_3$. Their findings evidenced the excellent potential of high loading sulfided NiW/SBA-15 catalysts for deep hydrotreatment of real petroleum feedstocks. Furthermore, the aforementioned limited number of studies in which pure SBA-15 was applied as a catalyst support for HDT reactions employed model compounds as the feedstocks (Vradman et al., 2003; Dhar et al., 2005). However, a study conducted by Sundaramuthy et al. (2008) tested the catalytic functionality of AlSBA-15-supported NiMo catalyst by screening with a light gas oil (derived from Athabasca bitumen) petroleum fraction. This catalyst with 17 wt.% Mo and 3.4 wt.% of Ni was found to produce the best HDN and HDS activities, which was comparable to the conventional γ-Al_2O_3-supported NiMo catalyst at industrial conditions.

Generally, for heterogeneous catalytic reactions such as HDT in which porous catalysts are employed, to enhance the rates and conversions of such reactions, the internal surfaces of the catalyst pellet hosting the active sites must be readily accessible to reactant molecules. In other words, the catalyst pore structure should be such that it would facilitate the diffusion of reactant molecules to the internal surfaces. This diffusion phenomenon would be greatly hindered depending on the reactant

molecular size as well as the pore size of the catalyst. Notable among the aforementioned studies (Vradman et al., 2003; Dhar et al., 2005; Sundaramuthy et al., 2008) using SBA-15 catalyst support is the fact that the pore diameters of the supports used was in the range of 5-8 nm. Nonetheless, in the HDT of heavy petroleum fractions, it is generally more practicable to use catalysts with larger pore diameters so as to enhance efficient species diffusion and also to minimize the possibilities of pore-plugging via coke deposition. The delineated problems could be greatly improved by synthesizing larger pore diameters SBA-15 supports using hexane as micelle expanders. The effectiveness of different pore diameter SBA-15 catalyst supports would be further explored in the hydrotreating of bitumen-derived heavy gas oil from Athabasca.

3.0 EXPERIMENTAL METHOD

This section highlights the experimental procedures performed in the course of the project and have been categorized into five subsections: 1) Syntheses of SBA-15 supports and FeW/SBA-15 catalysts of different pore diameters; 2) Supports and FeW/SBA-15 catalysts characterizations; 3) Catalytic performance evaluation using heavy gas oil derived from Athabasca bitumen; 4) Metals optimization studies on the optimum catalyst support, characterizations and subsequent catalytic performance evaluation; and 5) Kinetics and long-term deactivation studies for the optimum catalyst produced. Also addressed in this section are the detailed experimental procedures carried out in the project as well as the underlying principles considered in the various factions of the research. Finally, the section is designed to enhance understanding of the entire project by providing basic descriptions of all the laboratory work that contributed to the conclusions reached in this thesis.

3.1 Syntheses of SBA-15 supports and FeW/SBA-15 catalysts of different pore diameters

3.1.1 SBA-15 supports syntheses

The siliceous SBA-15 materials were synthesized using hexanes as a micelle expander under acidic conditions, according to the procedure described elsewhere (Sundaramuthy et al., 2008; Kruk et al., 2007). Shown in Figure 3.1 provides schematic of the experimental set-up employed for the supports syntheses.

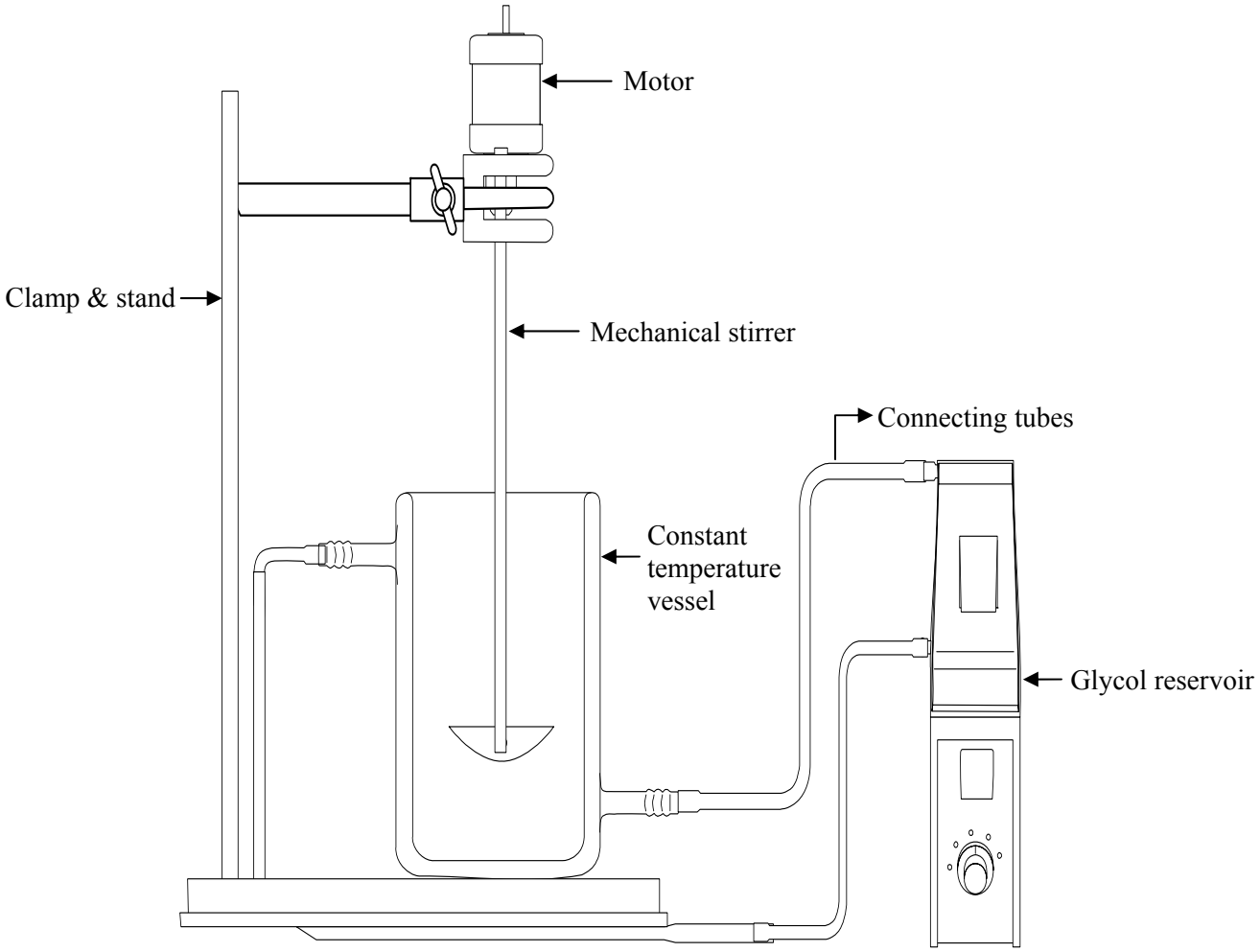

Figure 3.1: Experimental set-up for mesoporous SBA-15 supports synthesis

The set-up consisted of a constant temperature vessel (CTV) equipped with ethylene glycol cooling system to control drastic temperature fluctuations. The accuracy of this CTV cooling system can be as high as ± 0.1°C. Due to its high degree of accuracy, its content was easily maintained at the desired temperature of 15°C for all experimental runs performed. Circulation of the glycol was facilitated by a circulatory pump and a tubing system which connected the CTV to the bulk glycol reservoir. The stirring rate of the disc-shaped mechanical stirrer was controlled by a digital motor assembly supported by means of a clamp and stand apparatus. The motor and circulatory pumping device was powered by a DC (direct current) source for the duration of each experimental run.

In the synthesis of the SBA-15 supports, an important ingredients used is the triblock copolymer (Pluronic P123), which served as the structure-directing agent (SDA). It was supplied by Sigma Aldrich and has a nominal chemical formula of $HO(CH_2CH_2O)_{20}(CH_2CH(CH_3)O)_{70}(CH_2CH_2O)_{20}H$, which corresponds to an average molecular weight of 5800. Such triblock copolymers are based on the poly(ethylene glycol)-poly(propylene glycol)-poly(ethylene glycol) configuration and are known generically as poloxamers. Poloxamers are nonionic triblock copolymers composed of a central hydrophobic chain of polyoxypropylene (poly(propylene oxide)) flanked by two hydrophilic chains of polyoxyethylene (poly(ethylene oxide)). Poloxamers have behaviors similar as those of hydrocarbon surfactants and posses the property of forming micelles (dispersed aggregates of surfactant molecules) when placed in selective solvents such as water (www.wikipedia.org, 2011). They are capable of

forming both spherical and cylindrical micelles. When dissolved in aqueous acidic medium, P123 forms micelles that are used as the backbone (template) to make structured mesoporous materials such as SBA-15. Another ingredient used in the synthesis medium is the silica source, mostly tetraethyl orthosilicate (TEOS). The chemical formula for TEOS is given by: $Si(OC_2H_5)_4$ or $Si(OR)_4$, where the alkyl group R = C_2H_5. These alkoxides are ideal chemical precursors for sol-gel synthesis because they react readily with water in a reaction known as hydrolysis to yield a hydroxyl-substituted silicon atom as depicted in Equation 3.1:

$$Si(OR)_4 + H_2O \rightarrow HO - Si(OR)_3 + R - OH \qquad \textbf{3.1}$$

Intermediate species such as $[(OR)_2–Si-(OH)_2]$ or $[(OR)_3–Si-(OH)]$ that may result from partial hydrolysis can link together in a condensation reaction to form a siloxane [Si–O–Si] bond as shown in equation 3.2 (a &b):

$$(OR)_3 - Si - OH + HO - Si - (OR)_3 \rightarrow [(OR)_3 - Si - O - Si(OR)_3 + H - OH \qquad \textbf{3.2a}$$

or

$$(OR)_3 - Si - OR + HO - Si - (OR)_3 \rightarrow [(OR)_3 - Si - O - Si(OR)_3 + R - OH \qquad \textbf{3.2b}$$

The condensation reaction liberates small molecules such as water or alcohol and can continue to build larger and larger silicon-containing molecules by the process of polymerization. Thus, polymerization is associated with the formation of a 1, 2, or 3-

dimensional network of siloxane [Si–O–Si] bonds accompanied by the production of H-O-H and R-O-H species as shown in Figure 3.2 (www.wikipedia.org, 2011):

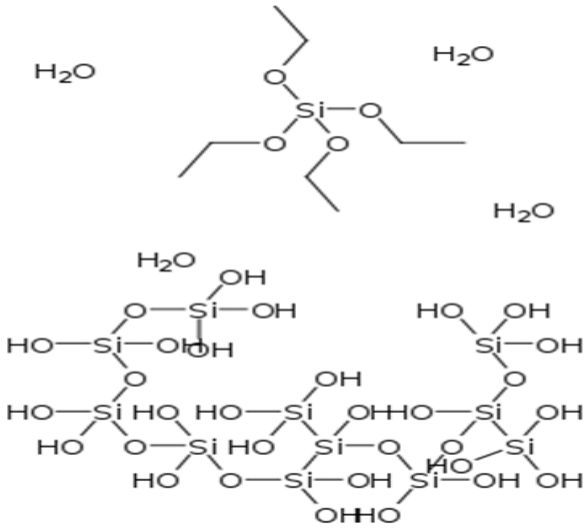

Figure 3.2: TEOS and water polymerization in sol-gel reaction

In the case of SBA-15 synthesis, the nominal molar gel composition used was 1.0 TEOS:0.0168 P123:4.02 C_6H_{14}:0.0295 NH_4F:4.42 HCl:186 H_2O. SBA-15 materials with different pore diameters were synthesized by varying the molar ratio of C_6H_{14} and NH_4F in the range of 60 to 180. Alkanes have the flexibility of expanding micelle cores probably due to its hydrophobic nature.

In a typical synthesis procedure, 9.8 g P123 and 0.109 g NH_4F were dissolved in 335 mL of 1.3 M aqueous HCl solution at room temperature. This solution was transferred to a constant temperature vessel (CTV) maintained at 15°C. Ammonium fluoride was used in this medium to serve as a structural ordering agent. After 1 h of mechanical stirring, a mixture of 20.8 g TEOS and 34.6 g C_6H_{14} was added. The

reaction was allowed to proceed under mechanical agitation for 24 h in the CTV, after which the gel formed was isolated and subjected to hydrothermal treatment in a teflon-lined autoclave for 3 days. The solid product was filtered, washed with deionized water, and dried for 24 h at room temperature. Removal of organic template from the samples was achieved by calcination at 550°C for 5 h using a heating rate of 2°C/min.

3.1.2 Synthesis of FeW/SBA-15 catalysts

FeW catalysts supported on SBA-15 with different pore diameters were prepared by the aqueous impregnation technique. The incipient wetness co-impregnation technique was employed to load Fe and W metal precursors onto the pristine supports. Aqueous solutions of ammonium metatungstate (AMT), $(NH_4)_6H_2W_{12}O_{40}$ (Fluka) and iron nitrate, Fe $(NO_3)_3.9H_2O$ (Aldrich) were used as W and Fe sources, respectively. After each impregnation, the catalysts were dried at 100°C for 24 h. In a typical synthesis, 0.514 g AMT was dissolved in 15 mL de-ionized water until a homogenous solution was formed. 2.55 g siliceous SBA-15 was added to this solution, to get 15 wt. % W/SBA-15. This mixture was dried in an oven at 100°C. For the FeW/SBA-15 catalysts preparation, similar approach was used only that 0.514 g AMT and 2 wt. % Fe were dissolved and subsequently loaded on the various supports. The four catalysts prepared in phase 1 of the project are designated as Cat A, Cat-B, Cat-C and Cat-D; with pore diameters 5.7 nm, 10.1 nm, 15 nm and 18.5 nm, respectively.

Similarly, Cats-E, F, G, H, and I were also prepared to be screened in phases II and III of the project. These catalysts were prepared with the same support (i.e. having the same textural properties). However, different metal loadings were employed so as to study the effects of Fe and W loadings in the ranges of 1-5 wt. % Fe and 15-45wt. % W, respectively.

3.2 Supports and FeW/SBA-15 catalysts and characterizations

Several characterization techniques were applied to the synthesized SBA-15 supports and corresponding FeW catalysts. Relevant techniques were selected to help ascertain the structure, morphology, textural properties, as well as to give insight about the catalytic behavior of materials produced.

X-ray powder diffraction analysis is a powerful method by which X-rays of a known wavelength are passed through a sample to be identified in order to identify the crystal structure. The wave nature of the X-rays makes them easy to be diffracted by the lattice of the crystal to give characteristic diffraction peaks at differing angles and intensities (Niemantsverdriet, 2000). The diffracted beams from atoms in successive planes cancel unless they are in phase, and the condition for this is given by the Bragg relationship:

$$n\lambda = 2d \sin\theta \qquad \textbf{3.3}$$

where λ = wavelength of the X-rays; d = distance between different plane of atoms in the crystal lattice; and θ = angle of diffraction.

Nitrogen physisorption isotherms were measured on a Micromeritics ASAP 2000 analyzer at liquid nitrogen temperature of 77 K. This analysis is based on the theory established by Brunauer, Emmett, and Teller (BET) for predicting the surface characteristics of a substance based on the size of the adsorption monolayer of an adsorbate (Gregg et al., 1967). Typically, it is nitrogen adsorption that is analyzed under liquid nitrogen conditions. Based on the amount of N_2 that is physically adsorbed by the SBA-15 materials, and also on theoretical equations, the specific surface area (m^2/g), average pore diameter (nm), and pore volume (cm^3/g) of the cylindrical arrays of pores can be estimated.

Transmission electron microscopy (TEM) provides a means by which the inner pore diameter, as well as the structural morphology of the SBA-15 materials can be determined. In this method, electrons are transmitted through an ultra-thin sample and interact with the sample as they pass through. As they pass out the other side, they produce an image possessing a degree of transparency, allowing the inner pore diameter and the hexagonal structure of the SBA-15 material to be determined.

Scanning electron microscopy (SEM) micrographs were observed on a Hitachi S3400 microscope. High quality images on a nanometer scale can be obtained using SEM analysis. These images are created by focusing a high-energy beam of electrons onto the sample and detecting interactions that occur at the sample surface. These images help to determine the morphology of SBA-15 materials produced.

Also used for local compositional analysis was an energy-dispersive X-ray (EDX) analysis, which is an integrated feature of the scanning electron microscope

operating at 25 kV. During EDX analysis, the specimen under scrutiny was bombarded with an electron beam inside the scanning electron microscope. The bombarding electrons collide with electrons generated by atoms of the specimen, knocking some of them off in the process. The vacancy created by an ejected inner shell electron is eventually occupied by a higher-energy electron from an outer shell. The transfer and subsequent occupancy of outer electron (of higher energy) to lower energy level (inner core) result in energy loses by the emission of X-ray photons. The amount of energy released is dependent on which shell electron is transferred from, as well as the shell it is transferring to (Niemantsvardriet, 2000). Furthermore, the atom of every element releases X-rays with unique amounts of energy during the transferring process. Thus, by measuring the amounts of energy present in the X-rays being released by a specimen during electron beam bombardment, the identity of the atom from which the X-ray was emitted can be established. The chemical composition determination is typically based on the average analytical data of individual particles.

Another spectrometric technique that was applied to the impregnated SBA-15 supports is the inductively coupled plasma mass spectrometry (ICP-MS). The main principle governing this method of analysis is by applying ICP to produce ions from the sample and MS to separate and detect the ions. Since there is always a difference between the targeted and actual amount of metal contents impregnated, the ICP-MS technique provides the necessary tools to determine the exact metal content of each

catalyst sample. Thus, this technique was utilized to quantify the metal composition in the catalysts.

Diffuse reflectance infrared Fourier transform spectroscopy (DRIFTS) was used to collect spectra based on measuring the coherence of the infrared region of a radiative source. With regard to this project, this spectroscopic technique was to analyze the typical sulfide phases formed on the surface of the FeW/SBA-15 catalysts as a result of time-on-stream.

Another technique employed to analyze the behavior of the FeW/SBA-15 catalysts is the chemisorption of carbon monoxide. By monitoring the amount of CO adsorbed by the sulfided catalyst samples, one can obtain the extent to which metal catalyst particles are distributed on the SBA-15 surface, and therefore the number of exposed active sites on the catalyst surface. In this method, the carbon monoxide uptake on sulfided catalysts was measured using the Micromeritics ASAP 2000 instrument.

Finally, the thermal degradation of the FeW/SBA-15 catalyst samples was studied using the Thermogravimetric analysis (TGA). This technique uses controlled heating of the catalyst sample in the presence of air flow to monitor reactions and physical changes in materials. TGA provides quantitative measurement of mass change in materials associated with transition and thermal degradation. It records change in mass from dehydration, decomposition, and oxidation of a sample with time and temperature.

3.2.1 Small-angle X-ray Scattering Analysis

The calcined SBA-15 samples were characterized by small angle X-ray scattering (SAXS) to ascertain their crystal structures. Diffraction patterns were recorded with a Bruker Smart 6000 CCD detector on a 3-circle D8 goniometer using a Rigaku RU 200 Cu rotating anode generator fitted with parallel focusing cross-coupled mirrors and a 0.5 mm pinhole collimator. Data was obtained using a still data collection (Bruker Software: SMART) with an exposure time of 300 seconds in the 0 to 10.0° range. Broad angle XRD patterns of all the SBA-15 supported FeW catalysts were recorded on a Rigaku diffractometer using Cu Kα radiation.

3.2.2 N_2 adsorption-desorption isotherms measurement

The Brunauer-Emmett-Teller (BET) surface area, pore volume, and pore diameter of the SBA-15 supports and catalysts were determined by analyzing the adsorption and desorption of N_2 at 77K using a Micromeritics 2000 ASAP analyzer. Prior to the analysis, 0.2g of the catalyst was out-gassed in vacuum at 200°C until the static pressure remained less than 6.6×10^{-4} Pa. The BET method was used to calculate the surface area in the range of relative pressures between 0.05 and 0.30. The value of 0.1620 nm^2 was taken for the cross-section of the physically adsorbed N_2 molecule. The pore diameter and pore size distributions were calculated from the adsorption and desorption branches of the isotherms using the Barrett–Joyner–Halenda (BJH) method. The mesopore volume was determined from the N_2 adsorbed at a $P/P_0 = 0.4$. The total pore volume was calculated from the amount of nitrogen adsorbed at P/P_0 =

0.95, assuming that adsorption on the external surface was negligible compared with adsorption in pores. In all cases, correlation coefficients above 0.999 were obtained.

3.2.3 Transmission electron microscopy (TEM) analyses

The morphological features of the support and catalysts were studied from transmission electron micrographs obtained with a Tecnai F20 at 200 kV. In this technique, the powder samples were grounded softly in an agate mortar and dispersed in heptane in an ultrasonic bath for several minutes. A few drops were then deposited on 200 mesh copper grids covered with a holey carbon film. The electron micrographs were recorded in electron negative films and in a digital PC system attached to the electron microscope.

3.2.4 SEM and EDX analyses

Scanning electron microscopy, located at the University of New Brunswick, Canada, was used to analyze the pore structure as well as the quality of SBA-15 materials. The sample images were created and collected using a Hitachi S3400 SEM. Both substances were examined by mounting the samples onto aluminum slabs using carbon paint. A gold coating was then applied by vacuum sputtering to improve secondary electron signals and reduce charging.

3.2.5 Inductively Coupled Plasma Mass Spectroscopy

The elemental compositions of both the fresh FeW/SBA-15 catalysts were analyzed with a Perkin Elmer ELAN 5000 ICP-MS instrument. This analysis method

works by applying inductively coupled plasma (ICP) to produce ions from the sample and mass spectroscopy (MS) to separate and detect the ions.

3.2.6 DRIFT Spectroscopy

Diffuse Reflectance Infrared Fourier spectroscopy (DRIFTS) of CO adsorption experiments were performed using a Perkin Elmer Spectrum GX instrument equipped with DTGS detector and a KBr beam splitter was used for this analysis. Approximately 10 mg of powdered catalyst sample was loaded in to a sample cup inside a Spectrotech diffuse reflectance in situ cell equipped with ZnSe windows and a thermocouple mount that allowed direct measurement of the sample surface temperature. Spectra for each experiment were averaged over 64 scans in the region 4000–1000 cm^{-1} with a nominal 4 cm^{-1} resolution. Prior to the CO adsorption, the catalyst was in situ sulfided in the Spectrotech diffuse reflectance cell using 10% (v/v) H_2S/H_2 (50 cm^3/min) at 400 °C for 2 h. At this temperature, the flow was switched to He at a flow rate of 50 cm^3/min and the temperature decreased to 30°C. The background spectrum was then recorded. The adsorption process was carried out at 30°C by introducing CO (30 cm^3/min) into the system for 30 min. After adsorption, the system was subsequently purged with He at a flow rate of 50 cm^3/min for 30 min. Spectra were then recorded under He flow. The background spectrum was subtracted from the post adsorption spectra.

3.2.7 CO Chemisorption

The amount of carbon monoxide chemisorbed on the FeW/SBA-15 catalysts was determined with the Micromeritics ASAP 2000 instrument. Prior to the CO chemisorption measurement, 0.2 g of sample was first degassed at 200 °C for 2 h, following an evacuation until the static pressure remained less than 6.6 x 10^{-4} Pa. In situ sulfidation of sample was then carried out using 10 mol. % H_2S in H_2 at 400°C for 4 h. The chemisorption was performed by passing pulses of CO over the sample to measure the total gas uptake at 35°C.

3.2.8 Thermogravimetry analysis

To determine the thermal stability of the freshly synthesized SBA-15-supported FeW catalysts, the thermogravimetric (TGA) analysis was performed using 5 mg samples of each SBA-15 grade produced. Using a Perkin-Elmer (Pyris Diamond) TGA instrument, data was collected at 0.5s intervals as the sample was heated to 600ºC at a rate of 10ºC/min under air flow at 100 mL/min.

3.3 Catalytic performance tests of FeW/SBA-15 catalysts

As aforementioned in section 3.1.2, the dried and calcined powdered form of the synthesized FeW/SBA-15 catalysts prepared by the incipient wetness co-impregnation method was subjected to high pressure in a die-press to convert it into their pellet form in order to make it useable in the micro trickle bed reactor for the hydrotreating applications. This was achieved via dry-pelletizing of the powdered FeW/SBA-15 material in the absence of binder (so as to eliminate influence from the

binders) by applying about 32 MPa of pressure in a pelletizer unit (Fred S. Carver Inc., USA). The produced catalyst pellets had typical size range from 14 to 10 mesh (1.0 to 1.5 mm).

Hydrotreating of the petroleum feedstock (bitumen-derived heavy gas oil from Athabasca) using the pelletized FeW/SBA-15 catalysts in a packed micro-trickle bed reactor, operated in the downward mode. A typical range of carbon molecules present in the feedstock varies from C_5 to C_{60} with a boiling point ranging from 200 to 600 °C and a specific gravity of 0.99 at 20 °C. Figure 3.3 illustrates the schematic representation of the experimental set-up used to evaluate the hydrotreating performance of the FeW/SBA-15 catalysts produced.

The reaction set-up is comprised of liquid and gas feeding sections, a high-pressure reactor (comprising a catalyst bed intermixed with packings of different size silicon carbide particles to mimic a plug flow reactor), a heater with controller for precisely monitoring the temperature of the catalyst bed, a water scrubber for absorbing ammonium sulfide from the reaction product, and a high-pressure gas-liquid separator, and a back pressure regulator for controlling the system pressure. The preliminary catalyst screening experiments (phase I) were conducted at the temperature, pressure, and liquid hourly space velocity (LHSV) of 375 – 400 °C, 8.8 MPa, and 1 h^{-1}, respectively. It should be noted that these conditions were kept constant so as to effectively study the effect of different FeW/SBA-15 catalyst pore

sizes on both sulfur and nitrogen conversions. Similarly, hydrogen-to-oil ratio was operated at 600 mL/mL while maintaining catalyst volume at 5 mL.

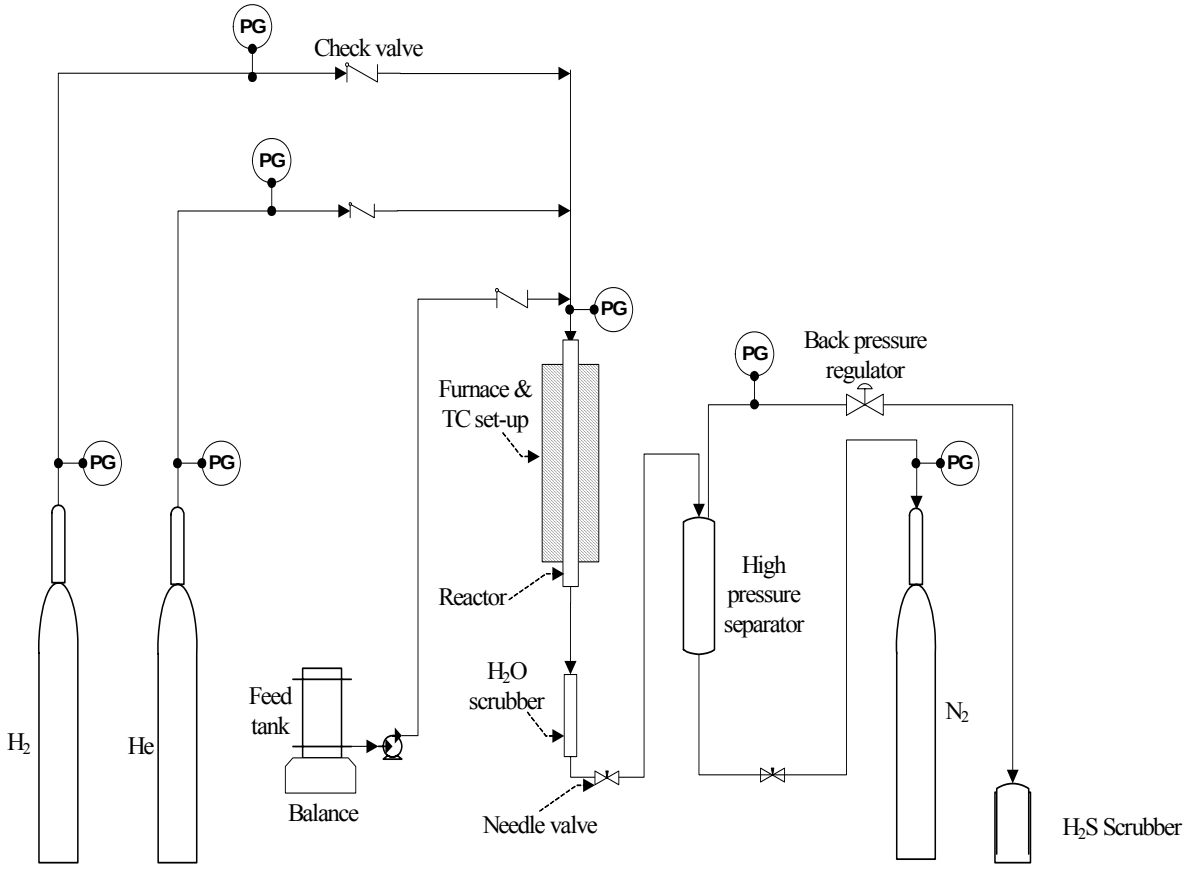

Figure 3.3: Schematic representation of experimental set-up for the hydrotreatment of heavy gas oil

The catalyst pellets (1.5 g ≈ 5mL) were first loaded into the reactor bed in a dilute mixture of 90 mesh silicon carbide. The layers above and below the catalyst bed were made up of 3 mm diameters quartz beads, 16, 46, and 60 mesh silicon carbide particles, respectively. Figure 3.4, illustrates the temperature program followed for a typical hydrotreating run.

Prior to the start of run, activation of the catalyst was carried out in a sulfidation procedure. This in situ sulfidation procedure was intended to transform the inactive oxidic FeW/SBA-15 catalyst to its most active sulfide form. To achieve this, a sulfidation solution, constituting 2.8 vol.% butanethiol in an insulating oil solvent was pumped over the catalyst bed at a rate of 5 mL/h. At the same time, hydrogen gas was also introduced to the reactor system at a volumetric ratio of 600 mL/mL with the dilute sulfiding solution.

The reactor was run under the conditions of 8.8 MPa pressure and 193 °C temperature for 24 hours. After this time, the temperature was increased to 343 °C in steps of 20 °C every 10 minutes until the desired sulfidation temperature was attained and maintained for another 24 hours. After sulfidation, the HGO was fed into the reactor by means of a pump, operated at a rate of 5 mL/h to give a liquid hourly space velocity (LHSV) of 1 h^{-1}. The reactor pressure and the volumetric ratio of hydrogen gas to feed liquid are kept at the same settings from the sulfidation procedure. At a reactor temperature of 375 °C, the catalyst was subjected to precoking for five days. This precoking step was intended to allow the reactor setup to reach steady-state behavior as coke is deposited on the catalyst surface.

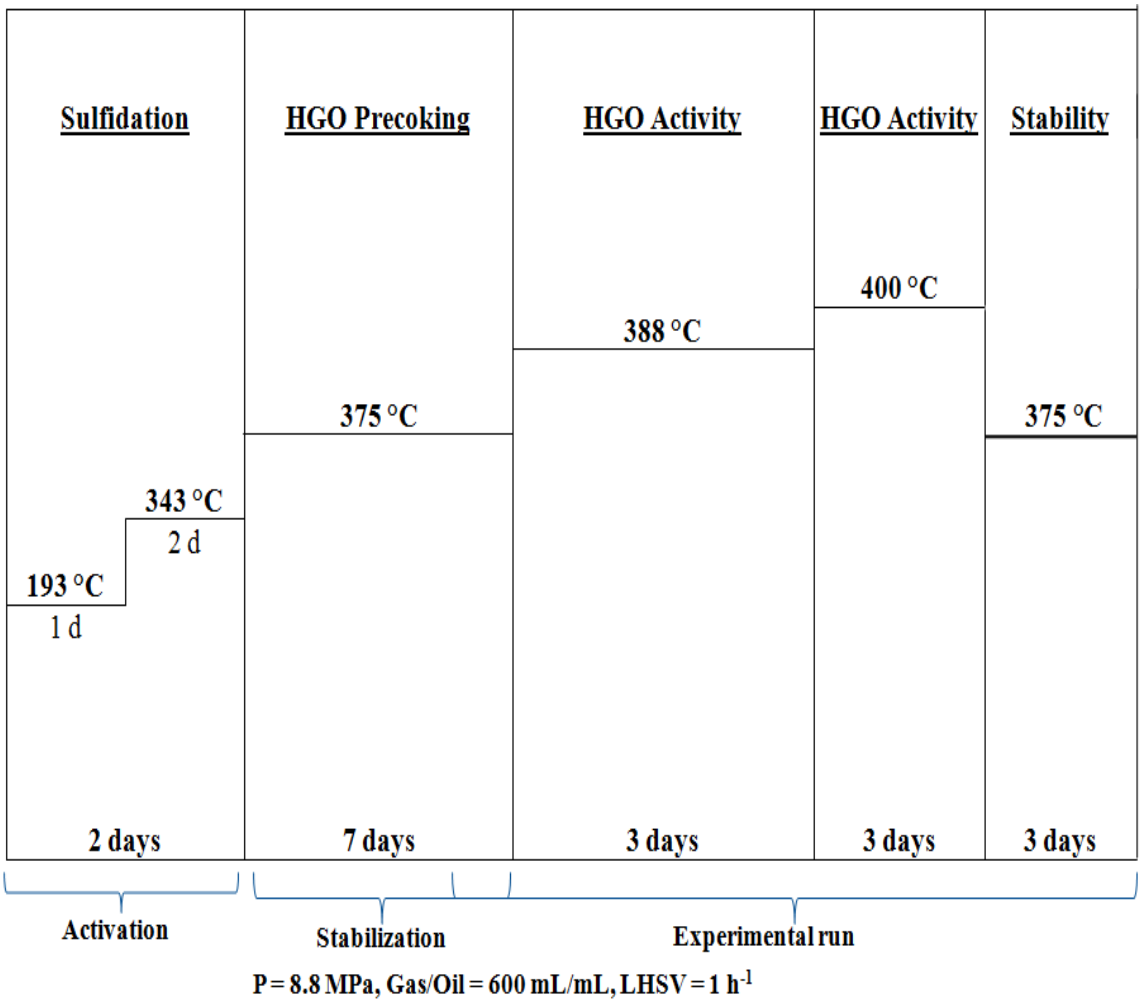

Figure 3.4: A typical temperature program followed for the hydrotreatment of heavy gas oil

After this period, the hydrotreating process was carried out for three days for each of the three chosen reaction temperatures (375, 388 and 400 °C) of study. During the precoking phase, product samples were taken every 24 hours and stripped for 2 hours under continuous N_2 flow to remove any dissolved NH_3 and H_2S within the liquid. The stripped hydrotreated product samples were then analyzed for sulfur and

nitrogen contents. In order to make calculation of sulfur and nitrogen conversions possible, the HGO feedstock was also analyzed for sulfur and nitrogen contents.

3.3.1 Nitrogen and sulfur analyses

The ASTM 5463 standard procedure was followed in the determination of sulfur concentrations of feed and hydrotreated liquid products using the combustion/fluorescence technique. In a similar manner, the total nitrogen contents of the feed and liquid products were determined by the combustion/chemiluminence technique of the ASTM D4629 method. An Antek nitrogen/sulfur analyzer (Antek 9000, model: 9000NS) was used for the total sulfur and nitrogen analyses. The instrumental error for both N and S analysis was found to be approximately ± 3%, based on analyzing standard solutions of known composition. The basic chemistry governing its operation is summarized in equations 3.4, 3.5, & 3.6 (Antek, 1998).

At the start of this analysis, the liquid sample is subjected to a high combustion temperature (i.e. in excess of 1000ºC) for oxidation to occur. As a result of this reaction, sulfur and nitrogen present in the sample are converted into their oxide forms (primarily, sulfur dioxide and nitric oxides, respectively):

$$R-N+R-S+O_2 \rightarrow CO_2+H_2O+NO^{\bullet}+SO_2 \qquad \textbf{3.4}$$

Excitation of the sulfur dioxide compounds proceed as they come into contact with ultraviolet radiation of a specific wavelength in the combustion chamber of the set-up. De-excitation of electrons to their original energy levels is accompanied by the emission of light (fluorescent emission, i.e. absorbed originally from a light source) of

specific wavelength, which is then detected by a photomultiplier integrated with the set-up. Equation 3.2 is a representation of the reaction occurring in this process:

$$SO_2 + hv \rightarrow SO_2 + hv' \qquad \textbf{3.5}$$

On the other hand, an on-board ozone generator produces ozone, which when contacted with nitric oxide compounds present in the liquid sample results in the formation of meta-stable nitrogen dioxide species. Relaxation of the meta-stable nitrogen dioxide species is associated with the emission of a photon of light (chemiluminescent emission, i.e. from a chemical reaction), which is then detected by a photomultiplier integrated with the set-up. A typical reaction that proceeds is as shown in equation 3.3:

$$NO^{\bullet} + O_3 \rightarrow NO_2^{*} + O_2 \rightarrow NO_2 + hv \qquad \textbf{3.6}$$

The species (sulfur and nitrogen) conversions are calculated as follows:

$$\boxed{\%Conversion = \frac{C_{i,Feed} - C_{i,\mathrm{Pr}\,oduct}}{C_{i,Feed}} \times 100\%} \qquad \textbf{3.7}$$

where: $C_{i,Feed}$ and $C_{i,Product}$ = sulfur or nitrogen concentrations in feed and hydrotreated liquid products, respectively.

3.3.2 Simulated distillation

Simulated distillation is a GC method used to characterize petroleum fractions and products, since it permits the quick determination of their boiling range distribution. Samples are analyzed on a non polar chromatographic column that separates the hydrocarbons in order of their boiling points. These are correlated with the retention times, through a calibration curve obtained by running under the same conditions a known standard mixture of hydrocarbons, usually n-alkanes, covering the boiling range expected in the sample. Results are reported as a correlation between the boiling points and the percentages of the sample eluted from the column (Facchetti et al., 2005).

This technique was used to determine the boiling range distribution of the liquid heavy gas oil feedstock and products, respectively. The separation of components in the column is based on their boiling range and can be performed using ASTM D6352 method. A Varian model CP3800 gas chromatograph integrated with a Varian CP 8400 auto sampler was used in this work. The hydrocarbons in the sample (s) were separated based on their boiling range by a capillary column 10 m (length) x 0.53 mm (diameter) x 0.88 mm (nominal film thickness). A flame ionization detector (FID) was used to detect the components' boiling ranges using He as a carrier gas at a flow rate of 30 mL/min. The air flow and H_2 were maintained at 400 mL/min and 35, respectively. The detector temperature and oven final temperature were maintained at 375 and 380ºC, respectively. The boiling fractions are identified by comparing them against calibration curve.

3.3.3 SBA-15 pore diameter optimization

To determine the optimum SBA-15 catalyst pore diameter required for effective hydrotreatment of the feedstock in question, phase I of the project saw the preparation of four types of FeW/SBA-15 catalysts with variable pore diameters. The pore diameter variation was made possible by varying the molar ratio of swelling agent (hexane)-to-ammonium fluoride used in the synthesis medium. The variation of this molar ratio in the range of 60 and 180 resulted in the production of SBA-15 catalyst supports of diameters in the 5 to 20 nm range. Thus, four catalysts designated a Cat-A, Cat-B, Cat-C, and Cat-D; with pore diameters 5.7, 10.1, 15.7, and 18.5 nm, respectively, were produced. Sections 3.1 and 3.3 address catalysts preparation and their subsequent screening conditions, respectively.

3.3.4 Optimization of metals loading for HGO hydrotreating

In order to obtain the ideal Fe and W metals loading for the preparation of the optimum SBA-15 catalyst support, a sequential metal loading approach was adopted. In this approach, the optimum W loading was first found by varying it in the range of 15 to 45 wt.%, while maintaining the Fe loading at an initial constant loading of 2 wt.%. Once the W metal loading was optimized, the optimum promoter (Fe) loading would then be found in conjunction with the obtained optimum W loading. Specific loading combinations tested at constant Fe loading of 2 wt.% and W loadings of 20.0, 30.0, and 45.0, respectively, resulted in catalysts designated as Cat-E, Cat-F, and Cat-G, respectively. The obtained optimum W loading of 30 wt.% (from phase II of project) was used to load 3.0 and 5.0 wt.% Fe on the optimized support to yield

resulting catalysts (for phase III) labeled as Cat-H and Cat-I, respectively. Details of the optimization regimen are summarized in section 4.26 (Table 4.2). The optimum catalyst found from the metal loading optimization was used to carry out kinetics and long-term deactivation studies for this catalyst system and are discussed in section 4.5.

3.3.5 HDS and HDN kinetics study

In this section, hydrotreating process parameters investigation was conducted for the determined optimum SBA-15-supported FeW catalyst. The details of kinetic study plan followed in experimental runs are also addressed. Table 3.1 shows the kinetic study plan implemented in this section. The first section of Table 3.1 shows a typical running schedule as described in section 6.2 for process temperature studies. The kinetic study plan carried out for the optimum SBA-15-supported FeW catalyst subsequently followed and was divided into two main phases: 1) Variation of LHSV and system pressure and their effects on sulfur and nitrogen conversions; 2) Variation of H_2/HGO ratio (*G/L*) and its effect on the HDS and HDN reaction rates.

Prior to the LHSV and system pressure study, a 5-day precoking procedure was carried out, followed by the collection of kinetic data evaluated at three different reaction temperatures (375, 388, and 400°C) for a 3 day period, respectively. Similarly, three different space velocities (0.5, 1.5, and 2.0 h^{-1}) and pressures (7.6, 8.3, and 9.6 MPa) were also investigated.

Table 3.1: Kinetic study plan for hydrotreating process parameters study using the optimum FeW/SBA-15 catalyst (Catalyst = 5 mL, P = 7-10 MPa, LHSV = 0.5-2 h^{-1} and H_2/oil ratio = 400-1000 mL/mL).

Study	Elapsed run time (days)	Temperature (°C)	LHSV (h^{-1})	Pressure (MPa)	H_2/Oil (mL/mL)
Precoking	1-5	375	1.0	8.8	600
1st Temperature	6-7	375	1.0	8.8	600
2nd Temperature	8-10	388	1.0	8.8	600
3rd Temperature	11-13	400	1.0	8.8	600
1st Temperature_R	14-16	375	1.0	8.8	600
Effect of process parameter study					
Parameter	**Elapsed run time (days)**	**Temperature (°C)**	**LHSV (h^{-1})**	**Pressure (MPa)**	**H_2/Oil (mL/mL)**
LHSV_0.5	17-19	388	0.5	8.8	600
LHSV_1.5	20-22	388	1.5	8.8	600
LHSV_2.0	23-25	388	2.0	8.8	600
Pressure_1st	26-28	388	1.0	7.6	600
Pressure_2nd	29-31	388	1.0	8.3	600
Pressure_3rd	32-34	388	1.0	9.6	600
G/O_1st	35-37	388	1.0	8.8	400

G/O_2nd	38-40	388	1.0	8.8	800
G/O_3rd	41-43	388	1.0	8.8	1000
Stability study	44-103	388	1.0	8.8	600

Furthermore, a qualitative study of the hydrogen-to-heavy gas oil volumetric ratio was then varied (400, 800, 1000 mL/mL) over a period of 9 days to determine their effects HDS and HDN reaction rates. Products sampling and stripping was carried out daily (24-hours) for each process parameter investigated. After kinetic data collection at the various operation conditions, three main kinetic models (Power Law, Langmuir-Hinshelwood, and Multi-parameter models) as described in section 4.4.2 were applied to evaluate model parameters and subsequently compared. A statistical analysis was performed on each of the function parameters to test their significance to the accuracy of the models.

3.3.6 Catalyst stability and long-term deactivation study

In order to determine the true effectiveness of a FeW/SBA-15 catalyst compared to a commercial FeW/γ-Al_2O_3 catalyst, a long term study was performed under maintained reaction conditions. To monitor how catalyst deactivation from coking affected the HDS and HDN activities of the FeW/SBA-15 catalyst over the long term, a performance test was carried out over the span of 60 days time-on-stream. Product samples were collected at 24 hour intervals at the following reaction conditions: 388°C reactor temperature, 8.8 MPa system pressure, 1.0 h^{-1} LHSV, 600 mL/mL H_2/HGO ratio, and a 1.5 g (~5.0 mL) catalyst loading. The same test was

performed for a FeW/γ-Al_2O_3 catalyst under identical conditions and with an equivalent 5.0 mL volumetric loading. Given that the commercial γ–alumina-supported FeW catalyst was three times denser than the FeW/SBA-15 catalyst, this corresponds to an approximate 4 g mass loading for the commercial γ–alumina-supported FeW catalyst studied. Due to time constraints for this project, only a 60-day period of longevity study was evaluated, even though typical industrial scale catalyst longevity studies may span over several months.

4.0 RESULTS AND DISCUSSION

This chapter gives detailed discussion of the results related to the research principal objectives outlined in section 3.0 as follows: 1) Syntheses of SBA-15 supports and FeW/SBA-15 catalysts of different pore diameters; 2) Supports and FeW/SBA-15 catalysts characterizations; 3) Catalytic performance evaluation using heavy gas oil derived from Athabasca bitumen; 4) Metals optimization studies on the optimum catalyst support, characterizations and subsequent catalytic performance evaluation; and 5) Kinetics and long-term deactivation studies for the optimum catalyst produced. Attempts have been made to interpret these results with annotated figures and respective tables. The prime objective is to explain how the optimum SBA-15-supported FeW catalyst was obtained and ultimately how to best predict its catalytic performance and stability over an extended running period under pre-determined process conditions.

4.1 Syntheses of SBA-15 and FeW/SBA-15 catalysts of different pore diameters

The synthesized pristine SBA-15 materials were first subjected to a series of characterization techniques so as to ascertain their overall quality before being applied in the FeW/SBA-15 catalyst preparation. To determine how SBA-15 materials of variable pore diameters were obtained, the amount of hexane (C_6H_{14}) and ammonium fluoride (NH_4F) molar ratio was varied in the range of 60-180. This molar ratio variation significantly influenced the pore channels of the resulting materials produced. The introduction of hexane (as a swelling agent) into the acidic synthesis medium may have caused an expansion of the hydrophobic volume of the micelle

cores. It is noteworthy to mention that the P123 template used for the synthesis of these SBA-15 materials has a greater portion of its chain length in the hydrophobic range (i.e. the propylene glycol block). Thus by increasing the C_6H_{14}/NH_4F molar ratio, more of the hexane is made available to the micelles for the swelling of the pores; probably due to the hydrophobic nature of hexane. Increasing the amount of swelling agent resulted in an increase in the BJH pore diameter and pore volumes alike; however, the pore size distribution of the catalyst with the largest pore diameter became more skewed and exhibited a relatively broader pore size distribution (see Figure 4.7). Even though it is quite noticeable from the TEM images of the catalyst with the largest pore diameter (Cat-D) that the pore sizes appear not very well-defined, a probable pore collapse may be suggested to explain this observation.

4.2 Supports and FeW/SBA-15 catalysts characterizations

The quality of the produced materials was first analyzed via small-angle x-ray scattering (SAXS) technique and subsequently other spectroscopic and analytical techniques. These techniques include N_2 adsorption/desorption, transmission electron microscopy, scanning electron microscopy, energy dispersive X-ray analysis, inductively coupled plasma mass spectroscopic analysis, Fourier Transform Infrared Spectroscopy, DRIFT spectroscopy, carbon monoxide uptake analysis, and thermogravimetric analysis. Details of results obtained by these techniques are addressed in subsections that follow.

4.2.1 Small-angle X-ray scattering analysis

The XRD measurements were carried out to study the mesoporous structure of the supports and catalysts. The crystalline phases of the calcined catalysts can also be obtained by this technique. The low angle XRD pattern of Fe-W catalysts supported on SBA-15 of different pore diameters are shown in Figure 4.1 in the interval between the 2θ values of 0.5 – 10°.

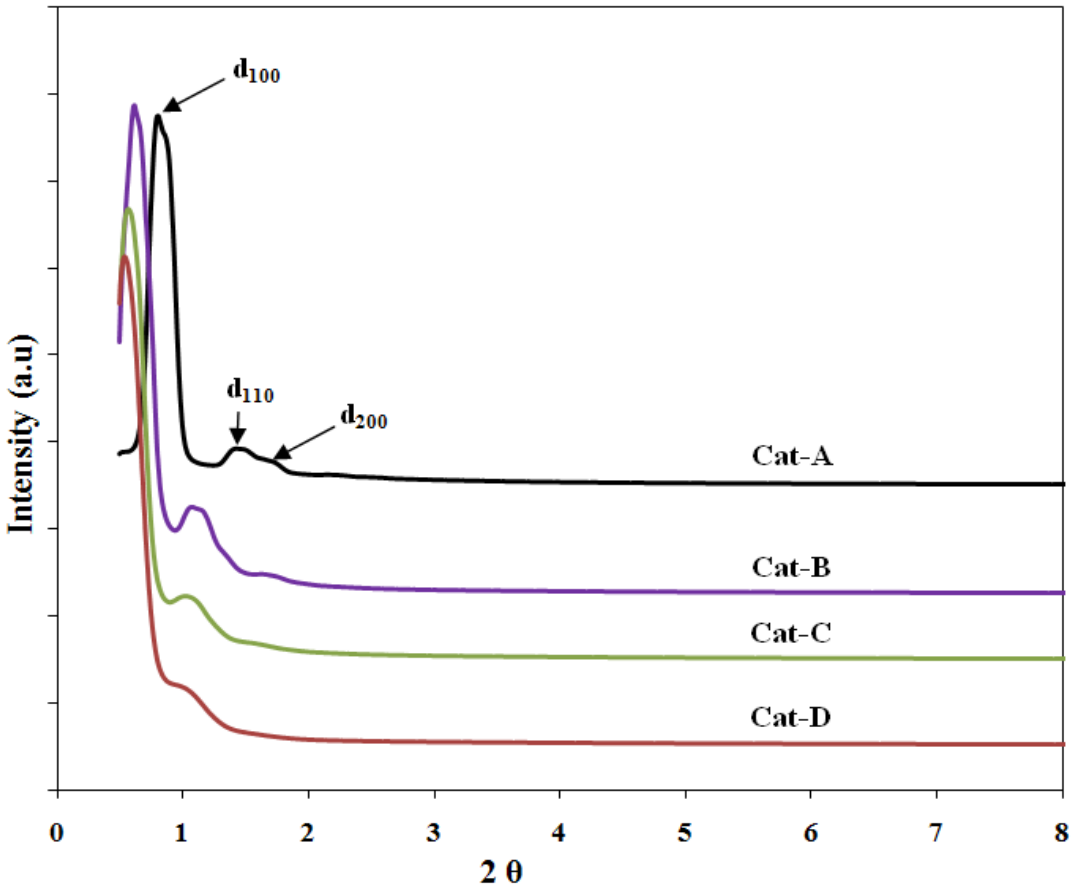

Figure 4.1. Small-angle X-ray profiles of FeW/SBA-15 catalysts of different pore diameter

The small-angle X-ray scattering patterns of the calcined SBA-15-supported FeW catalysts exhibit three well-resolved peaks, characteristic of SBA-15 materials (Zhao et al., 1998). These XRD peaks are indexable as (d_{100}), (d_{110}) and (d_{200}) reflections associated with the p6mm symmetry of the hexagonal ordered pore structure. Hexagonal order remains more or less intact after pore diameter increase. The peaks corresponding to d_{110} and d_{200} planes exhibited minor changes; revealing a slight structural change of SBA- 15 with pore swelling. Similar, changes in the d_{110} and d_{200} diffraction planes were observed in Cats-E to I. This could be attributed to the higher metals loading causing minor changes in the structure of the pure SBA-15 support.

4.2.2 Broad-angle X-ray Diffraction

The broad angle X-ray diffraction patterns of siliceous SBA-15 and Fe-W/SBA-15 catalysts with similar metal loading but different pore diameters recorded in the 2θ interval of 10° to 80° are shown in Figure 4.2. It can be seen from Figure 4.2 that the presence of crystalline phases were not detected in Cat-A, B and C; suggesting that either metals were homogeneously dispersed on the support or their compositions were below the detection limit of the X-ray signals. The absence of XRD signals in wide angle region indicates that the particle size of metals is below the coherence length of X-ray scattering i.e., smaller than ~40 Å. However, the single broad hump exhibited by all samples and centered at 2θ values of 15-40º is characteristic of siliceous materials (Zepeda et al., 2006). The X-ray result reveals that Fe and W are well dispersed and are probably present as a monolayer.

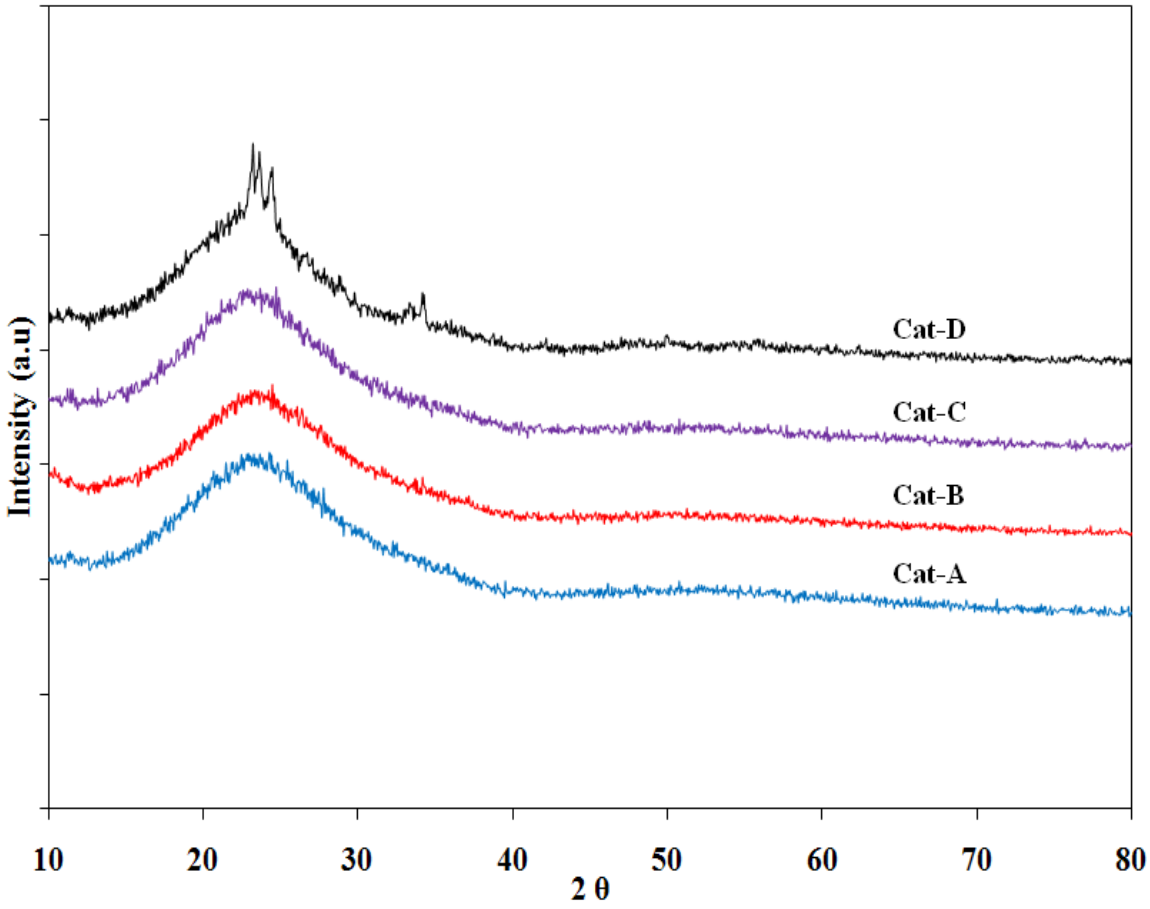

Figure 4.2: Broad-angle X-ray diffraction patterns of SBA-15-supported FeW catalysts of variable pore diameter

The high surface area of silica support favors dispersion of the active phases. However, in the case of Cat-D some crystalline peaks can be observed due to the poorly crystalline species of W and Fe in the oxidic phase appearing at 2θ values of 23.5 and 34.2, respectively. The species observed at 2θ value of 23.5 can be assigned to monoclinic WO_3 crystalline phase (JCPDS card 35–609); while the small and weak broad peak observed at 2θ value of 34.2 has been attributed to α-Fe, which manifests as small iron oxide crystallites with a spinel structure (Pozas et al., 2006). The poor dispersion of the oxide phases in Cat-D may explain the notable loss of hydrotreating

activity. This is due to the fact that amongst the four catalysts prepared, Cat-D has the largest pore diameter; however, its least surface area may have contributed to the formation of aggregates as detected by the X-ray.

The XRD patterns of SBA-15 supported FeW catalysts of variable Fe and W loadings can be seen in Figure 4.3.

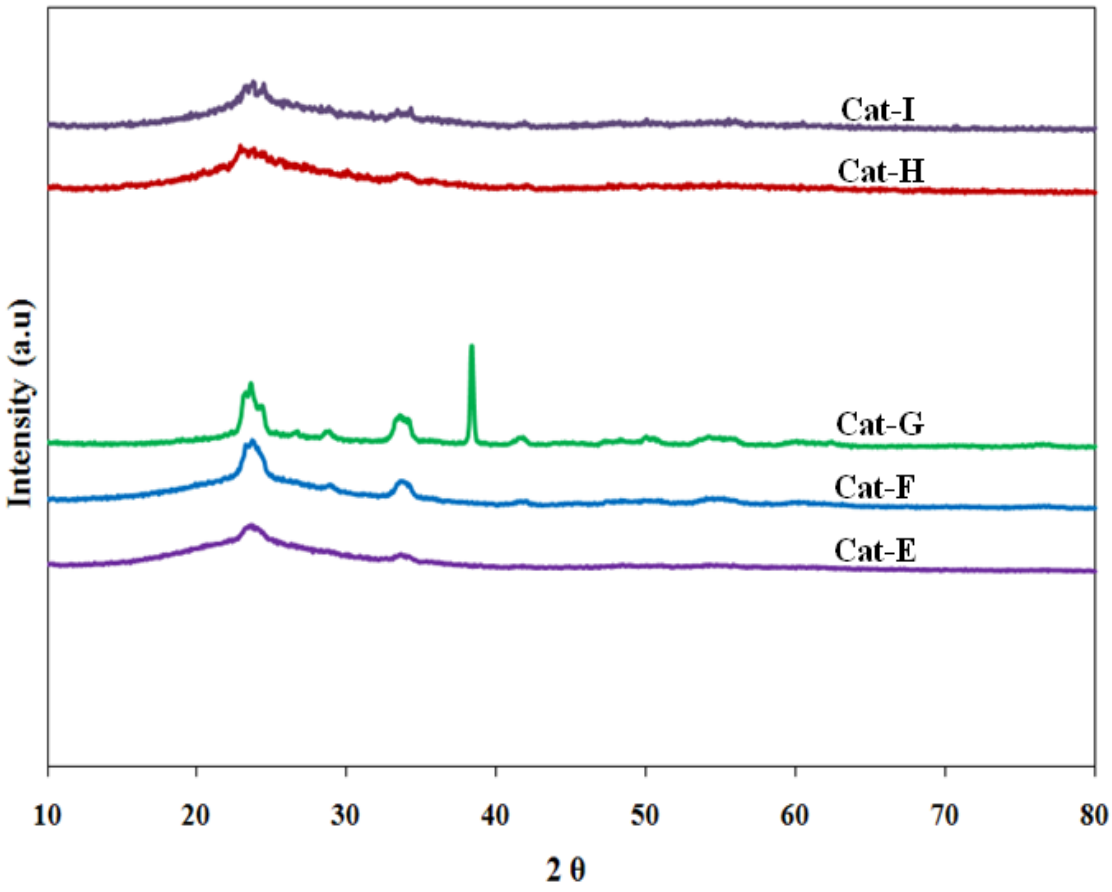

Figure 4.3: Broad-angle X-ray diffraction patterns of SBA-15-supported FeW catalysts of variable Fe and W metals loading

All catalysts investigated (Cats E to I) evidenced the WO_3 crystalline phase, characterized by the appearance of the peak at a 2θ value of 23.5. Furthermore, one can observe an increase in the intensity of this peak in the order: Cat-E < Cat-F < Cat-G. This is attributable to the increasing quantity of tungsten introduced (i.e. 20, 30, and 45) in the catalyst preparation step. The crystalline peaks observed at 2θ values of 34.5 could as well be attributed to the spinel structure of iron oxide crystallites manifesting on the surface of these catalysts (Cat-E to G). The sharp spike observed on the XRD profile for Cat-G can be attributed to WO_3 crystalline phase, present in the monoclinic form (JCPDS card 35–609). For Cats-H and I with variable Fe loadings of 3 and 5 wt.%, respectively, and constant W loading of 30 wt.%, the peaks seem to diminish in intensity; probably due to the formation of FeW oxidic phase that appeared to be well dispersed on the support.

4.2.3 N_2 adsorption-desorption isotherms measurement

The textural properties of mesoporous materials can be examined by N_2 adsorption-desorption isotherms at 77K. The nitrogen adsorption-desorption isotherms of a typical siliceous SBA-15 support is shown in Figure 4.4. It is typical of mesoporous materials to evidence a type IV isotherm with sudden increase in the volume of N_2 gas uptake corresponding to the capillary condensation. Generally, the hysteresis loops observed for porous solids is due to the mechanism of gas adsorption and desorption of porous solids, which is quite different from that of non-porous materials.

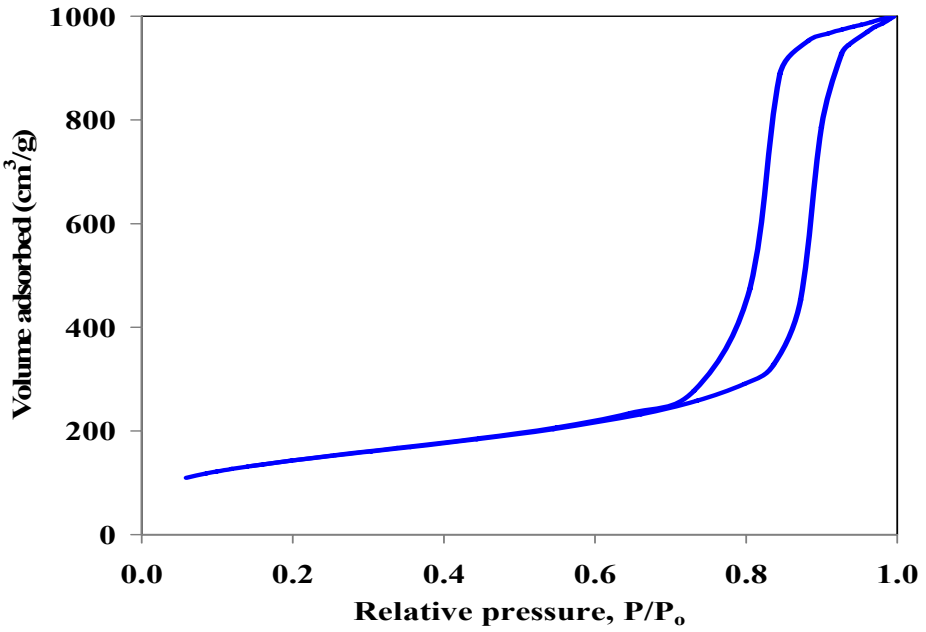

Figure 4.4: N_2 adsorption-desorption isotherm of a typical pure SBA-15 support

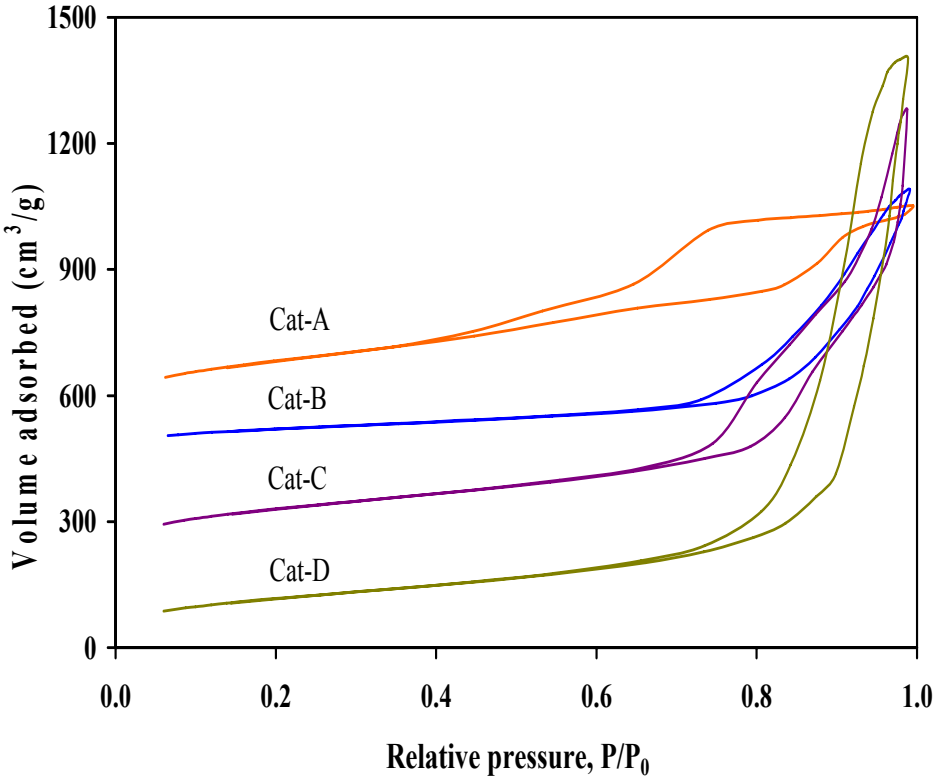

Figure 4.5: N_2 sorption isotherms of FeW/SBA-15 catalysts of different pore diameters (Cat A = 5.7 nm; Cat A = 10.1 nm; Cat A = 15.7 nm; Cat A=18.5 nm)

Figure 4.5 illustrates isotherms for four SBA-15-supported FeW catalysts with different pore diameters (as investigated in Phase I). Similar profiles were exhibited by catalysts screened as per phases II and III of the project. The textural and structural characteristics (surface area S_{BET}, total pore volume V_P, pore diameter D_P, unit-cell parameter a_0 and pore wall thickness) of the SBA-15 supports and their corresponding catalysts are given in Table 4.1. It should be noted that the same support was employed to prepare catalysts as used in phases II (studying the effect of variable W-loading at 2 wt.% Fe loading) and III (studying the effect of variable Fe-loading at 30 wt.% W loading), respectively.

All the FeW/SBA-15 catalysts exhibited the type IV isotherm with H1 hysteresis loop, which is characteristic of a well-formed SBA-15 material. The shape of the loop is unchanged after the Fe and W metals loading indicating that support and catalysts exhibit uniform textural porosity, which is also in agreement with XRD results. The height of the hysteresis loop is decreased after metals loading into SBA-15 due to a decreased pore volume indicating the introduction of metal species within the mesopores of the support. The surface area and pore volume of the SBA-15 decreased significantly after metal loading. Lizama et al. (2008) investigated the incorporation of active metals (Mo or W) on the SBA-15 support from either conventional precursors or heteropolyacid sources and observed that W-containing samples have lower values of surface area and pore volume than the corresponding Mo-containing ones because the loading of W metal is higher than that of Mo for maintaining active metal-promoter ratios.

Table 4.1: Physical properties of SBA-15 supported FeW catalysts with different pore diameter and variable metals loading determined from N_2 sorption and XRD analyses.

Sample ID	S_{BET} $(m^2/g)_{Sup}$	S_{BET} $(m^2/g)_{Cat}$	NS_{BET}	PV (cm^3/g)	PD_{ads} (nm)	d_{100} (nm)	a_0 (nm)	φ (nm)
Cat-A	895	651	0.88	0.64	5.7	9.9	11.4	5.7
Cat-B	636	498	0.94	0.89	10.1	12.4	14.4	4.3
Cat-C	491	396	0.97	1.00	15.7	16.9	19.5	3.8
Cat-D	473	388	0.99	1.09	18.5	17.9	20.7	2.2
FeW/γ-Al_2O_3	276	154	0.67	0.42	10.8	-	-	-
Cat-E	619	457	0.95	1.01	10.4	13.0	15.0	4.6
Cat-F	619	403	0.96	0.91	10.3	12.8	14.8	4.5
Cat-G	619	284	0.87	0.83	10.4	12.7	14.7	4.3
Cat-H	619	382	0.92	0.89	10.2	12.9	14.9	4.7
Cat-I	619	361	0.90	0.79	10.3	12.8	14.8	4.5

S_{BET}, specific surface area calculated by the BET method.
NS_{BET} (Normalized surface area) were calculated by using the equation, NS_{BET} = (S_{BET} of the catalysts)/ (1-x). S_{BET} of the support
PV, pore volume determined by nitrogen adsorption at a relative pressure of 0.98.
PDads, mesopore diameter corresponding to the maximum pore size distribution obtained from adsorption isotherm by the BJH method.
a_0, unit-cell parameter determined from the position of the (1 0 0) diffraction line as $a_0 = d_{100} \times 2 / \sqrt{3}$
φ, pore wall thickness calculated as $d_{100} = a_0$ - Dads.

The pore wall thickness (d) decreases with increasing unit cell parameter (a_o) which is measured by small-angle XRD. A decrease in the pore wall thickness as observed was due to increase in the pore diameter of the supports. In the case of Cat-D, the pore wall thickness is considerably less as compared to all other catalysts, making it susceptible to easy pore collapse under the severe HDT reaction conditions. The results from N_2 adsorption-desorption analysis correlates well with that obtained from XRD analysis. The pore size distributions of pure SBA-15 support and FeW/SBA-15 catalysts are given in Figures 4.6 and 4.7. The sharpness of the desorption branches is indicative of the narrow mesopore size distribution.

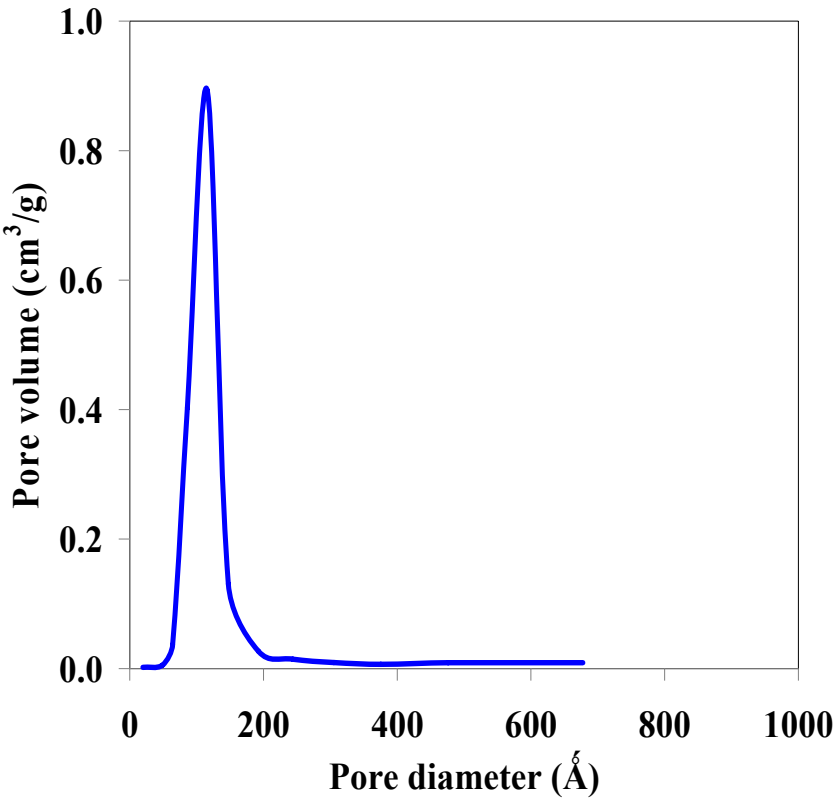

Figure 4.6: Pore size distribution profile of a typical pure SBA-15 support

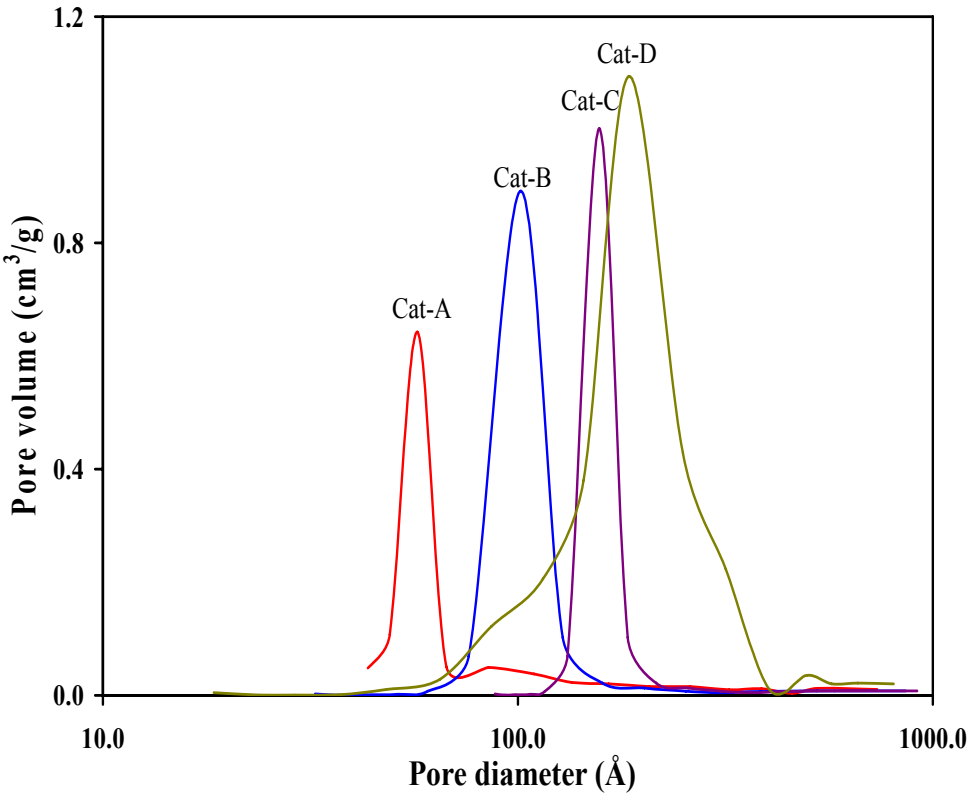

Figure 4.7: Pore size distribution profiles of FeW/SBA-15 catalysts of different pore diameters.

To confirm the presence of nanoparticles of Fe and W oxides in the pores of the SBA-15 substrate, the normalized S_{BET} values were calculated using an equation proposed by Vradman et al. (2005):

$$NS_{BET} = \frac{(S_{BET})_{Catalyst}}{(1-x) * (S_{BET})_{Support}}$$

where NS_{BET} is normalized S_{BET} and x is the weight fraction of the phases. The values of normalized NS_{BET} are given in Table 4.1. Values of NS_{BET} close to unity give an indication of less pore blockage. As seen in Table 4.1, the introduction of the Fe and

W particles caused a reduction in pore volume, which resulted in the reduction of normalized surface area. The normalized surface area of Cat-A was found to be 0.88, which is < 1. The NS_{BET} of SBA-15 supported catalysts increased with increasing pore diameters, indicating less blockage of the pores with the introduction of FeO and WO_3 nanoparticles. These results confirm that even though the large pore diameter of SBA-15 facilitated the ease of metal incorporation into the pore volume but did not necessarily improve dispersion of these metals; probably due to formation of agglomerates within the pores. However, apart from Cat-G, which showed some extent of pore blockage, the NS_{BET} results of all the catalysts analyzed suggested minimal pore blockage of the resulting catalysts studied.

4.2.4 TEM and SEM analyses

The structural morphology of SBA-15 supports was evidenced using TEM analysis. The TEM images of calcined SBA-15 supported catalysts with different pore diameters are shown in Figure 4.8.

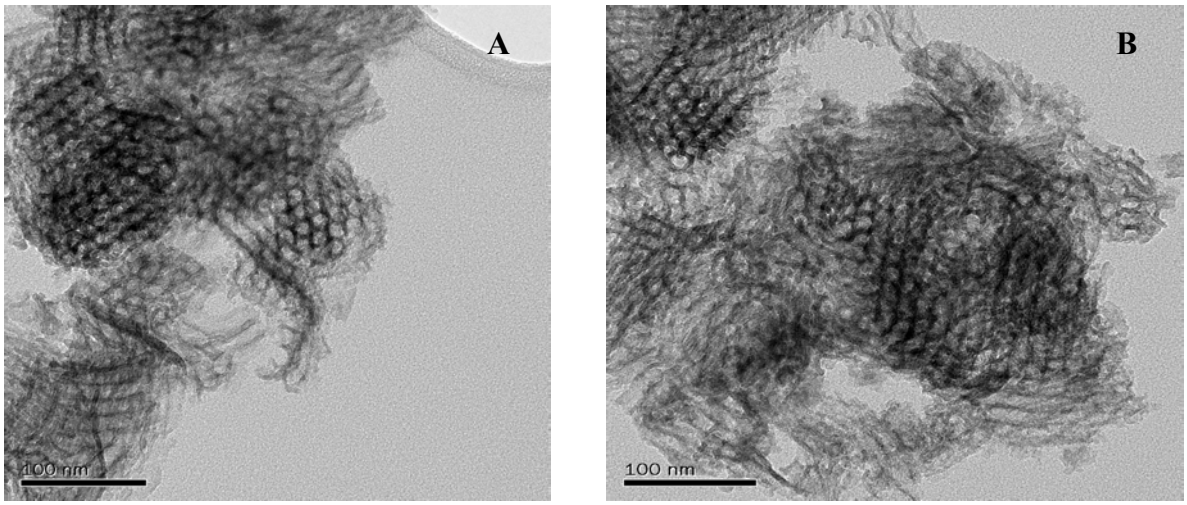

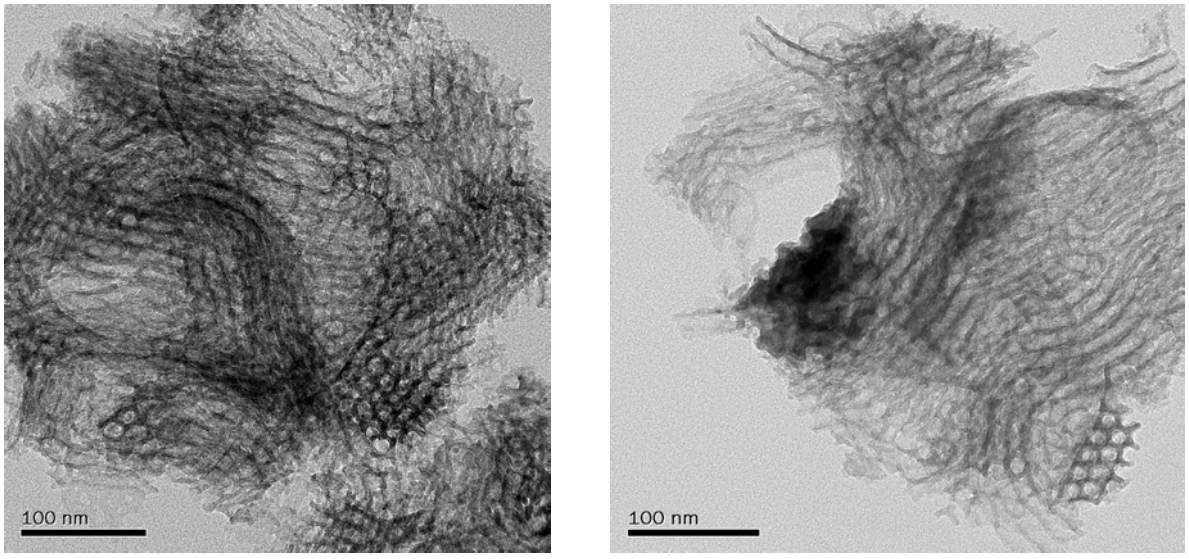

Figure 4.8: TEM images of FeW/SBA-15 catalysts of different pore diameters: (A) ×20k magnification, PD = 5.7 nm; (B) ×20k magnification, PD=10.1nm; (C) ×20k magnification, PD = 15.7 nm; (D) ×20k magnification; PD = 18.5 nm

All samples analyzed by the TEM technique evidenced well-ordered cylindrical channel-like pore morphology with a 2D hexagonal (p6mm) mesostructure (Cao et al., 2009). The TEM images provide a pictorial evidence of an ordered meso-structured SBA-15 silicate material. These images confirmed that the mesoporous and well-ordered structure of the SBA-15 was preserved even after metals loading and that the metals are well dispersed in the pore channels since no patches of metal aggregates or agglomerates were found for samples analyzed. The average distance estimated between two consecutive centers of hexagonal pores estimated from the TEM images are in the 5-20 nm range, which are consistent with N_2 physisorption results. Any deviation in the size of the pores was within ±0.5 nm. A couple of catalyst supports were synthesized under identical synthesis conditions and further

compared to establish the reproducible nature of synthesis procedure as well as the resulting SBA-15 pore diameters produced. The WO_3 nanoparticles are in the size range of 3-5 nm. The average size of crystallites, D, was calculated by the Scherrer's formula $D= 0.9\lambda/(\beta \cos \theta)$, where 0.9 is the shape factor, λ is 0.154 nm, β is the full width at half-height, and θ is the diffraction angle for a particular crystalline phase. The average particle sizes determined by TEM images are in good agreement with the corresponding crystalline sizes calculated by the Debye–Scherrer equation. Nonetheless, agglomerates of nanoparticles of WO_3 start to appear as the metals loading increased from 30 to 45 wt. %W.

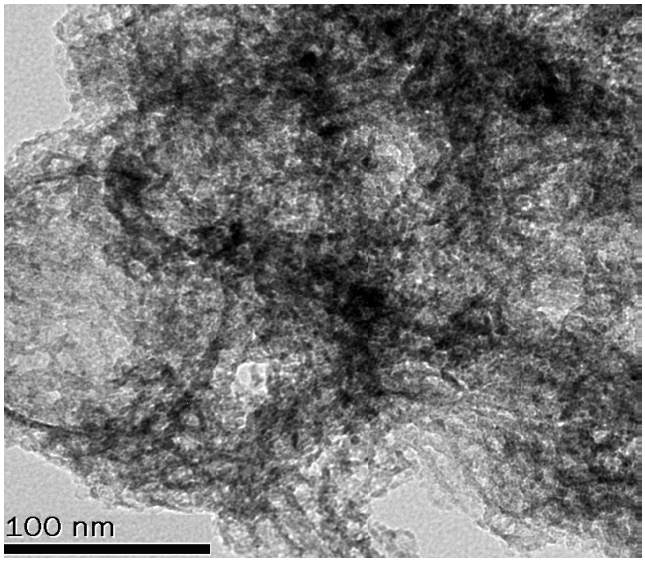

Figure 4.9: TEM image of FeW/SBA-15 catalysts of 3 wt.% Fe and 15 wt.%: (F) ×20k magnification, PD = 10.4 nm

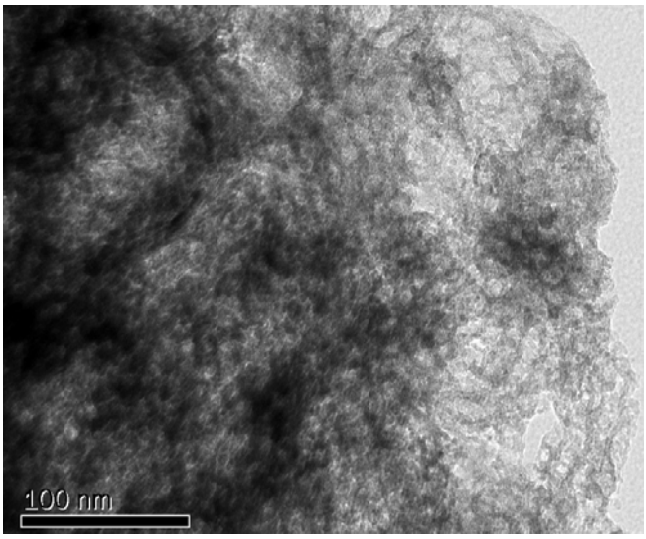

Figure 4.10: TEM image of FeW/SBA-15 catalysts of 2 wt.% Fe and 45 wt.%: (G) ×20k magnification, PD = 10.6 nm

This effect of metal loading is quite observable for Cat-G (having 2wt.% Fe and 45wt.% W) as confirmed by the XRD result. The average size range of these particles as determined by the Debye–Scherrer equation was in the range of 5-7 nm, which is large enough to cause pore blockage. The NS_{BET} value of 0.89 as calculated by the Vradman equation (Vradman et al., 2005), confirmed the conclusion by the TEM and XRD analyses that Cat-G suffered significant pore blockage and agglomeration of nanoparticles, respectively, probably due to its lower surface area; thus, resulting in its lowest HDS and HDN performance when screened with the heavy gas oil.

The SEM images of two different mesoporous SBA-15 materials are shown in Figures 4.11 and 4.12. Similar morphologies have been reported by other researchers (Zepeda et al., 2006).

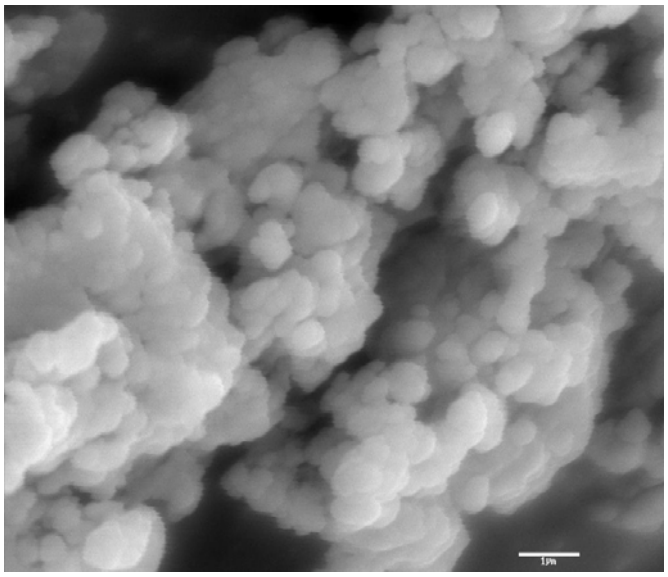

Figure 4.11: SEM image of pure SBA-15 support of 6.4 nm pore diameter

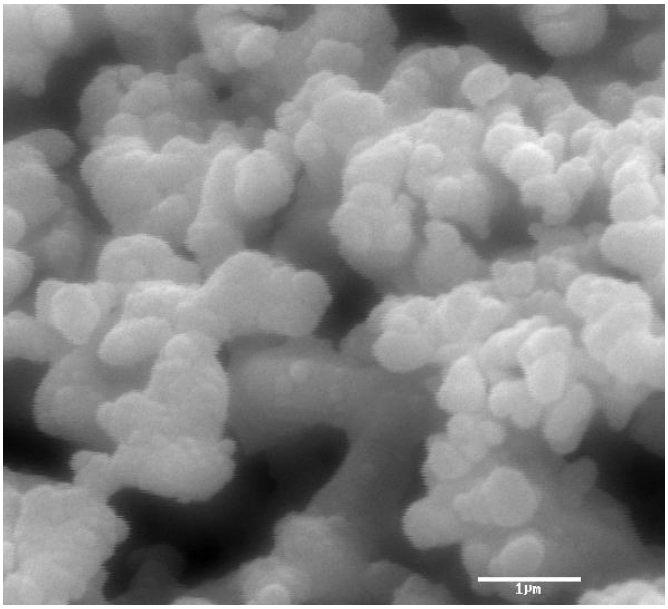

Figure 4.12: SEM image of pure SBA-15 support of 11.3 nm pore diameter

The SBA-15-supported FeW catalysts showed that all samples contained fiber-like particles several tens of micrometers in length Figures 4.13 and 4.14.

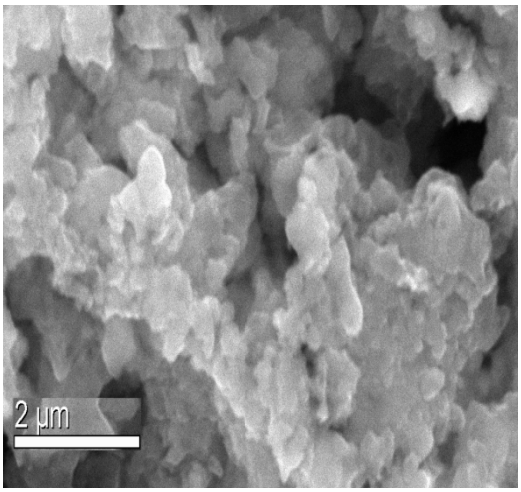

Figure 4.13: SEM image of FeW/SBA-15 catalyst of 5.7 nm pore diameter

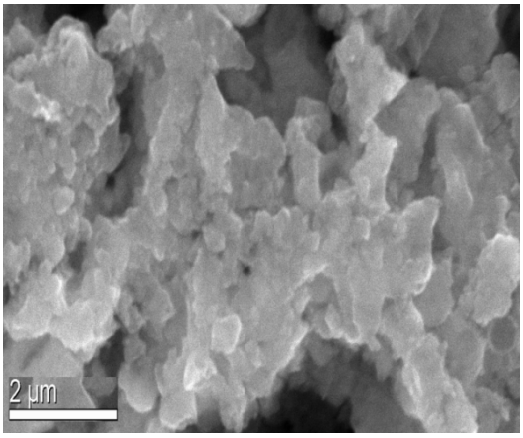

Figure 4.14: SEM image of FeW/SBA-15 catalyst of 10.1 nm pore diameter

4.2.5 Elemental analysis

The elemental compositions of all calcined Fe-W/SBA-15 catalysts were determined by ICP-MS and EDX analysis. The results of ICP-MS with targeted compositions are presented in Table 4.1. The elemental compositions obtained from ICP-MS and EDX correlate well with each other, as well as with targeted values.

4.2.6 DRIFT spectroscopy of CO adsorption

The nature of active species in the sulfided form of catalysts was studied by DRIFT spectroscopy of CO adsorbed catalysts. DRIFT spectroscopy of CO adsorption on the sulfided FeW catalysts with different pore diameters was performed at 30^{o}C to characterize the surface active sites. Figure 4.15 shows DRIFTS spectra of the above catalysts around C–O stretching region.

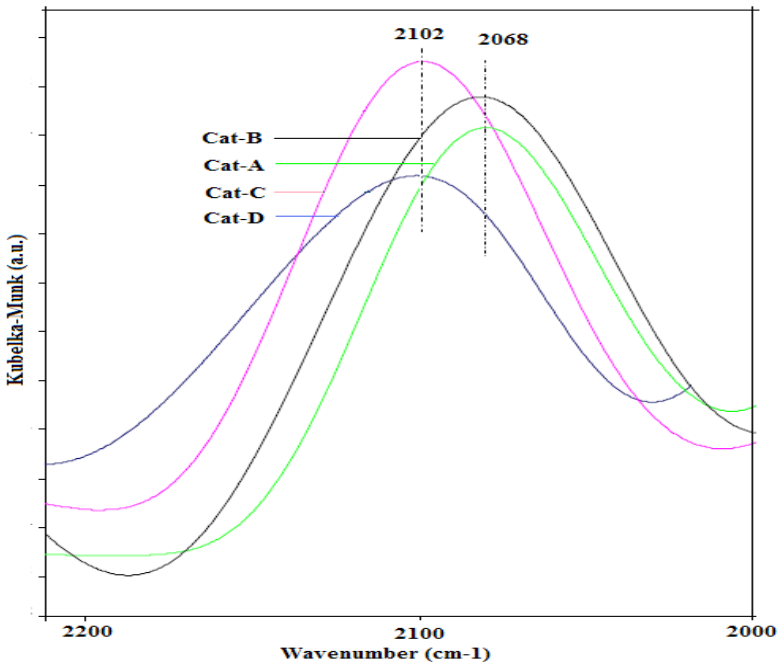

Figure 4.15: DRIFT spectroscopy for CO adsorption of FeW/SBA-15 catalysts of different pore diameters.

Adsorption of CO on sulfided catalysts yields strong bands at 2102 and 2068 cm^{-1}. Although there is no literature on CO adsorption studies on FeW/SBA-15 catalysts, the literature available on NiMo-supported catalysts shows two bands at 2098 cm^{-1} corresponding to CO adsorption on unpromoted Mo sulfide sites, whereas the band at 2062 cm^{-1} is due to the Ni promoted Mo sulfide sites (NiMoS phase) (Muller et al., 1993; Wu et al., 2000). The adsorption profile for FeW on SBA-15 shows similar results, indicating similar adsorption behaviors of CO molecules on FeW catalysts supported on SBA-15. In the case of Cat-C and Cat-D, the intense peak observed at 2102 cm^{-1} corresponds to unpromoted tungsten sulfides, which is indicative of a higher number of WS_2 phase. However, Cat-A and Cat-B exhibit a more intense peak at 2068 cm^{-1}, which suggests more adsorption of CO molecules at FeWS sites of FeW/SBA-15 catalysts. The presence of high FeWS centres in Cat-A and Cat-B supported catalysts show a higher number of active centres of Fe and W particles on the high surface area silica support. In the case of Cat-A and Cat-B, there is a disappearance of the band of corresponding to WS_2. A similar observation was made in the case of Cat-C and Cat-D in which the FeWS band is not available due to the overlapping with dominated phase. It can be deduced from the DRIFTS studies that catalysts with pore diameter in the range of 5 to 10 nm is responsible for higher number of co-ordinatively unsaturated sites.

Carbon monoxide adsorption at liquid nitrogen temperature was also used to quantify exposed surface metal atoms on sulfided catalysts. The CO uptake (μmol/g of cat.) measured from CO chemisorption is equivalent to the number of active metal

Table 4.2: Elemental composition, CO uptake, and HDS/HDN steady-state activities of SBA-15 supported FeW catalysts at various reaction temperatures (Catalyst = 5 mL, P = 8.8 MPa, LHSV = 1 h^{-1} and H_2/oil ratio = 600 mL/mL).

Phase	Sample ID	Composition (wt.%)		CO uptake (µmol/g)	Sulfur/Nitrogen removal at each temperature (wt.%)					
					375 (°C)		388 (°C)		400 (°C)	
		Fe	W		S	N	S	N	S	N
I	Cat-A	2*(1.95)	15*(14.58)	17	44	9	54	14	64	26
	Cat-B	2*(1.91)	15*(14.07)	25	45	17	53	17	66	33
	Cat-C	2*(1.91)	15*(14.20)	15	31	11	38	12	62	17
	Cat-D	2*(1.95)	15*(14.44)	10	30	5	38	7	43	3
	FeW/γ-Al_2O_3	2*(1.96)	15*(15.01)	33	69	16	80	32	89	49
II	Cat-E	2*(1.89)	20*(14.20)	26	35	10	42	13	47	14
	Cat-F	2*(1.86)	30*(29.84)	29	50	18	59	20	70	35
	Cat-G	2*(1.93)	45*(43.01)	32	38	9	45	15	56	18

III	Cat-H	3*(2.82)	30*(29.24)	31	53	22	64	26	73	38
	Cat-I	5*(4.76)	30*(29.51)	30	44	14	53	17	64	21

*Targeted

atoms that are accessible to the reactant molecules. Results of CO uptake for all the catalysts prepared in all phases of the project are summarized in Table 4.2.

The amount of CO uptake for catalysts studied in phase I increased from Cat-A to B; yielding a maximum in the case of Cat-B, then gradually decreased to Cat-D. This trend could be attributed by the fact that as the pore diameter increased from Cat-B to D, exposed metals increasingly became inaccessible to CO molecules due to the probable pore collapse as a result of increasing the pore diameter. These results give an indication that Cat-B has the highest number of active sites due to its highly dispersed metal phases. The amount of CO adsorbed by the optimum FeW/SBA-15 catalyst (Cat-H) was 31μmol/g of catalyst, which was slightly lower than that adsorbed by the FeW/γ-Al_2O_3 counterpart; giving an indication of a greater number of exposed active metal sites in the latter catalyst.

4.2.7 Thermogravimetric analysis

The TGA profile of a typical SBA-15-supported FeW catalyst is displayed in Figure 4.16. Of all the catalyst samples analyzed by this technique, each one exhibited a similar profile as depicted in Figure 4.16. It can be seen from the figure that the analyzed catalyst sample suffered a significant weight loss of ~30% in the temperature range of 80-120°C. This observed decrease in sample weight can be attributed to the desorption of physisorbed moisture from the surface of the catalyst. Apart from this significant weight loss, no major decomposition of volatile compounds was recorded by the samples.

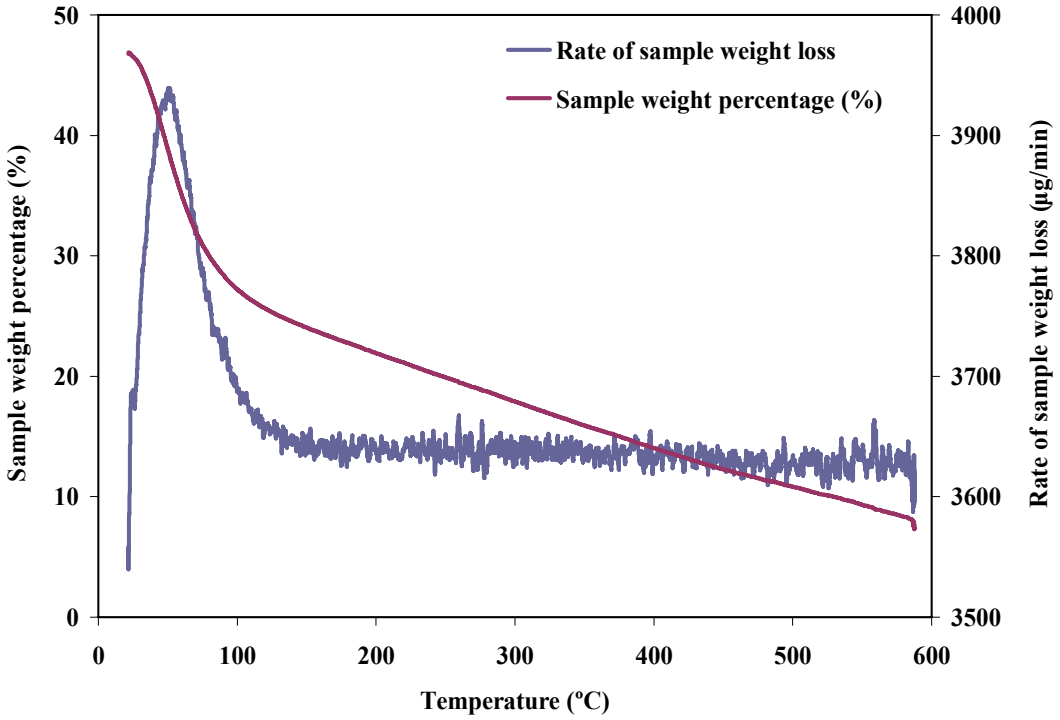

Figure 4.16: Thermogravimetric profile of a typical SBA-15 supported FeW catalyst.

Moreover, since no weight loss was observed between 320-350°C, it can be assumed that the polymer template (P123) used in the synthesis of the SBA-15 support was effectively removed during the calcination step. One can conclude from the TGA results that variation of the pore diameter as well as different metal loadings did not significantly affect the thermal stability of the FeW/SBA-15 catalyst samples.

4.2.8 Simulated Distillation

The boiling point range for the various hydrocarbon cuts present in the HGO feed stock and the resulting hydrotreated products were determined using simulated distillation procedure; and the results are display in Appendix A1. The SimDist results of samples analyzed from phase I (pore diameter optimization) of the project were compared with the composition of the HGO feed used for these runs as well as the

product liquid on a weight basis comparison with commercial γ–alumina-supported FeW catalyst. Using the boiling point distribution of a standard n-paraffin sample with molecular carbon numbers ranging from C_5 to C_{60}, the molecular compositions of the liquid HGO feed stock and hydrotreated products were divided into five sections as shown in Appendix A2. Figure 4.17 shows the graphical interpretation of these results at temperature and LHSV of 400°C and 1.0 h^{-1}, respectively.

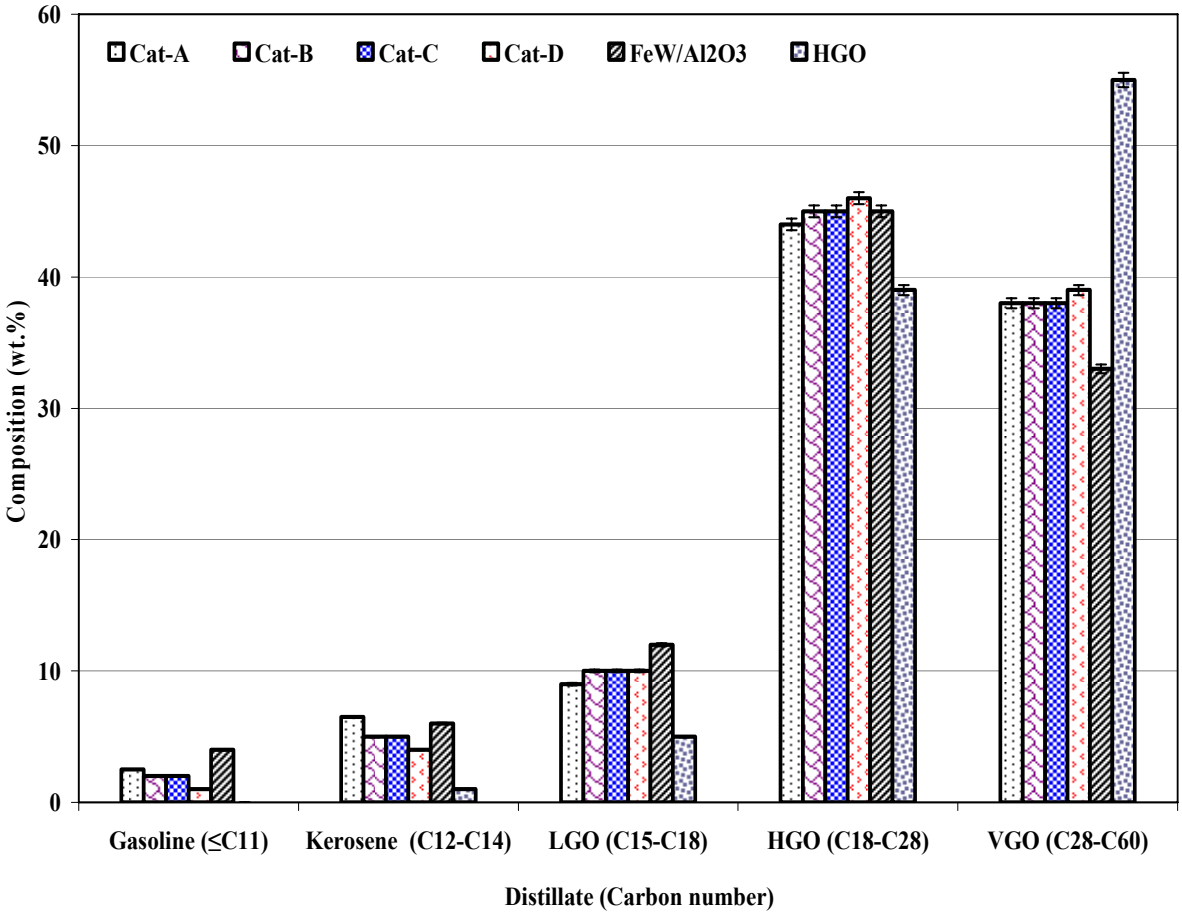

Figure 4.17: Distillates boiling ranges and carbon numbers of typical hydrocarbon fractions present in heavy gas oil (T = 400°C; P = 8.8 MPa; LHSV = 1 h^{-1}; H_2/HGO = 600 mL/mL; Catalyst loading = 5mL).

As depicted in this figure, the categorized molar composition of the product liquids facilitated the development of a relationship between the carbon numbers, their respective boiling ranges, and the pore diameter of the four FeW/SBA-15 catalysts studied. One can clearly notice that except for the heavy gas oil feed stock, the greatest composition of the distillate fractions were found to be hydrocarbons with carbon numbers in the range of 18 to 28. A general trend observed for all catalysts studied followed: C_{18}-C_{28} > C_{28}-C_{60} > C_{15}-C_{18} > C_{12}-C_{14} > C_{11}-. Furthermore, it must be noted that the catalyst with the largest pore diameter (Cat-D) produced the least amount of distillates of carbon numbers in the range of C11 to 14 at the temperature of study. This suggests that as the pore diameter increased, less fractions of hydro-cracked products were produced due to the fact that molecules with carbon numbers greater than 14 did not suffer hindered diffusion into the pores. Nonetheless, more lighter fractions were produced with the catalyst having the smallest pore diameter (Cat-A), probably due to the fact that bulkier fractions present in the heavy gas oil might have suffered hindered diffusion at the pore mouth of such catalysts; thereby enhancing cracking into smaller fractions under the severe hydrotreating conditions. It may also be observed from the figure that Cats-B and C (having pore diameters in the medium range) yielded about the same amount of distillate fractions at the various individual cuts. This suggests that to optimize the production of less hydro-cracked and heavier hydrocarbons, catalysts selection requirements must consider catalysts with pore sizes in the medium range (10-15nm).

It is noteworthy to mention that the commercial γ-Al_2O_3-supported FeW catalyst used for this experiments has an average pore size in the defined medium range. As can be seen from Figure 4.18, such a catalyst showed a markedly higher production of hydro-cracked products at all three temperatures studied.

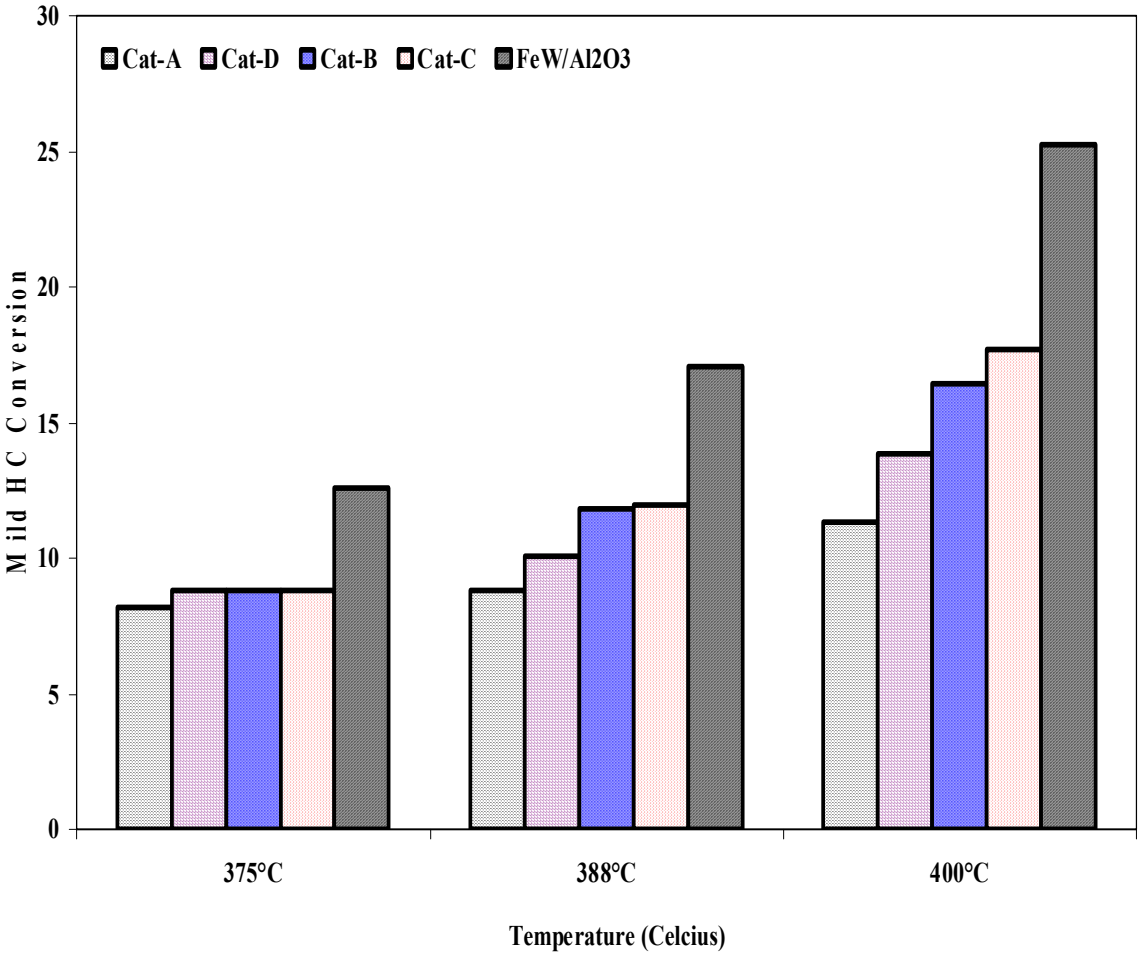

Figure 4.18: Effect of mild hydrocracking conversion as a function of temperature and FeW/SBA-15 catalysts of variable pore diameters (T = 375-400°C; P = 8.8 MPa; LHSV = 1 h^{-1}; H_2/HGO = 600 mL/mL; Catalyst loading = 5mL).

This could be explained by reason of the mildly acidic nature of the γ-Al_2O_3 support; thus contributing to the cracking and alkylation reactions characteristic of acidic supports as compared to the less acidic siliceous SBA-15-supported catalysts. At lower temperatures, insignificant levels of mild hydrocracking conversions were recorded by the FeW/SBA-15 catalysts of variable pore diameters. However, at higher temperatures (388 and 400ºC), the effect of mild hydrocracking became more pronounced due to the reduction in viscosity of the feed with temperature. This enhanced the diffusion of feed molecules into the active sites of the catalysts. The results show a trend of more extensive molecular refinement occurring as the pore diameter of the SBA-15 supports become smaller. The reverse trend appears to be the case for carbon numbers >C_{20}; as a higher concentration of these molecules are found as the pore diameter of the catalyst support becomes larger. It could be concluded from these results that making the pores of the SBA-15 supports more confined leads to more extensive cracking of the HGO molecules during the hydrotreating process at higher temperatures studied.

4.3 Catalytic performance tests of FeW/SBA-15 catalysts

Based on the characterization results of synthesized SBA-15 supports, phase I of the project saw the preparation of four FeW/SBA-15 HDT catalysts with varied pore diameters (5, 10, 15, and 20 nm) and designated as Cat-A, Cat-B, Cat-C and Cat-D, respectively. This was made possible by varying the molar ratio of hexane (micelle expander) and NH_4F in the range of 60-180 so as to achieve catalysts with inner diameters ranging from 5 to 20 nm. To determine the optimum pore diameter for

FeW/SBA-15 catalysts prepared, the four catalyst grades were evaluated for their HDS and HDN performance under typical industrial hydrotreating conditions. The intended Fe and W loadings for these catalysts was consistent with most commercial NiMo/γ-Al_2O_3 catalysts at 2.5 and 13.0 wt %, respectively. The optimum catalyst selected from studies of phase I was used in phases II and III, respectively to optimize both W and Fe loadings. Detailed HDS and HDN activity results are discussed in the following sections.

4.3.1 Effect of precoking on sulfur and nitrogen conversion

Precoking of catalysts is necessary to stabilize its initial high activity. Figures 4.19 & 4.20 show the effect of precoking on sulfur and nitrogen conversions of Fe-W/SBA-15 catalysts with different pore diameters. As can be seen from Figures 4.19 and 4.20, the sulfided catalysts had very high initial activity at the start-of-run (SOR) of the HDT reactions which dropped suddenly with time-on-stream (TOS). The decrease in HDS and HDN activities was observed in the following order: Cat-A ≅ Cat-B > Cat-C > Cat-D. It can also be observed that the stability of Cats-A and B were better than that of Cats-C and D. Cat-C and Cat-D had high initial HDS and HDN activities at the start-of-run, but could not be maintained and subsequently dropped sharply as the reaction progressed (within 48 h period).

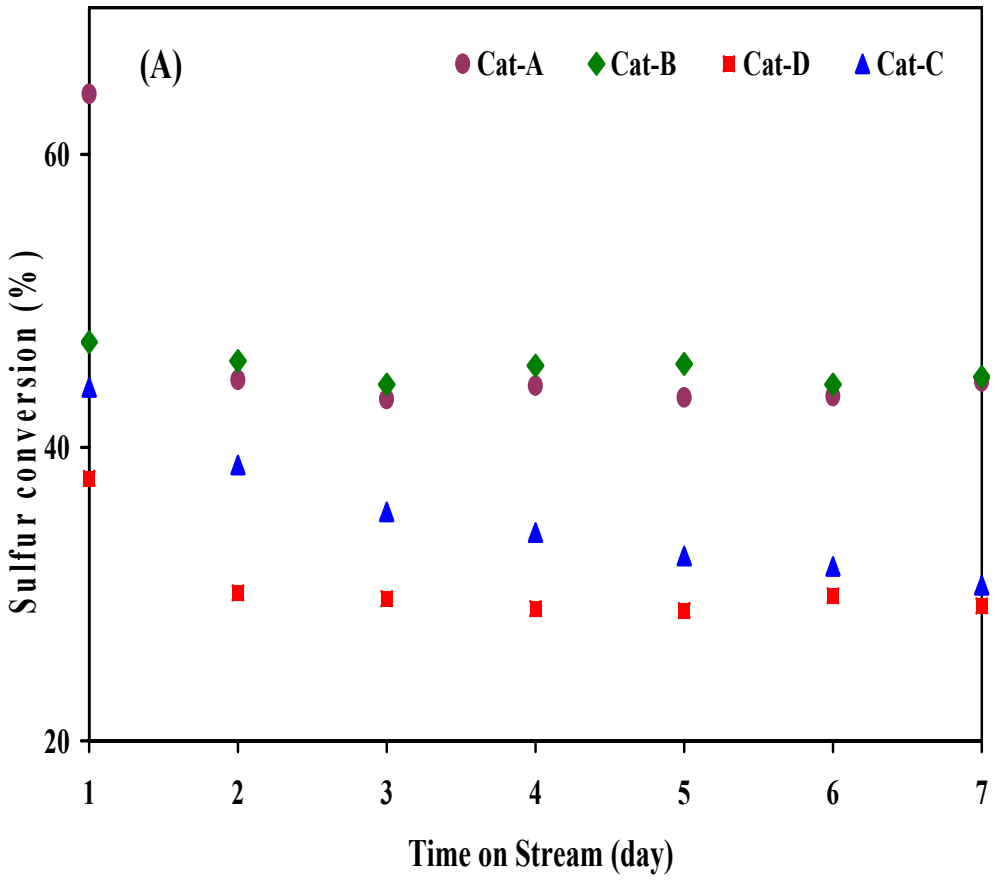

Figure 4.19: HDS activities of SBA-15-supported FeW catalysts during pre-coking with HGO at 375°C (catalyst = 5 cm^3, P = 8.8 MPa, LHSV = 1 h^{-1} and H_2/oil ratio = 600 mL/mL).

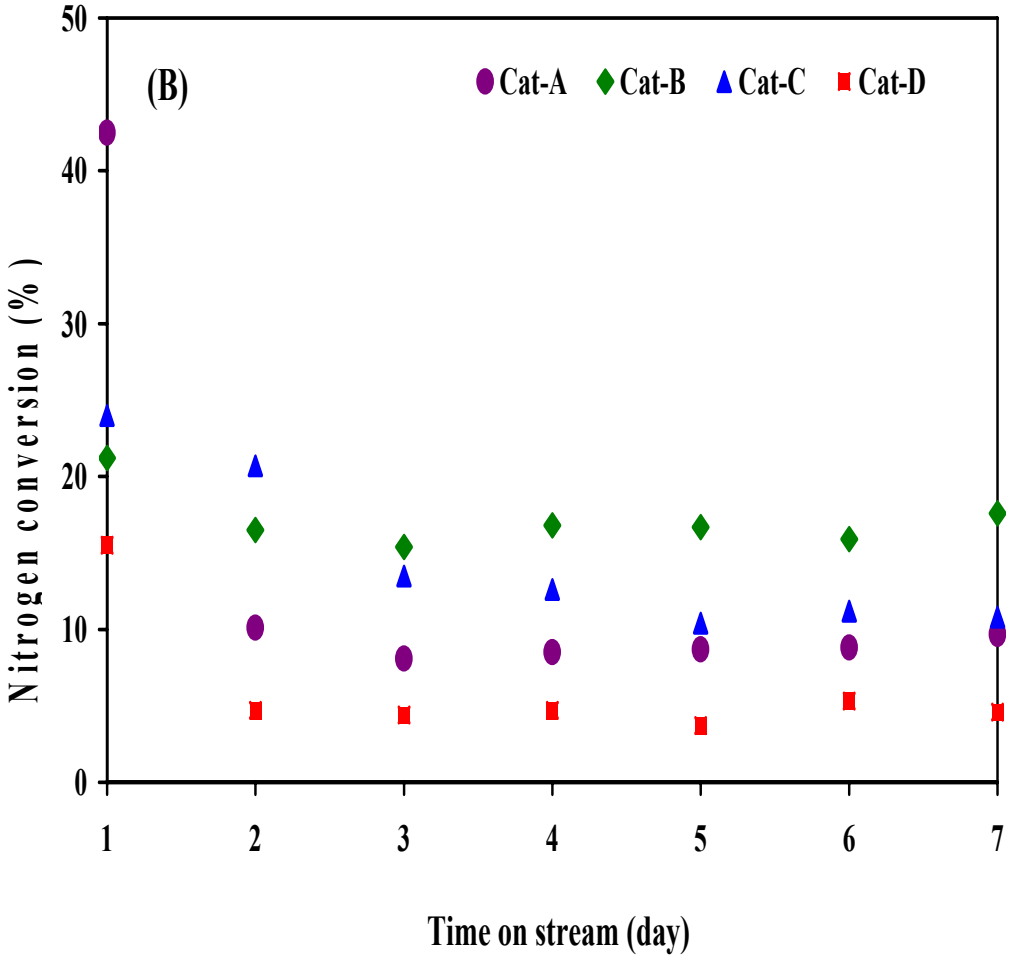

Figure 4.20: HDN activities of SBA-15-supported FeW catalysts during pre-coking with HGO at 375°C (catalyst = 5 cm^3, P = 8.8 MPa, LHSV = 1 h^{-1} and H_2/oil ratio = 600 mL/mL).

This observation could be attributed to their larger pore sizes as compared to that of Cats-A and B. This range of pore size is large enough for unhindered diffusion of a greater portion of low-molecular-size asphaltenes and other heteroatom-containing species that can undergo various reactions on the catalyst surface at the catalytically active centers within the pores. Some products formed in the reaction, such as carbonaceous species, can block the active centers. Consequently, deterioration of HDT activities in the larger pore supported catalysts could be observed within the initial 48 h period. A similar study conducted by Callejas et al. (2001) on the long-term (7,400 h) hydroprocessing of petroleum residue using commercial $NiMo/Al_2O_3$ catalyst concluded that coke deposition occurs rapidly on the catalyst surface during the early hours of the run (100 h), reaching as high as 12.4 wt. % of the catalyst. However, it deserves to be mentioned that catalyst grades studied in phases II and III of the project (i.e. Cat-E through I) showed similar precoking profiles as observed for the series of catalysts screened in phase I.

4.3.2 Effects of pore size on sulfur and nitrogen conversion

The ability of feedstock molecules to diffuse to the active centers within the pores is a key factor for determining the effectiveness of the catalyst (Ternan et al., 1983). As a result, phase I of the project investigated the effect of pore size on HDS and HDN activities. Generally, increasing the pore diameter of the catalyst facilitates diffusion of bulkier molecules from the bulk fluid to the active sites. However, this phenomenon solely does not necessarily translate into higher HDT activity. In the case of FeW/SBA-15, the results in Table 4.1 and Figure 4.21 & 4.22 show that HDS

and HDN activities generally passed through a maxima with respect to increasing the pore diameter in the range of 5.7 – 18.5 nm.

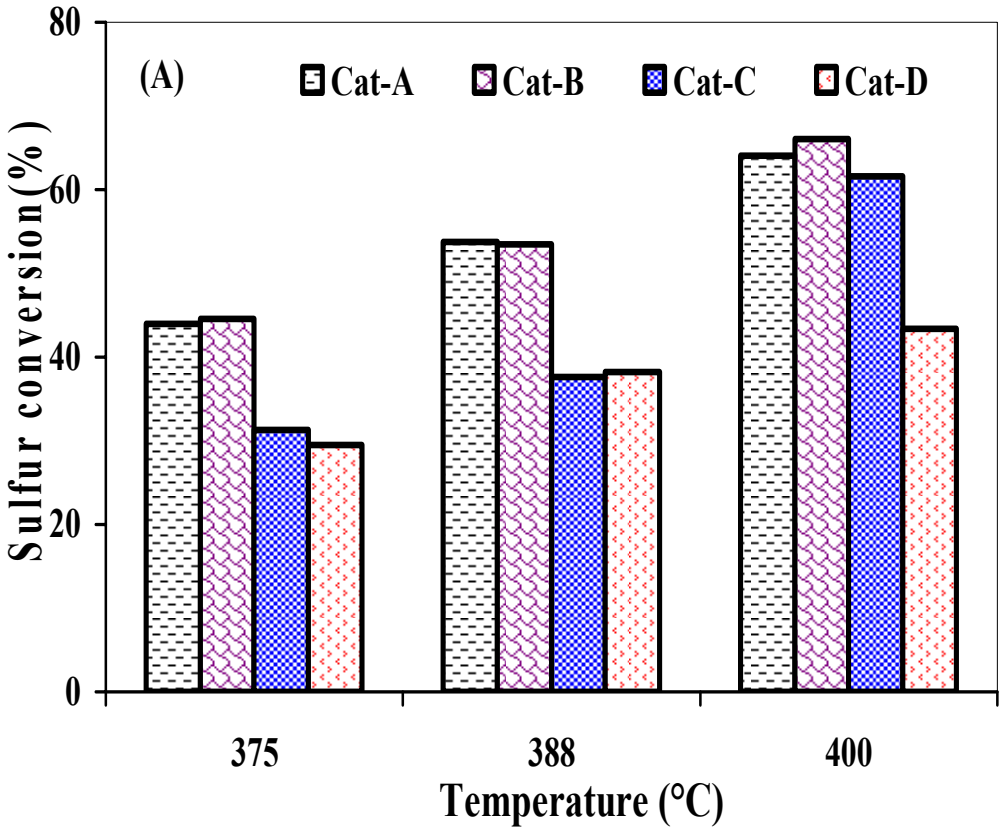

Figure 4.21: HDS activities of SBA-15-supported FeW catalysts during during the screening of HGO as a function of reaction temperatures (catalyst = 5 cm^3, P = 8.8 MPa, LHSV = 1 h^{-1} and H_2/oil ratio = 600 mL/mL).

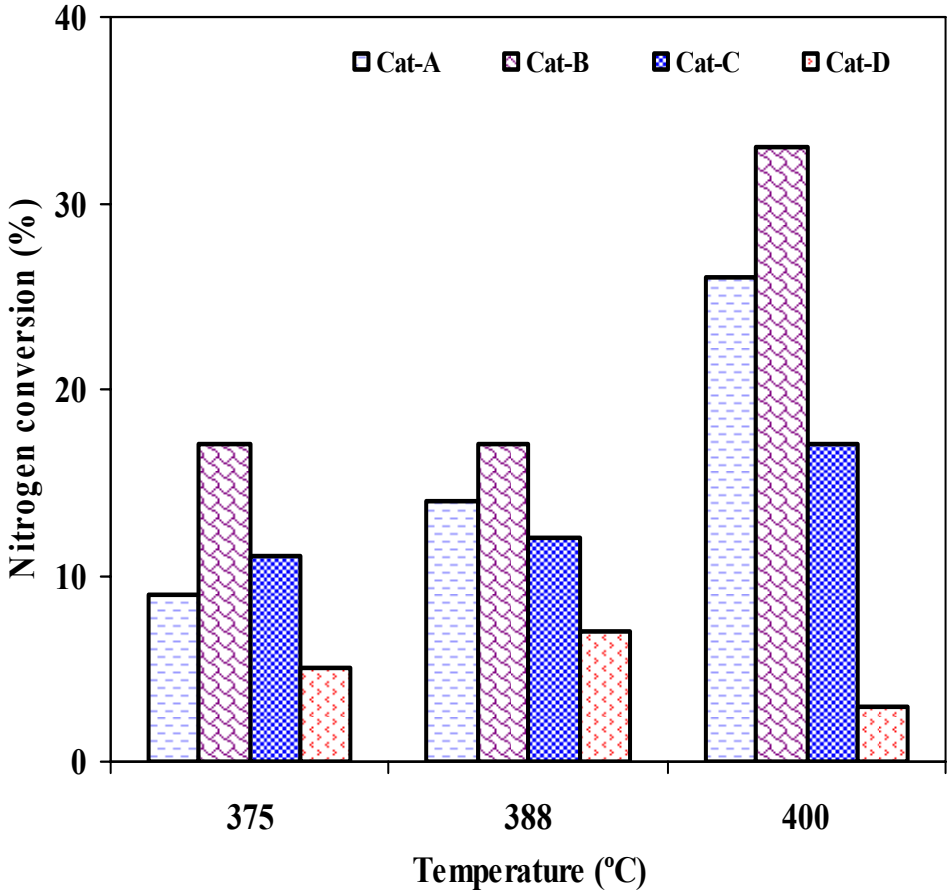

Figure 4.22: HDN activities of SBA-15-supported FeW catalysts during during the screening of HGO as a function of reaction temperatures (catalyst = 5 cm^3, P = 8.8 MPa, LHSV = 1 h^{-1} and H_2/oil ratio = 600 mL/mL).

As can be seen from Figure 4.21, the HDS activity remained almost the same for Cats-A and B of pore diameters 5.7 and 10.1 nm, respectively. This highest HDS activity recorded for these catalysts declined as the pore diameter was further increased from 10.1 to 15.7 nm, and subsequently to 18.5 nm. However, Figure 4.22 shows that HDN activity increased slightly with pore diameter (5.7 and 10.1 nm) and declined as the pore diameter further increased to 18.5 nm. This observed trend could be explained by the fact that, past a certain optimal pore diameter, increasing the pore diameter resulted in a decrease in surface area. It is worth mentioning that the surface area of a catalyst offers the platform for the dispersion of active metal components. However, the effective surface area required for metal dispersion suffered at the expense of increasing pore diameter. The decrease in surface area due to pore collapse (as evidenced by the TEM images) was responsible for the decrease in HDS and HDN conversions as the pore diameter increased. Thus, it can be concluded that by loading the same amount of metals (2 wt. % Fe and 15 wt. % W) on SBA-15 supports of different pore diameters resulted in an inhomogeneous dispersion of metals in the highest pore diameter catalysts (i.e., having the lowest surface area). This result was also confirmed by wide-angle XRD spectra showing the crystalline peaks of oxidic phases in Cat-D.

Furthermore, this observation could also be explained by the asphaltene content present in the feedstock, which was found to be 1.55 wt. % (Table 4.3).

Table 4.3: Characteristics of Heavy Gas Oil derived from Athabasca bitumen

Characteristic	Heavy Gas Oil
Nitrogen (wppm)	3615
Sulfur (wppm)	42,302
Density (g/ml)	0.99
Aromatic content (wt.%)	31.4
Asphaltene content (wt. %)	1.55
Boiling point distribution	
IBP (°C)	210.8
FBP (°C)	597.3
Boiling range (^{o}C)	**(wt%)**
IBP–205 (Gasoline)	0
205–260 (Kerosene)	1
260–315 (Light gas oil)	5
315–425 (Heavy gas oil)	39
425–600 (Vacuum gas oil)	55

The amount of asphaltene present in the HGO is quite significant as compared to the amount of catalyst loaded in the micro reactor (1.5 g); since it only requires a little amount of asphaltenes to significantly deactivate the catalyst. Due to their larger molecular weights (Takahashi et al., 2003), asphaltenes will preferentially diffuse and react in larger pores than they would in smaller pores. This resulted in the production of smaller hydrocarbons which are the main precursors for carbonaceous species deposition on the catalyst active sites. This conversion of asphaltene molecules to coke is a plausible explanation for the decreased HDS and HDN activities in the larger pore diameter catalysts. A similar explanation was provided by Song et al., 1991, who studied the effect of pore structure of Ni-Mo/$A1_2O_3$ catalysts in hydrocracking of coal and oil sand derived asphaltenes (Song et al., 1991). They concluded that as the pore diameter increases, heavier fractions (mostly the asphaltenes) are strongly adsorbed on the catalyst surface, inhibiting the adsorption of less heavier molecules. This conclusion was also supported by Diez et al. (1999), who showed that a HDT catalyst with large pores (> 14 nm) was more susceptible for asphaltene decomposition.

On the basis of the catalyst pore sizes (~5–20 nm) and HDT results, it can be suggested that an optimum pore diameter of approximately 10 nm was effective for both HDS and HDN of the HGO. For the HDS activity, a study conducted by Inoguchi et al. (1978) on the control of pore size of supports concluded that optimal pore diameter shifted from 10 nm for HDS of petroleum distillates to 15 nm for HDS of the residue. Furthermore, Fischer et al. (1986) reported that for residue HDS, a

small-pore catalyst (in the size range of 3–10 nm) was selective for non-asphaltene sulfur; while a large-pore catalyst (in the size range of 10–30 nm) was selective for asphaltene sulfur (Takeuchi, 1986). Thus, results obtained in the present study (as depicted in Figures 4.23 & 4.24) for HDS and HDN of heavy gas oil fractions are consistent with that reported in literature (Breivik et al., 1982).

4.3.3 Effects of temperature on sulfur and nitrogen conversion

An easy and cost-efficient way of increasing HDT conversions is by manipulating process temperature. However, an excessively high operating temperature may lead to activity loss and shortening of catalyst life (Gruia, 2006). Thus, the effects of temperature on sulfur and nitrogen conversions were studied. It is well known that during HDT reactions, rapid catalyst deactivation (or ageing) occurs due to sintering and coke formation on the catalyst surface (Speight, 2000). In order to maintain a stable catalyst activity and desired product quality, operating temperature is gradually raised to compensate for catalyst deactivation. Thus, the effect of temperature on the catalytic hydrotreatment of the heavy gas oil was evaluated using the four FeW/SBA-15 catalysts. The effect of temperature on nitrogen and sulfur conversions is presented in Figures 4.23 and 4.24, respectively.

In all phases of the study, temperature was varied from 375 to 400°C; while pressure, H_2 to oil ratio, and LHSV conditions were maintained at 8.8 MPa, 600 mL/mL and 1 h^{-1}, respectively. From the results compiled in Table 4.2, it is obvious that maximum HDS activity was observed at 400°C. It may be noted that the HDS activities for all catalysts increased with increasing temperature. However, in the case

of nitrogen conversion, the HDN activity showed a slight improvement with increased temperature for the set of catalysts studied in phase I of the project. Interestingly, the HDN activity for Cat-D (having the largest pore diameter) decreased with a temperature increase from 388 to 400°C. This may be explained by the fact that larger molecules (mostly consisting of asphaltenes) easily diffused into the larger pores of Cat-D as the reaction progressed. With increasing temperature, the asphaltene micelles undergo decomposition or mild hydrocracking; yielding products of lower molecular weight hydrocarbons, which are the major precursors for coke deposition. The coke formed tends to cover the active FeWS phase; thus preventing direct exposure of the active catalytic phase with other species present in the gas oil.

Furthermore, the effect of temperature on variable Fe and W metals loading were also studied and are discussed in the following subsection.

4.3.4 Optimization of metals loading for HGO hydrotreating

Catalyst metals optimization was important in order for the catalyst displaying optimum HDS and HDN activities to be produced. The loading of active metal (tungsten) was first optimized at a constant promoter loading of 2 wt. % Fe. These were carried out in phases II and III of the project. A total of five catalysts were prepared; three in phase II and two in phase III, respectively. The three different tungsten loadings investigated using the optimum pore diameter FeW/SBA-15 catalyst selected from phase I are as follows: 20, 30, and 45 wt.%. It should be noted that Fe loading was kept constant at 2.0 wt.% for all three catalysts screened and the optimum catalyst pore diameter was approximately 10 nm. Figures 4.23 and 4.24

show results of the HDS and HDN activities for these catalysts. It can be concluded from these results that Cat-F, with 30 wt.% W, yielded the optimum W-loading on the SBA-15 catalyst support.

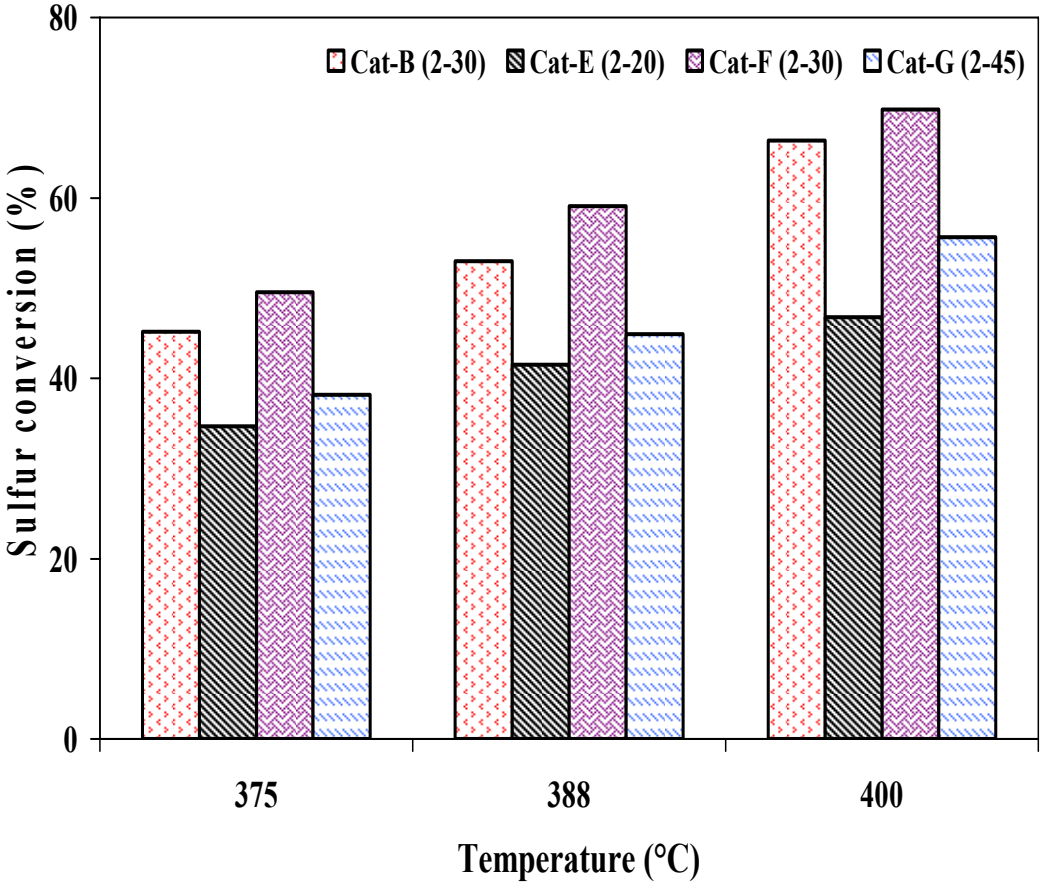

Figure 4.23: Effect of HDS activities of SBA-15-supported FeW catalysts as a function of variable tungsten loading at constant Fe loading of 2 wt.%. (Catalyst = 5 cm^3, P = 8.8 MPa, LHSV = 1 h^{-1} and H_2/oil ratio = 600 mL/mL).

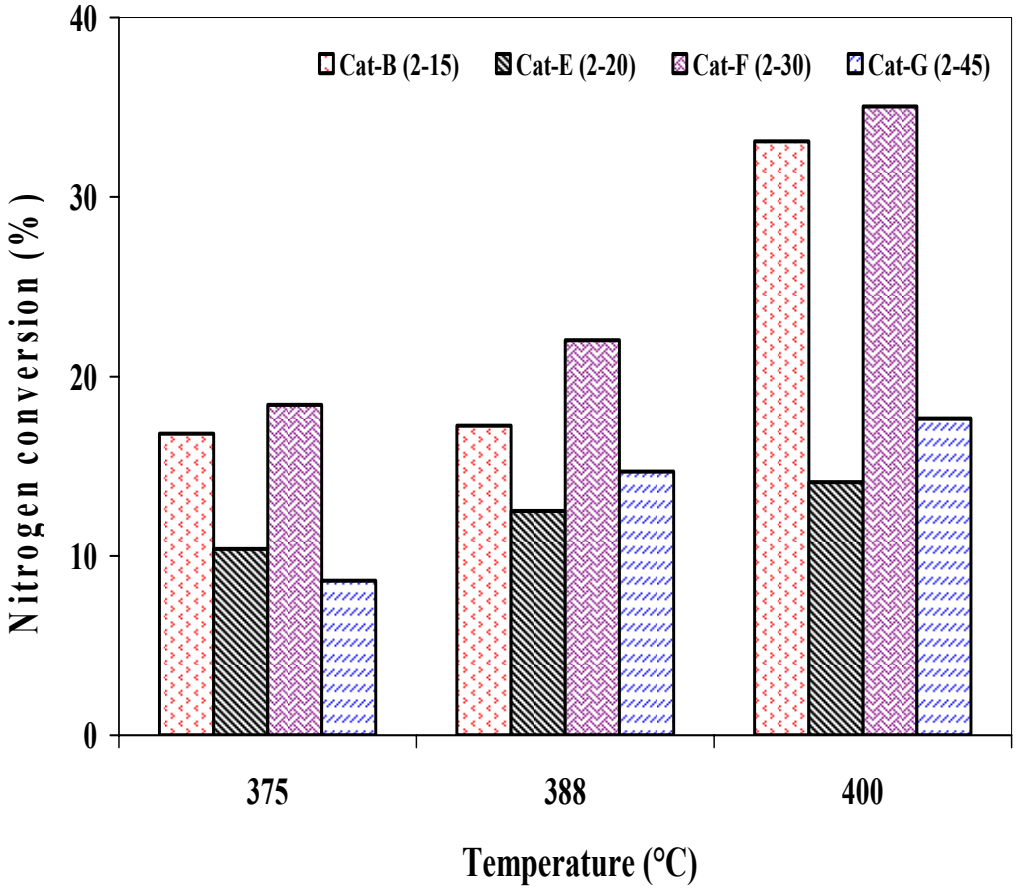

Figure 4.24: Effect of HDN activities of SBA-15-supported FeW catalysts as a function of variable tungsten loading at constant Fe loading of 2 wt.%. (Catalyst = 5 cm^3, P = 8.8 MPa, LHSV = 1 h^{-1} and H_2/oil ratio = 600 mL/mL).

On the basis of the optimum W-loading obtained from phase II, the Fe loading was also optimized at three different loadings (2, 3, and 5wt.% Fe), maintaining a constant tungsten loading of 30 wt.% on the optimum SBA-15 support. Figures 4.25 and 4.26 compare the steady-state HDS and HDN activities, respectively, for each of the three catalysts.

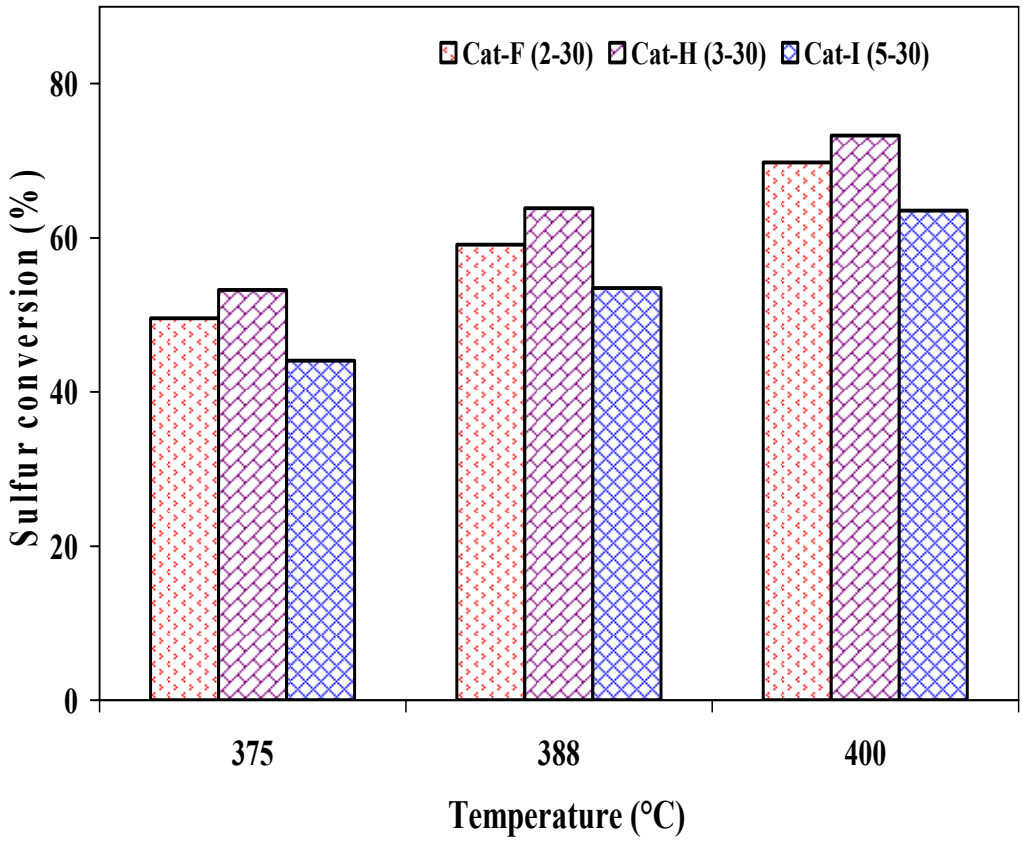

Figure 4.25: Effect of HDS activities of SBA-15-supported FeW catalysts as a function of variable iron loading at constant W loading of 30 wt.%. (Catalyst = 5 cm^3, P = 8.8 MPa, LHSV = 1 h^{-1} and H_2/oil ratio = 600 mL/mL).

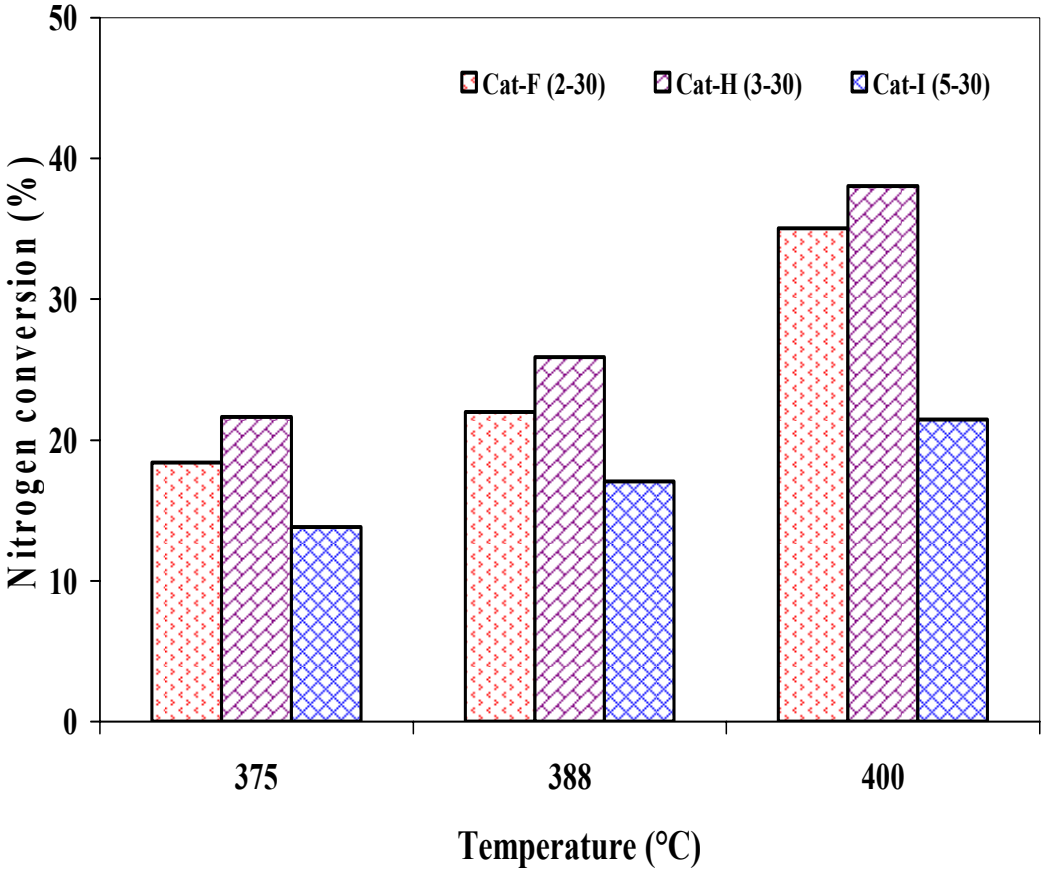

Figure 4.26: Effect of HDN activities of SBA-15-supported FeW catalysts as a function of variable iron loading at constant W loading of 30 wt.%. (Catalyst = 5 cm^3, P = 8.8 MPa, LHSV = 1 h^{-1} and H_2/oil ratio = 600 mL/mL).

It can be found from these figures 4.25 & 4.26 that increasing the Fe loading beyond 3.0 wt.% resulted in a decreased HDS and HDN activities of the SBA-15-supported FeW catalyst. This could be associated with the corresponding decrease in surface area with increased metal loadings. It was concluded that metal loadings of 3 wt.% Fe and 30 wt.% Mo were the optimum loadings for the best catalytic performance on the optimum pore diameter SBA-15 support. For descending reaction temperatures of 400, 388, and 375°C, this optimum catalyst produced sulfur conversions of 73.4, 64.1, and 52.9%, respectively, and nitrogen conversions of 38.3, 26.1, and 21.7%, respectively. In this regard, the optimum catalyst having pore diameter of 10 nm; with metal compositions of 3 wt.% Fe and 30 wt.% W, respectively was selected to carry out process parameters study. Results of such a study have been discussed in the following subsections.

4.4 Hydrotreating kinetics

4.4.1 Effect of process parameters variation with hydrotreating conversions

As we may know, the hydrotreating reaction is one of the major refining processes that has gained tremendous importance due to its wide application in refineries. As aforementioned, hydrotreating is the key upgrading process employed to reduce the sulfur and nitrogen contents in petroleum fractions so as to produce cleaner fuels, which meet product specifications. In this section, the effects of operating conditions on the removal of sulfur and nitrogen compounds are discussed in the ranges of temperatures, pressures, LHSV, and gas-to-oil ratios of 360-420^{o}C, 7.6-9.6 MPa, 0.5-2 h^{-1}, and 400-1000 mL/mL, respectively.

4.4.1.1 Effect of temperature

The significance of temperature in the HDT reactions has been discussed in section 6.2.3. However, for the purposes of kinetic studies, the effect of temperature has been studied by varying it from 360 to 420°C. The other process variables namely pressure, LHSV and hydrogen/heavy gas oil volumetric ratio were respectively constant at 8.8 MPa, 1.0 h^{-1} and 600 mL/mL during these experiments. The results shown in Figure 4.27 indicate that an increase in temperature favors the percent sulfur and nitrogen conversions as expected.

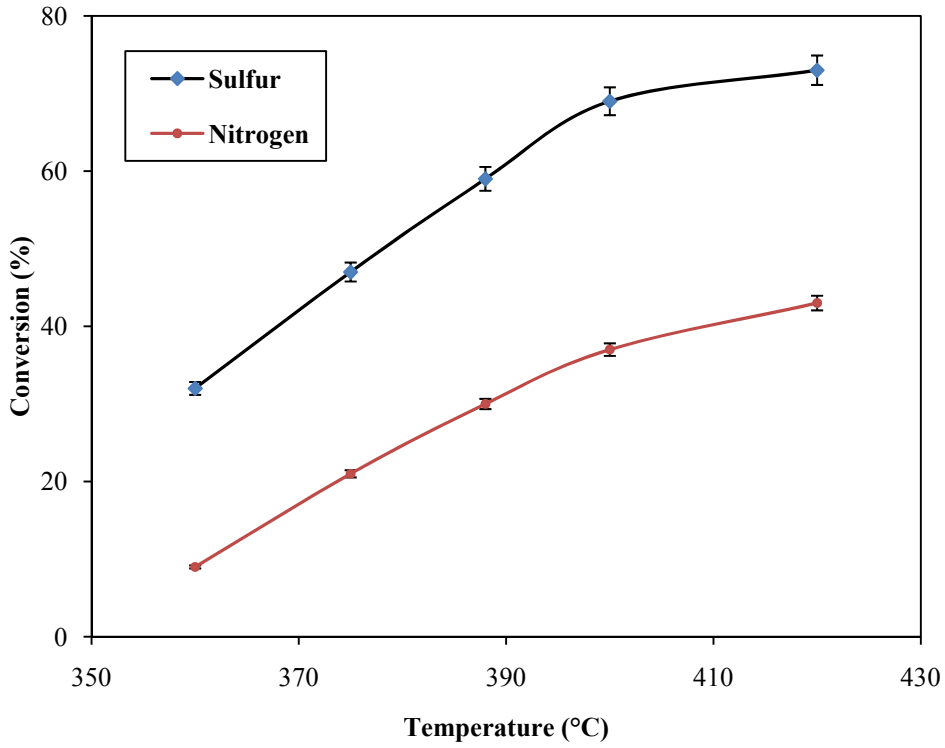

Figure 4.27: Effect of temperature on sulfur and nitrogen conversions. (Catalyst = 5 cm^3, T = 360-420ºC, P = 8.8 MPa, LHSV = 1 h^{-1} and H_2/oil ratio = 600 mL/mL)

However, the rate of increase in HDS and HDN tend to be slightly slow at higher temperature ranges as compared to that at lower temperature ranges. Thus, it can be observed from Figure 4.27 that a 20ºC rise in temperature from 400 to 420ºC only resulted in about 4 wt.% change in sulfur conversion. Hence, operating the HDT process at about 400°C, a maximum sulfur and nitrogen removal of about 73 and 38 wt.% could be achieved using the optimum FeW/SBA-15 catalyst. Experimental runs were repeated at 360, 375, 388, 400 and 420^{o}C and the results compared with those of the previous runs in order to ascertain the reproducibility of the data obtained. Results of the error analyses as presented in Figure 4.27 evidence the fact that the data are quite reproducible, especially at higher temperatures with only a narrow margin of error. In the case of sulfur, the highest error margin was $\pm$2.6 wt% whereas those of nitrogen gave an average maximum error of $\pm$1.2 wt%.

4.4.1.2 Effect of liquid hourly space velocity

The liquid hourly space velocity gives the hourly volumetric flow rate of liquid to the volume of catalyst in the reactor. Thus, the effect of liquid hourly space velocity (LHSV) on both sulfur and nitrogen conversions were studied by varying LHSV from 0.5 to 2.0 h^{-1} at a constant temperature of 388°C, pressure of 8.8 MPa and a hydrogen/heavy gas oil volumetric ratio of 600 mL/mL. Experimental results depicted in Figure 4.28 indicate that by decreasing the LHSV, the extent of sulfur and nitrogen conversions increased due to the fact that the contact time of the liquid with the catalyst increased. It could be concluded from the LHSV studies that at these

conditions about 77.4 and 43.6 wt.% sulfur and nitrogen, respectively could be achieved over the optimum FeW/SBA-15 catalyst.

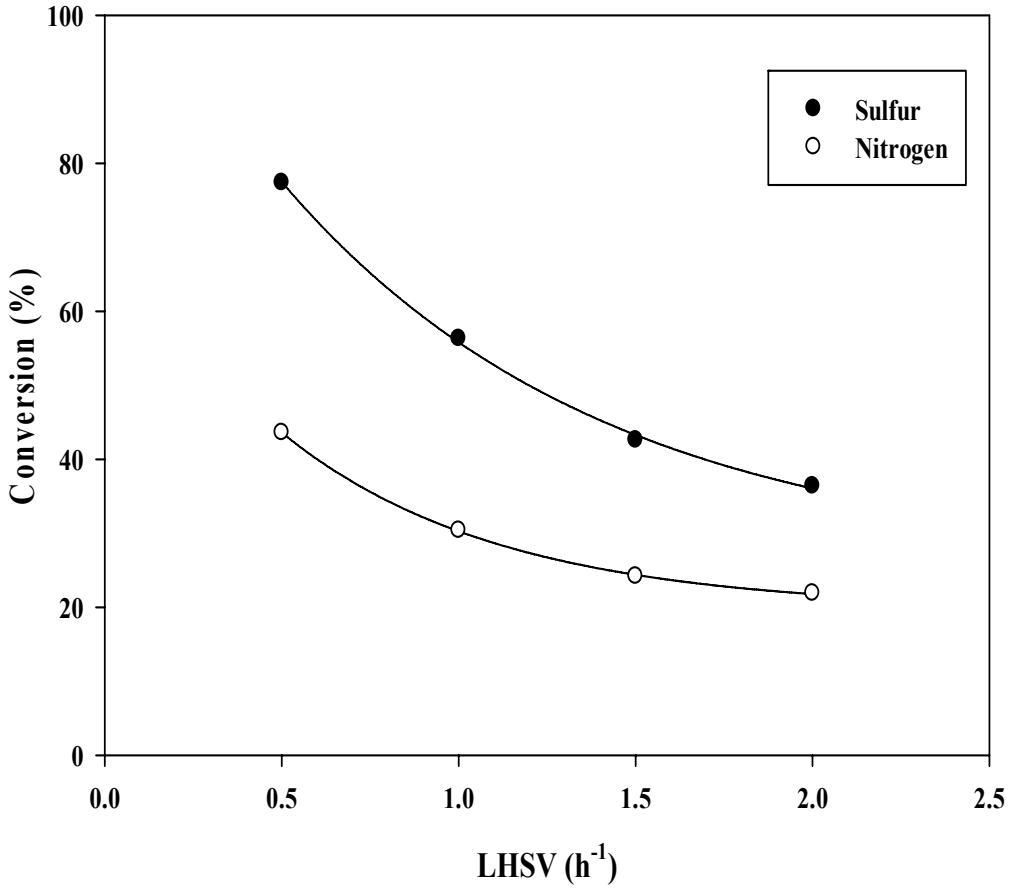

Figure 4.28: Effect of liquid hourly space velocity on sulfur and nitrogen conversions (Catalyst = 5 cm^3, T = 388°C, P = 8.8 MPa, LHSV = 0.5-2 h^{-1} and H_2/oil ratio = 600 mL/mL).

4.4.1.3 Effect of pressure

One crucial process parameter that directly affects the hydrotreating conversions is the hydrogen partial pressure. For instance, in the hydrotreating of naphtha feedstock, Topsoe et al. (1982) observed that below a certain hydrogen partial pressure, it becomes impossible to reduce the product nitrogen to levels required to be used as reformer feedstock even when the operating temperature is increased. As a result, the effect of pressure on the hydrotreating of heavy gas oil was studied at temperature, LHSV, and hydrogen-to-gas oil ratio of 388°C, 1 h^{-1}, and 600mL/mL, respectively, and is represented in Figure 4.29.

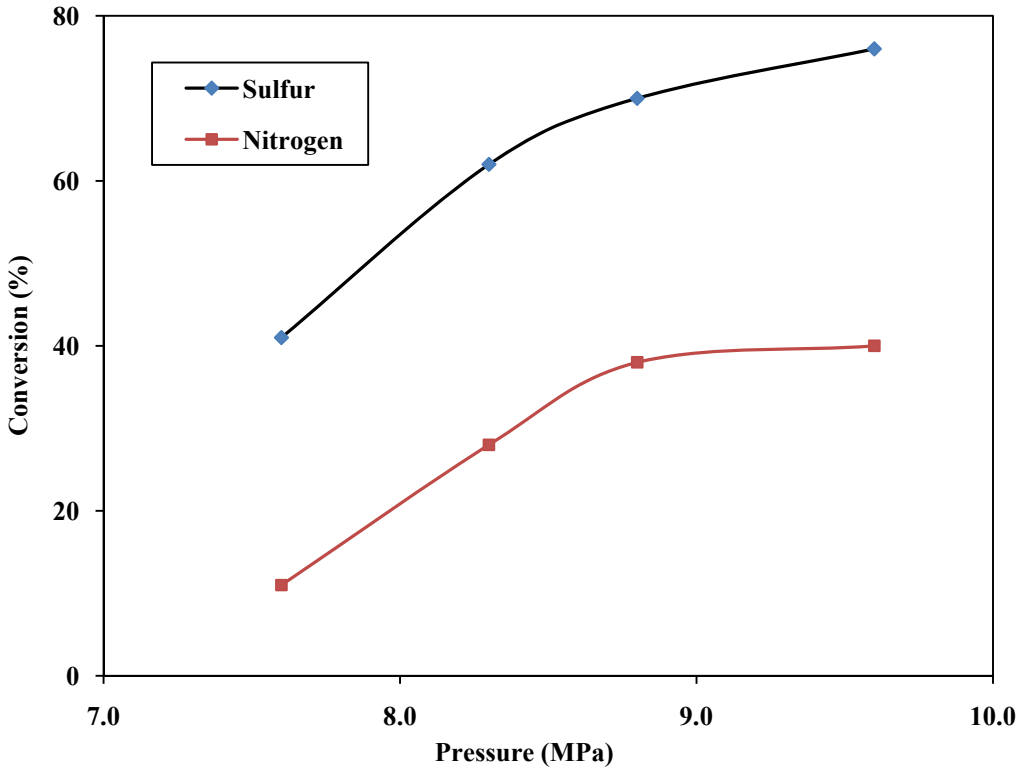

Figure 4.29: Effect of pressure on sulfur and nitrogen conversions (Catalyst = 5 cm^3, T = 388°C, P = 7.6-9.6 MPa, LHSV = 1 h^{-1} and H_2/oil ratio = 600 mL/mL).

As was expected, increasing the hydrogen partial pressure resulted in an increase in the extent of sulfur and nitrogen conversions through an increase in catalyst activity. It is known that the major role of the catalyst is to provide the required reaction interface for the reactants, thereby promoting interaction between the feedstock constituents (i.e. sulfur, nitrogen, etc.) and the hydrogen. However, it is noteworthy that excessively high hydrogen pressures may only serve to saturate the catalyst and any further increase in hydrogen partial pressure tend to affect the hydrotreating conversions only by a slight margin (Speight, 2000). For the optimized FeW/SBA-15 catalytic study, one could observe from Figure 4.29 that by increasing the hydrogen pressure from 9.0 to 9.7 MPa only resulted in less than 5 wt.% conversion in both HDS and HDN processes.

The nature of the HDS process is such that the rate will increase with increasing partial pressure of the hydrogen. However, Botchwey et al. (2003) concluded from their study on the inter-stage hydrogen sulfide removal in a two-stage hydrotreating of heavy gas oil that excessively increasing hydrogen pressure may result in relatively high concentrations of ammonia and hydrogen sulfide in the vicinity of the catalyst, which tends to have detrimental effect on catalyst activity.

4.4.1.4 Effect of hydrogen-to-heavy gas oil ratio

In any hydrotreating reaction, the choice of proper ratio of hydrogen/hydrocarbon is very crucial. Generally, an increase in the hydrogen partial pressure increases the rate of hydrogenation, which in turn increases the rate of removal of sulfur and nitrogen compounds. The use of higher hydrogen pressure also

enriches the catalyst and reduces deactivation. But a very high value of hydrogen/hydrocarbon ratio may increase the cost of the process. Thus, an optimum value of the hydrogen/hydrocarbon ratio is always desired. In the present study, the effect of hydrogen/heavy gas oil ratio on the HDS of heavy gas oil has been determined by varying it from 400 to 1000 mL/mL, maintaining temperature, pressure and LHSV at 388°C, 8.8 MPa and 1.0 h^{-1}, respectively.

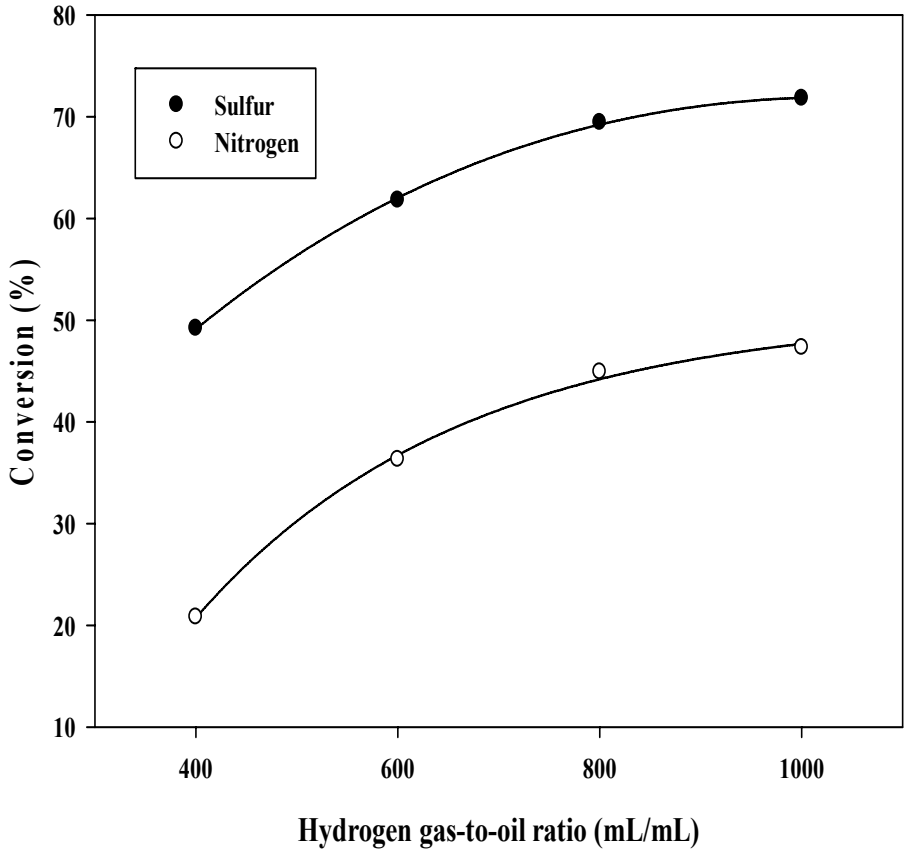

Figure 4.30: Effect of hydrogen gas-to-oil ratio on sulfur and nitrogen conversions (Catalyst = 5 cm^3, T = 388ºC, P = 8.8 MPa, LHSV = 1 h^{-1} and H_2/oil ratio =400-600 mL/mL).

It can be observed from the Figure 4.30 that the removal of sulfur and nitrogen compounds increased significantly as the hydrogen-to-heavy gas oil volumetric ratio is increased up to 800 mL/mL. However, the effect began to level off beyond this threshold, rendering further increments economically non-beneficial to the process. This observation was explained by Bej et al. (2002) to be due to the pseudo-first order dependency of the rates of HDS and HDN reactions on hydrogen partial pressure at its high value corresponding to a hydrogen/heavy gas ratio of 800 mL/mL. Thus, the present study indicates that a hydrogen/heavy gas oil ratio of about 800 mL/mL should be kept for achieving maximum sulfur and nitrogen removal.

4.4.2 Kinetic parameters evaluation by different models

As previously discussed in section 2.5, kinetic parameters evaluation and modeling for the hydrodesulfurization and hydrodenitrogenation reactions are normally derived using the power law and the Langmuir-Hinshelwood models. In this study, both the power law and Langmuir-Hinshelwood models were employed in the kinetic analyses. In cases whereby inhibition of other compounds was disregarded, the power law model was employed for the kinetic parameters evaluation. However, in the scenarios in inhibitive compounds such as hydrogen, hydrogen sulfide removal, etc., were considered, the Langmuir-Hinshelwood model was regarded appropriate in kinetic parameters evaluation. Another useful model of industrial importance studied was the Multi-parameter model. Detailed discussions of kinetic results obtained are addressed in the subsections that follow and compared with those found in the open literature.

4.4.2.1 The Power Law Model

The power law model is mostly used by many researchers in studies of kinetics modeling of HDS and HDN due to its simplicity. In this work, the reaction orders for the HDS and HDN were determined by the power law model and the results are summarized in Table 4.4.

Table 4.4: Determination of reaction orders by the PL model using their regression coefficients.

Equation #	Order of reaction (n)	Kinetic Equations	Value of R^2	
			HDS	HDN
1	0.0	$k = [C_F - C_P]*LHSV$	0.9907	0.9644
2	0.5	$k = 2\,[C_P^{0.5} - C_F^{0.5}]*LHSV$	0.9797	0.9937
3	1.0	$k = \ln [C_F - C_P]*LHSV$	0.9905	0.9961
4	1.5	$k = 2\,[1/C_P^{0.5} - 1/C_F^{0.5}]*LHSV$	0.9968	**0.9987**
5	2.0	$k = [1/C_P - 1/C_F]*LHSV$	**0.9992**	0.9977
6	2.5	$k = 0.667\,[1/C_P^{1.5} - 1/C_F^{1.5}]*LHSV$	0.9983	0.9971
7	3.0	$k = 0.50\,[1/C_P^{2} - 1/C_F^{2}]*LHSV$	0.9947	0.9968

The values of reaction orders were determined from the best fit of experimental data. Using the general solution for the n^{th} order kinetic equation developed for the Power Law model (Eq. 2.18 in section 2.4.1), a trial and error approach was adopted by varying the value of *n* until the highest regression

coefficient, R^2, was obtained. Values of R^2 obtained from the fitting of these equations to experimental data can also be found in Table 4.4. R^2 is generally regarded as a statistical measure of fitness; the closer it is to unity, the better is the fitness. From the different values of n tested, the appropriate value of n for the HDS and HDN reactions were selected to be those with the highest R^2 values. Thus, HDS follows a 2^{nd} order, whereas HDN follows a 1.5^{th} order. The fitting of rate data for equations having the aforementioned orders of reaction is represented in Figure 4.31. Hence, the rate constants for different temperatures were calculated using Eqs. (4 and 5) for HDN and HDS, respectively (as given in Table 4.4).

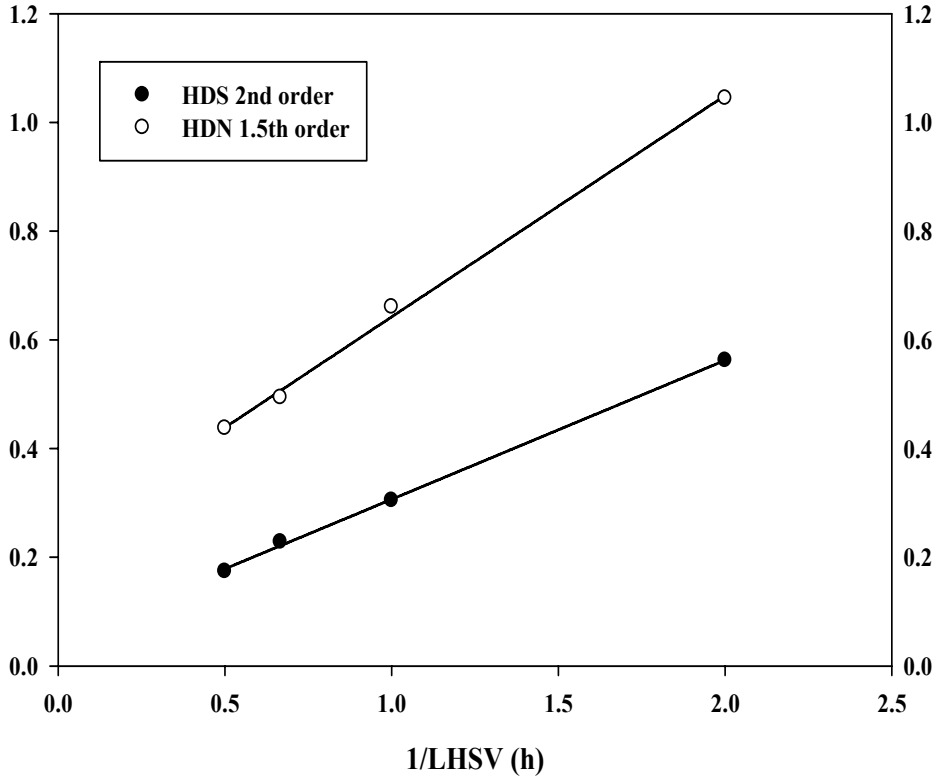

Figure 4.31: Fitting of experimental data to the P-L model having orders 1.5 and 2.0 for HDN and HDS, respectively. (Catalyst = 5 cm^3, T = 388ºC, P = 8.8 MPa, LHSV = 0.5-2 h^{-1} and H_2/oil ratio = 600 mL/mL).

To determine the activation energies and pre-exponential factors for the HDS and HDN reactions, a plot of *lnk* against *1/T* was computed and represented in a graph as shown in Figure 4.32.

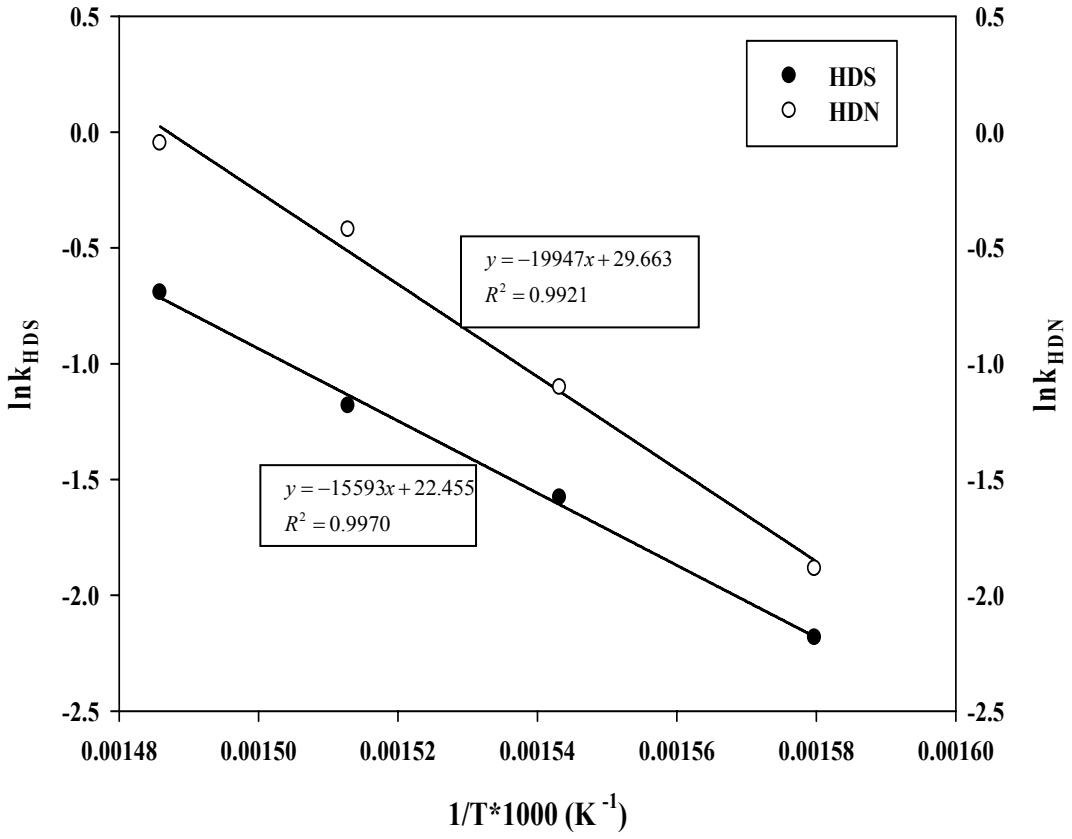

Figure 4.32: Arrhenius plot of HDS and HDN rate constants obtained from the Power Law model. (Catalyst = 5 cm^3, T = 360-420 ºC, P = 8.8 MPa, LHSV = 1 h^{-1} and H_2/oil ratio = 600 mL/mL).

These parameters were determined from the Arrhenius plot for the rate constants. From this plot, the activation energies computed within the range of temperatures studied (375 – 420ºC) for HDS and HDN were found to be 129.6 and 165.8 kJ/mol, respectively. The pre-exponential factors computed from the intercept on the *lnk* axis were found to be 4.18E +10 and 7.63E +12 for HDS and HDN, respectively. However, discrepancies in activation energy may indicate a change in mechanism of reaction or interference of a physical phenomenon such as diffusion (Ferdous et al., 2006), which tends to decrease the activation energy as a result of inherent mass transfer limitations in packed beds. This mass transfer effect on hydrotreating reactions in trickle bed reactors will be discussed in subsequent subsections.

4.4.2.2 The Langmuir-Hinshelwood Model

For the Langmuir-Hinshelwood model, both HDS and HDN reactions were assumed to be irreversible (Chu et al., 1989; Whirsthurst et al., 1998). The L-H type of rate equation for representing the hydrogenation kinetics of industrial feedstocks is complicated; and the fact that too many coefficients are involved to be determined makes it quite a challenging task to undertake. However, attempts have been made to determine the parameters by employing a simplified model described by Botchwey et al. (2003), and can be seen equations 2.21 and 2.22.

Excel solver was used to solve eq. 2.21. The values of k_i, K_i, K_{H2}, and K_{H2S} were obtained by rigorous iterative procedure. The calculated parameters for HDS and HDN are given in Table 4.4. The values of calculated C_i predicted by the model were

in agreement with those obtained from experimental data used. It is observed from this table that k_S and k_N increased with the increase in temperature; i.e., the rates of HDS and HDN increased with the increase in temperature.

Table 4.5: Calculated values of k_S, k_N, K_N, K_S, and K_{H2S} from the L-H model

HDN Reaction

T (K)	k_N	K_N	K_{H2}	K_{H2S}
633.15	0.15	1.62	1.67	105.01
648.15	0.35	1.48	1.55	98.75
661.15	0.73	1.40	1.48	92.50
673.15	1.05	1.31	1.40	86.25
693.15	1.67	0.97	1.16	78.00

HDS Reaction

T (K)	Ks	Ks	K_{H2}	K_{H2S}
633.15	0.15	4.77	2.77	105.01
648.15	0.42	4.00	2.40	98.50
661.15	0.72	3.32	2.06	92.00
673.15	1.19	2.62	1.75	85.00
693.15	1.80	2.00	1.50	78.00

Moreover, figures 4.33 and 4.34 show that K_{H2S}, K_{H2}, K_S, and K_N decreased with the increase in temperature. This trend indicates that increase in temperature decreased the inhibition of these parameters on HDN and HDS reactions. The activation energies from this model were calculated from the Arrhenius plot in Figure 35. The activation energies for HDN and HDS reactions were 150.6 and 147.2 kJ/mol, respectively.

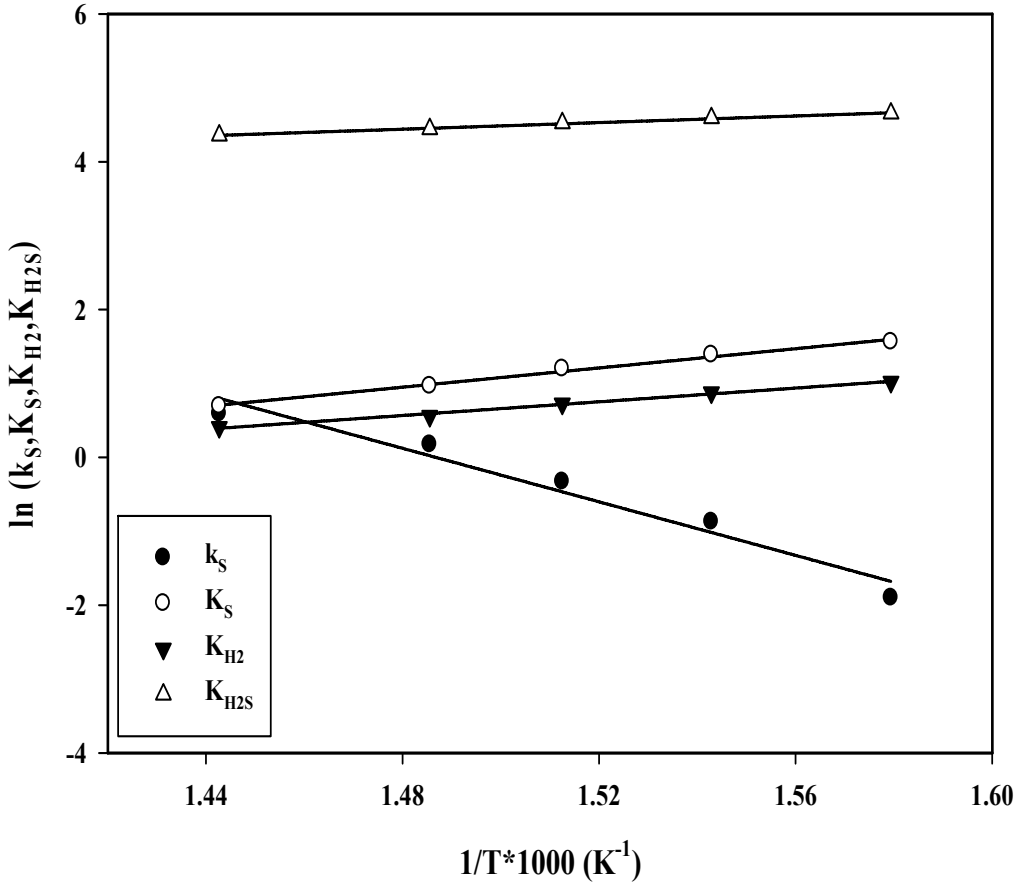

Figure 4.33: Plots of constants: k_S, K_S, K_{H2}, and K_{H2S} from the L-H Model for HDS reaction. (Catalyst = 5 cm^3, T = 360-420 ºC, P = 8.8 MPa, LHSV = 1 h^{-1} and H_2/oil ratio = 600 mL/mL).

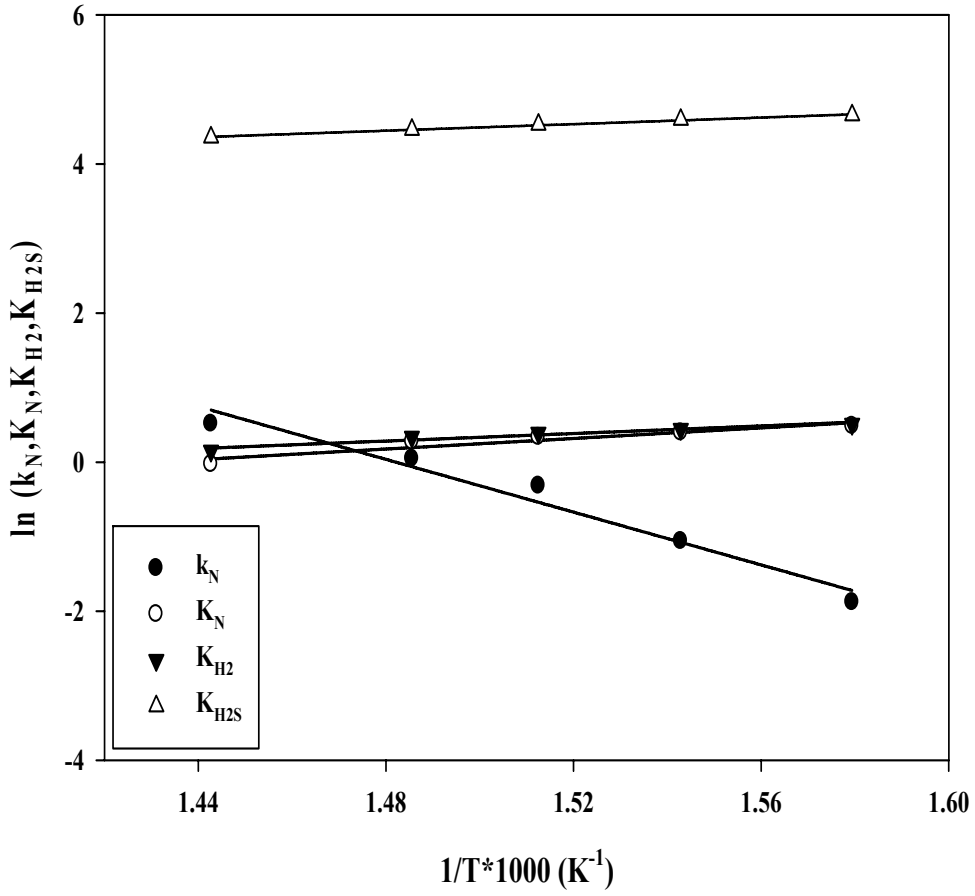

Figure 4.34: Plots of constants: k_N, K_N, K_{H2}, and K_{H2S} from the L-H Model for HDS reaction (Catalyst = 5 cm^3, T = 360-420 ºC, P = 8.8 MPa, LHSV = 1 h^{-1} and H_2/oil ratio = 600 mL/mL).

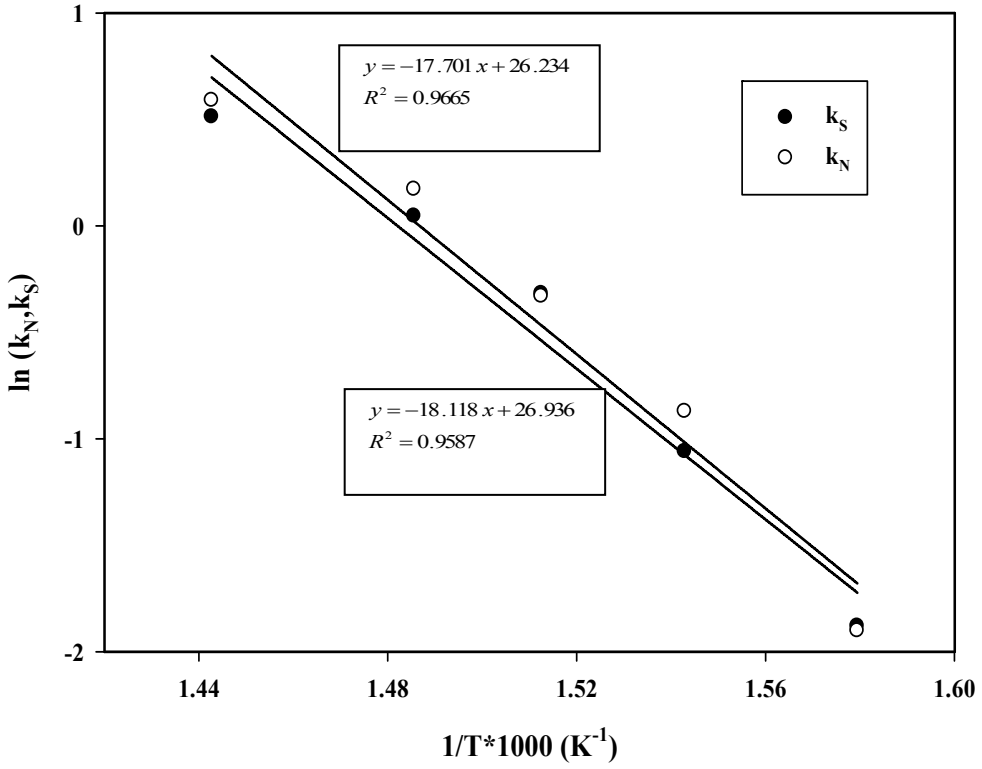

Figure 4.35: Arrhenius plot of HDS and HDN rate constants obtained from the Langmuir-Hinshelwood model. (Catalyst = 5 cm^3, T = 360-420 ºC, P = 8.8 MPa, LHSV = 1 h^{-1} and H_2/oil ratio = 600 mL/mL).

4.4.2.3 The Multi-parameter Model

Kinetic parameters predicted for the HDS and HDN reactions by the multi-parameter model are compiled in Table 4.6.

Table 4.6: Multi-parameter model results for HDS and HDN reactions

Parameter	HDS	HDN
n	2.2	1.8
k	722	12.73
s	1.52×10^3	1.43×10^3
m	3.39	4.18
q	1.19	1.54
c	0.92	0.67
R^2	0.96	0.88
R^2adj	0.94	0.83

Experimental data for the optimized catalyst was analyzed using the non-linear regression method in Polymath 5.1 software under extended experimental conditions of temperatures, pressures, LHSVs, and gas/oil ratios of 360 to 420°C, 7 to 10 MPa, 0.5 to $2h^{-1}$, and 400 to 1000 mL/mL, respectively. The activation energies for HDS and HDN reactions were computed to be 126.7 kJ/mol and 118.8 kJ/mol, with predicted reaction orders of 2.2 and 1.8, respectively. R^2 for HDS and HDN were 0.96

and 0.88, respectively. The value of R^2 adjusted tells how well the model could be used to predict sulfur and nitrogen product distributions under conditions not experimented, and were found to be 0.94 and 0.83, respectively.

4.4.3 Comparison of results from the various models studied

Table 4.6 compiles the activation energies and Arrhenius constants obtained from the PL, L-H, and MP models. It can be observed from this table that for HDN and HDS reactions activation energies from the Langmuir-Hinshelwood model are higher than those from the power law model. This could be due to the fact that in the Langmuir-Hinshelwood model adsorption of sulfur, nitrogen, hydrogen, and H_2S were considered. Also, in this model it was assumed that H_2S inhibits HDN and HDS reactions (Botchwey, 2003). Higher activation energies for HDN and HDS reactions from the L-H model than that from the power law model indicate that nitrogen and H_2S adsorptions have significant inhibition effects on HDN and HDS. H_2S competes with the organosulfur and organonitrogen compounds for the same active catalyst sites in the reaction process (Whitehurst et al., 1998), which in turn reduce HDN and HDS activities of the catalyst and hence increase activation energies.

Table 4.6: Comparison of the PL, LH, and MP models

	PL model			LH model			MP model		
	n	**E_a† (kJ/mol)**	**k_o***	**n**	**E_a† (kJ/mol)**	**k_o***	**n**	**E_a† (kJ/mol)**	**k_o***
HDS	2.0	129.6	$4.18E^{10}$	Pseudo	147.2	$2.47E^{11}$	2.2	126.7	722
HDN	1.5	165.8	$7.63E^{12}$	Pseudo	150.6	$4.99E^{11}$	1.8	118.8	12.73

† Activation energy * Pre-exponential factor

4.5 Stability Study for the Optimum FeW/SBA-15 Catalyst

Catalyst stability test was performed on the optimum FeW/SBA-15 catalyst in the final phase of the project. As described for the normal hydrotreating runs, liquid hydrotreated samples were collected every 24 hours, stripped with nitrogen gas and analyzed for sulfur and nitrogen over the 60-day period planned for the study. The average steady-state conversions of sulfur and nitrogen were determined prior to a five day pre-coking period for the catalyst so as to attain a steady-state condition. Figure 4.36 shows the results of the stability study. It can be noted from the sulfur and nitrogen conversion profiles that the optimum FeW/SBA-15 catalyst displayed steady-state conversions of 62% for sulfur compounds 25% for nitrogen compounds; with average error margins of ± 1 wt%, in both sulfur and nitrogen conversion, respectively. One can deduce from the long-term stability study that the optimum FeW/SBA-15 did not suffer any significant deactivation over the 60-day period of study.

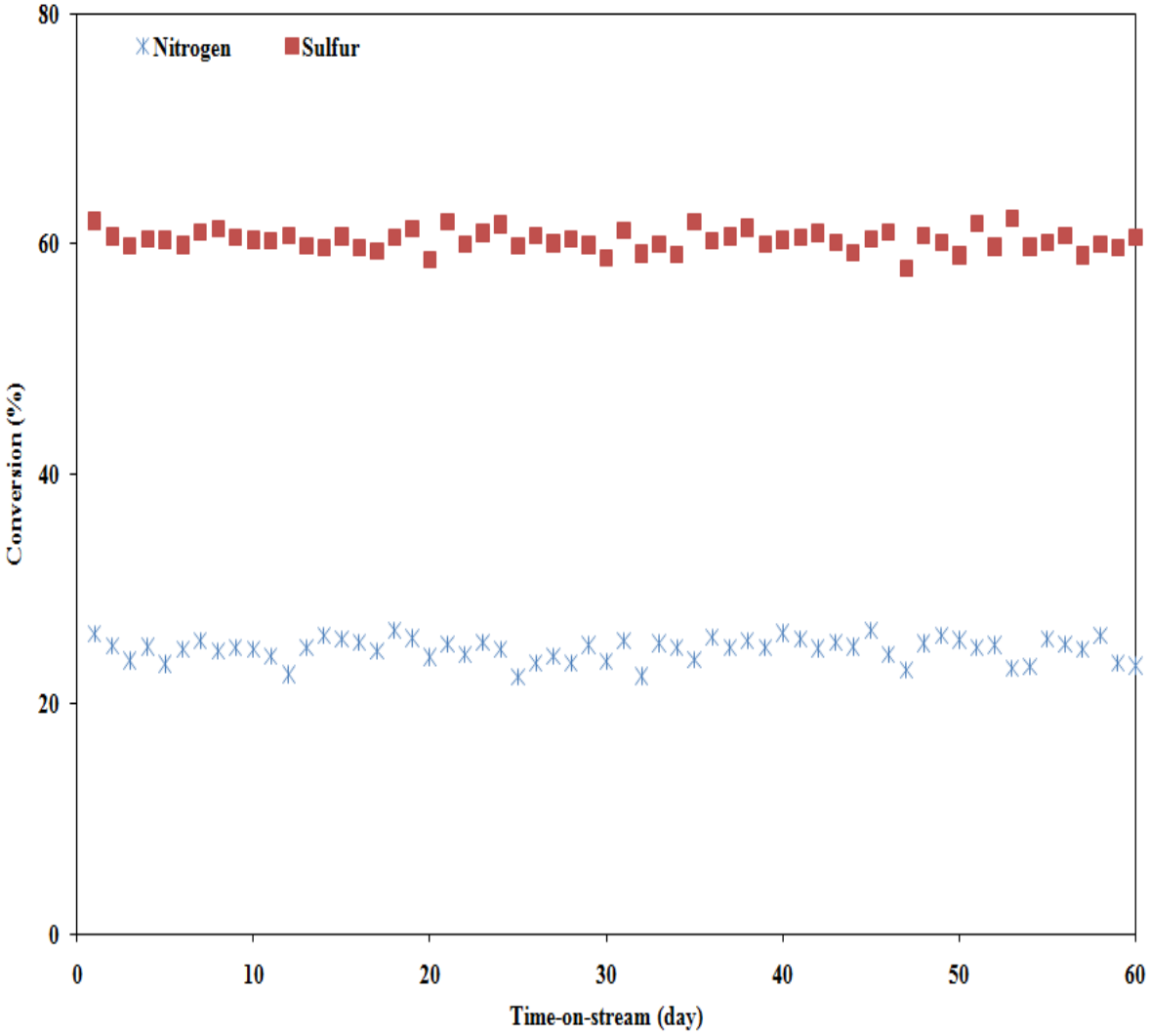

Figure 4.36: HDS and HDN steady-state activities over a 60-day period of stability study of the optimum FeW/SBA-15 catalyst using HGO (LHSV = 1.0 h^{-1}; P = 8.8 MPa; T = 388°C; H_2/HGO = 600mL/mL; catalyst loading = 5mL).

4.6 Mass Transfer Resistances for the HDS/HDN Reactions

It was important to evaluate the mass transfer resistances associated with the hydrotreatment process using the optimum FeW/SBA-15 catalyst produced. This was deemed necessary due to their effect on the overall results collected from kinetic analysis. The two main evaluation approaches adapted include: (1) external mass transfer, consisting of the diffusion of H_2 (gas phase) into the HGO (liquid phase) exterior to the catalyst particles, and; (2) internal mass transfer, consisting of the diffusion of the organic sulfur and nitrogen compounds within the interior pores of the catalyst particles to reach the active sites. Appendices D and E give a detailed summary of these mass transfer analyses.

For the evaluation of the external mass transfer resistance, a criterion developed Charles N. Satterfield (1969) was adapted basically to determine which of the overall hydrotreating reactions represents the rate determining step. This was accomplished by finding whether the rate of hydrogen conversion in the HDN and HDS reactions or the rate of hydrogen mass transfer through the HGO liquid phase to the catalyst surface is significant. The summary of results and the possible ranges of reaction conditions to be considered from this analysis can be found in Table D.1 of Appendix D. It can be seen from each reaction condition studied that the left side of Satterfield's criterion for both reactions ($\mathbf{S_{HDS}}$ and $\mathbf{S_{HDN}}$) had the same magnitude (10^{-4}) as the overall mass transfer coefficient for hydrogen gas. The values of $\mathbf{S_{HDN}}$ validated Satterfield's criterion for all reaction conditions, while all values of $\mathbf{S_{HDS}}$ did not. This result suggests that mass transfer of heteroatomic compounds from the gas

phase to the catalyst surface can be ignored for the overall hydrodesulfurization reaction; but not for the overall hydrodenitrogenation reaction. This could be explained due to the higher consumption of H_2 for the HDN reaction. Furthermore, the HDN mechanism favors the pathway of initial pre-hydrogenation of olefinic bonds prior to the C-N bond cleavage, which probably accounted for the relatively higher hydrogen consumption as compared to the HDS reaction. Under the primary conditions shown in Table D.1 (T = 388°C; P = 8.8 MPa; LHSV = 1.0 h^{-1}), the rate of hydrogen consumption for the HDN reaction is 3.5 times more than that for the HDS reaction. Thus, the bulk mass transfer limitations for the overall HDS process can be considered not significant; however, that for the HDN reaction cannot be ignored. The higher hydrogen requirement for the HDN reaction could also be attributable to the rather high concentration of refractory nitrogen compounds (0.32 wt. %) present in the heavy gas oil analyzed. One can conclude from this result that the determined apparent reaction rates in the kinetic study will tend to be more sensitive toward a specific set reaction conditions studied than the intrinsic rates of the reactions.

Evaluation of the internal mass transfer limitations for the operation of the optimum FeW/SBA-15 catalyst during the hydrotreating process involved the validation of assuming isothermality across entire surface of the FeW/SBA-15 catalyst pellet. This was achieved via two approaches: (1) finding the highest potential temperature rise between the core and surface of the pellet (Fogler, 2006), and; (2) by the confirmation of Anderson's criterion (1963). Pertinent results spanning the range of conditions studied are summarized in Table E.1 of Appendix E.

For isothermality to be assumed, the calculated highest temperature difference between the center and surface of the catalyst pellets (ΔT_{MAX}) should not exceed 0.05 K. The ΔT_{MAX} obtained from computation was 0.018 K (i.e. calculated $\Delta T_{MAX} < 0.05$ K); hence the assumption of isothermality seems justifiable. Moreover, computation of the Anderson's criterion also gives a corroborative validation to the assumption of isothermality. Hence, the computed left-side of the Anderson's criterion was found to be far less than the right-side for both HDS and HDN reactions; giving a reasonable indication of the isothermal behavior of the FeW/SBA-15 catalyst.

For a given catalyst in operation, the ratio of the actual overall reaction rate with respect to the maximum potential reaction rate (i.e. if the internal catalyst surfaces were exposed to the conditions of the external catalyst surfaces) is termed the effectiveness factor. This parameter is typically determined by first determining the dimensionless Thiele modulus. If the Thiele modulus is large ($\Phi > 3$) and effectiveness factor is less ($\eta < 0.3$), the internal diffusion limits the rate of the reaction. Nonetheless, it is necessary to determine the Thiele modulus regarding the intrinsic reaction rates. It is often difficult to determine these intrinsic reaction rates, especially with the external mass transfer resistances that were found for the given reaction system. To overcome this obstacle, an alternative dimensionless modulus (Satterfield, 1970) defined by the overall reaction rate was determined as a means of estimating the effectiveness factor for each of the examined operating conditions. The bulk diffusivities of sulfur and nitrogen compounds were assumed to be the same as all compounds in the HGO feedstock. Regarding the internal mass transfer resistance,

only organosulfur and organonitrogen diffusion were considered since their HGO diffusivities were found to be $\times 10^{-1}$ lower in magnitude compared to H_2 diffusion in HGO.

The modulus (Φ) and effectiveness factor (η) were determined at both the inlet and outlet of the trickle bed reactor. The results are tabulated in Tables E.2 and E.3 for the HDS and HDN reactions, respectively. The inlet and outlet value ranges of Φ for HDS were 0.926-0.188 and 0.545-1.995, respectively. These modulus values corresponded to average effectiveness factors for the HDS reaction of 0.896 at the inlet and 0.837 at the outlet. For the HDN reaction, inlet and outlet modulus ranges of 0.072-0.613 and 0.522-0.981, respectively, were found. The average effectiveness factors found from these HDN modulus values were 0.867 and 0.740 for the reactor inlet and outlet, respectively. The high effectiveness factor values found give an indication that the HDS/HDN reactions are beyond first-order rate laws and that these results should be interpreted with caution. These results appear to be consistent with both HDN and HDS reaction orders predicted to be 1.5 and 2.0 (by the power law), and 1.8 and 2.2 (by the multi-parameter model), respectively. The observed trends were expected as the inlet factor values were controlled by the LHSV and the outlet factor values were controlled by the reaction temperature. Lower space velocities (due to higher contact time with the catalyst) resulted in higher η inlet values, while lower reaction temperatures resulted in higher η outlet values. The lower values at the outlet of the reactor reflect the fact that the diffusion limitations in the catalyst pellets are more noticeable at lower impurity concentrations. The internal mass transfer

resistances appeared to have a greater impact on the HDN reaction than on the HDS reaction, as the average effectives factor values for nitrogen removal dropped significantly from the inlet to the outlet (i.e., 0.896-0.873 for HDS as compared to 0.867-0.740 for HDN). In conclusion, the rate of the HDN reaction is governed by the rate of diffusion much more significantly than the HDS reaction.

5.0 CONCLUSIONS AND RECOMMENDATIONS

5.1 Conclusions

The prime objective of the study was to evaluate the hydrotreatment performance of SBA-15-supported FeW catalysts using heavy gas oil derived from Athabasca bitumen. Of crucial importance in this study was to explore the potential applicability of different pore diameters of the FeW/SBA-15 catalysts and also their sulfur and nitrogen conversions as a function of variable metals loading. Discussed below are some of the key conclusions reached in the various phases of the project:

- **Part 1: Variable pore diameter SBA-15 supports and characterizations**

SBA-15 supports of variable pore diameters were successfully synthesized using hexane as a micelle expander under acidic conditions. This was made possible by varying the molar ratio of hexane to ammonium fluoride in the synthesis medium in the 60-180 range. Specifically, SBA-15 support with textural properties of 474 m^2/g BET surface area, 1.09 cm^3/g pore volume, and 19.6 nm BJH pore diameter was found as the maximum pore diameter produced.

- **Part 2: Catalytic tests of variable pore diameter FeW/SBA-15 catalysts**

The catalytic performance tests using the four FeW/SBA-15 catalysts of variable pore diameters but similar metals loading (2 wt.% Fe and 15 wt.% W) resulted in catalyst with pore diameter of 10 nm as the optimum. At evaluated reaction temperatures of 400°C, 388°C, and 375°C, respectively, the hydrotreating

activities recorded for such a catalyst (Cat-B) were 66%, 53%, and 45% for HDS and 33%, 17%, and 17% for HDN reactions.

- **Part 3: Catalyst performance optimization and characterization**

Using the optimum catalyst support, the optimum Fe and W loadings as used in the preparation of the optimum catalyst (Cat-H) were found to be 3.0 and 30.0 weight percent, respectively. Catalytic performance test using HGO over this optimum catalyst gave rise to maximum hydrotreating activities of 73%, 64%, and 53% for HDS and 38%, 26%, and 22% for HDN at reaction temperatures of 400°C, 388°C, and 375°C, respectively. An equal mass loading of commercial γ-Al_2O_3–supported FeW catalyst offered HDS conversions of 84%, 71%, and 52% with HDN conversions of 42%, 27%, and 12% at the same temperatures of study.

- **Part 4: Kinetic parameter determination for optimum FeW/SBA-15 catalyst**

From kinetic study, power law models were fitted for the HDS and HDN reactions, with reaction orders of 2.0 and 1.5, respectively, and activation energies of 161 kJ/mol and 82.3 kJ/mol, respectively. By fitting the multi-parameter model to the kinetic data yielded HDS and HDN reactions orders of 2.2 and 1.8, with respective activation energies of 126.7 kJ/mol and 118.8 kJ/mol.

- **Part 5: Stability study for optimum FeW/SBA-15 catalyst**

Long-term deactivation studies conducted on the optimum FeW/SBA-15 catalyst, spanning a 60-day period, displayed steady-state conversions of 62% for sulfur and 25% for nitrogen.

5.2 Recommendations

After sequential studies regarding the applicability of FeW/SBA-15 catalyst for the hydrotreatment heavy gas oil derived from Athabasca bitumen, the following recommendations can be advanced for future studies.

- Even though SBA-15 material posses desirable textural properties making it a choice candidate for catalyst support, its poor surface chemistry contributed to its lesser HDS and HDN activities as compared to the commercial γ-Al_2O_3 counterpart. Enhancement of surface properties of the SBA-15 support via treatment that will enhance the production of surface silanol groups for anchorage can be explored to improve the surface chemistry. Effects of acid treatment with sulfuric acid or phosphoric acid may be investigated.
- Due to the known difficulty of sulfidation associated with W as the active component in the FeW/SBA-15 catalytic system, the effect of different sulfidation temperatures can be investigated to ascertain a desirable sulfidation temperature for such a catalyst. Also, it would be interesting to study the FeMo/SBA-15 catalyst, since the reduction temperature for molybdate species is less that polytungstate species; thus the extent of catalyst sulfidation at the prevailing sulfidation conditions is likely to be greater for the former catalyst (FeMo/SBA-15) as compared to the latter (FeW/SBA-15).
- Due to time constraint, the focus of the project was solely on using Fe as the promoter for the W/SBA-15 catalyst system. However, the effect of different promoters such as Ni and Co viz the formation different SBA-15 supported

bimetallic sulfide (NiWS and CoWS) hydrotreating catalysts could be explored to ascertain how the individual catalysts perform.

- The effects of incorporating tertiary promoters such as boron and phosphorus to the bimetallic FeW/SBA-15 catalyst system have the potential of improving its hydrotreating performance.

6.0 LIST OF REFERENCES

Ancheyta J., Angeles M.J., Macias M.J., Marroquin G., Morales R., "Changes in apparent reaction order and activation energy in the hydrodesulfurization of real feedstocks", Energy and Fuels, 189-193, 16, 2002

Aoyagi K., McCaffrey W.C., Gray M.R., "Kinetics of hydrocracking and hydrotreating of coker and oilsands gas oils", Petroleum Science and Technology, 997-1015, 21, 2003

Baldi, G., "Heat transfer in fixed bed three phase reactors, in: A. Gianetto, P.L. Silveston (Eds.), Multiphase Chemical Reactors", Hemisphere, New York, 1986.

Bartholdy, J., Cooper, B., Prepr. - Am. Chem. Soc., Div. Pet. Chem. 38, 2, 386–390, 1993

Bej, S.K.; Dalai, A.K.; Maity, S.K., "Effect of diluent size on the performance of a micro-scale fixed bed multiphase reactor in up flow and down flow modes of operation" Catalysis Today, 64, 333–345, 2001

Bej, S.K., Dalai, A.K., Adjaye, J., "Kinetics of Hydrodesulfurization of Heavy Gas Oil Derived From Oil-Sands Bitumen", Petroleum Science & Technology, 20, 867–877, 2002

Besenbacher F., Brorson M., Clausen B.S., Helveg S., Hinnemann B., Kibsgaard J., Lauritsen J.V., Moses P.G., Nørshov J.K., Topsøe H., "Recent STM, DFT, and HAADF-STEM studies of sulfide-based hydrotreating catalysts: Insight into mechanistic, structural and particle size effects", Catalysis Today, 86-96, 130, 2008

Biardi, G., Baldi, G., "Three-phase catalytic reactors", Catal. Today, 52, 223–234, 1999

Blin, J.L., and Su, B.L., "Tailoring pore size of ordered mesoporous silicas using one or two organic auxiliaries as expanders" Langmuir, 18, 5303-5308, 2002

Botchwey, C., "Two-stage hydrotreating of heavy gas oil with inter-stage hydrogen sulfide removal", MSc. Thesis, University of Saskatchewan, Saskatoon, 2003.

Botchwey, C., Dalai, A., and Adjaye, J., "Simulation of a Two-Stage Micro Trickle-Bed Hydrotreating Reactor using Athabasca Bitumen-Derived Heavy Gas Oil over Commercial $NiMo/Al_2O_3$ Catalyst: Effect of H_2S on HDS and HDN", International Journal of Chemical Reactor Engineering, Vol.4, 2006

Bouwens, S.M.A.M., van Zon, F.B., van Dijk, M. M.P., van der Kraan, A.M., de Beer, V.H.J., van Veen, J.A.R., and Koningsberger, D.C., "On the Structural Differences Between Alumina-Supported Comos Type I and Alumina-, Silica-, and Carbon-Supported Comos Type II Phases Studied by XAFS, MES, and XPS", J. Catal. 146, 375, 1994

Breivik R., Egebjerg, R., "Novel Coker Naphtha Hydrotreating Technology" ERTC 12th Annual Meeting, 2007

Breysse, M., Portefaix, J.L., and Vrinat, M., "Support effect on hydrotreating", Catal. Today, 10, 489-505, 1991

Breysse M., Djega M., Gerald P., Stephanie G., Christophe V., Michel P.G., Lemaire M "Deep desulfurization: reactions, catalysts and technological challenges", Catalysis Today, 129-138, 84, (3-4), 2003

Breysse, M., Afanasiev, P., Geantet, C., Vrinat, M., "Overview of support effects in hydrotreating catalysts", Catal. Today, 86, 5-16, 2003

Breysse M., Geauntet C., Afanasiev P., Blanchard J., Vrinat M., "Recent studies on the preparation, activation and design of active phases and supports of

hydrotreating catalysts", Catalysis Today, 3-13, 130, 2008

Brodie-Linder, N., Dosseh, G., Alba-Simonesco, C., Audonnet, F., Imperor-Clerc, M., "SBA-15 synthesis: Are there lasting effects of temperature change within the first 10min of TEOS polymerization?" Mat. Chem. & Phys., 108, 73–81, 2008

Byskov, L., Hammer, B., Nørskov, J.K., Clausen, B.S., and Topsøe, H., Catal. Lett. 47, 177, 1997

Callejas M.A., Martinez M.T., "Hydroprocessing of Maya Residue: Intrinsic kinetics of sulfur, nitrogen, and vanadium removal reactions", Energy and Fuels, 629-636, 13, 1999

Callejas, M.A., Martinez, M.T., Blasco, T., and Sastre, E., "Coke Characterization in aged residue hydrotreating catalysts by solid-state ^{13}C-NMR spectroscopy and temperature-programmed oxidation", Appl. Catal. A, 218, 181, 2001

Cao, Y., Hu, J.C., Yang, P., Dai, W.L., Fan, K.N., "CuCl catalyst heterogenized on diamide immobilized SBA-15 for efficient oxidative carbonylation of methanol to dimethylcarbonate", Chem. Comm., 908-909, 2003

Cao, L., Man, T., and Kruk, M., "Synthesis of ultra-large-pore SBA-15 silica with two-dimensional hexagonal structure using triisopropylbenzene as micelle expander, Chem. Mater., 21, 1144–1153, 2009

Chianelli R.R., Berhault G., Torres B., "Unsupported transition metal sulfide catalysts: 100 years of science and application", Catal. Today, 275-286, 147, 2009

Chu C.P., and Ng, K.M., "Flow in packed tubes with a small tube to particle diameter ratio" AICHE J., 35:148, 1989

Clausen B. S., Massoth F.E., Topsoe H., "Catalysis - Science and Technology", PRODUserv Springer Produktions – Gesellschaft, Berlin, 77, 1996

Cocchetto J.F., Satterfield C.N., "Chemical Equilibria among quinoline and its reaction products in hydrodenitrogenation", Industrial and Engineering Chemistry Process Design and Development, 49-53, 20, 1981

Crajé, M.W.J., "Hydrodesulfurization Catalysis and Mechanism of Supported Transition Metal Sulfides", Ph.D. Thesis, Delft University of Technology, Delft, 1992

Coulier, L., "Hydrotreating Model Catalysts: from characterization to kinetics", PhD. Dissertation, Technische Universiteit Eindhoven, 2001.

Coulier, L., de Beer, V.H.J., van Veen, J.A.R., and Niemantsverdriet, J.W., "Correlation between Hydrodesulfurization Activity and Order of Ni and Mo Sulfidation in Planar Silica-Supported NiMo Catalysts: The Influence of Chelating Agents", J. Catal., 197, 26–33, 2001

Daage M., Chianelli R.R., "Structure-function relations in molybdenum sulphide catalysts: The 'rim-edge' model", J. Catal., 414-427, 149, 1994

de Bruijn, A. "Testing of HDS Catalysts in Small Trickle Phase Reactors", Proceedings 6th International Congress on Catalysis, Imperial College, London, July, p 951, 1976

DeCanio, E.C., Weissman, G.J., "FT-IR Analysis of Borate-Promoted NiMo/γ-$A1_2O_3$ Hydrotreating Catalysts", Colloids and Surfaces, A: Physiochemical and Engineering Aspects, 105, 123, 1995

Delmon, B., Bull. Soc. Chim. Belg. 88, 979, 1979

Delmon, B., in "Catalysts in Petroleum Refining", (Trimm, D.L., Akashah, S., Absi-Halabi, M., and Bishara, A., Eds.), p.1. Elsevier, Amsterdam, 1990

Delvaux, G., Grange, P., and Delmon, B., "X-ray photoelectron spectroscopic study of unsupported cobalt-molybdenum sulfide catalysts", J. Catal., 56, 99-109, 1979

Department of Justice Canada, "Sulfur in gasoline regulations, 1999", Canadian Environmental Protection Act, 1999

Dhar, G.M., Rana, M.S., Maity, S.K., Srinivas, B.N., Prasada Rao, T.S.R., in: C. Song, S. Hsu, I. Mochida (Eds.), "Chemistry of Diesel Fuels", Taylor & Francis, 2000 (Chapter 8).

Dhar, G.M., Srinivas, B.N., Rana, M.S., Kumar, M., Maity, S.K., "Mixed oxide supported hydrodesulfurization catalysts – A review", Catal. Today, 86, 45, 2003

Dhar, G.M., Kumarana, G.M., Kumara, M., Rawat, K.S., Sharma, L.D., Raju, B.D., Rao, K.S.R., "Physico-chemical characterization and catalysis on SBA-15 supported molybdenum hydrotreating catalysts", Catal. Today, 99, 309-314, 2005

Diez, F., Gates, B., Miller, J., Sajcowski, D., and Kukes, S., "Deactivation of a Ni-Mo/γ-$A1_2O_3$ Catalyst: Influence of Coke on the Hydroprocessing Activity", Ind. Eng. Chem. Res., 29, 1999-2004, 1990

Duan, A.; Chun-ming, X.; Shi-xing, L.; Keng, H.C., Journal of Chem. Engineering of Chinese Universities, 19, (5), 762, 2005

Dusseault, M.B. "Comparing Venezuelan and Canadian Heavy Oil and Tar Sands" . Calgary, Canada: Canadian International Petroleum Conference, 2008

Eijsbouts, S., "On the flexibility of the active phase in hydrotreating catalysts", Appl. Catal. A., 158, 53-92, 1997

Eijsbouts, S., Mayo, S. W., Fujita, K., "Unsupported transition metal sulfide catalysts: From fundamentals to industrial application", Appl. Catal. A., 58-66, 2007

Facchetti, R., Cadoppi, A., "Simulated Distillation of Petroleum Products (ASTM D2887) by GC in less than two minutes", Thermo Electron Corporation, Milan, Italy, 2005

Farragher, A.L., and Cossee, P., "Proc. 5th Int. Congress on Catalysis",J.W. Hightower, Ed., Elsevier, Amsterdam, 1301, 1973

Ferdous, D., "Surface morphology of NiMo catalyst supported on γ-Al_2O_3: Impact on hydroprocessing of heavy gas oil derived from Athabasca bitumen", PhD. dissertation, University of Saskatchewan, Saskatoon, 2003

Ferdous, D.; Dalai, A.K.; Adjaye, J., "Hydrodenitrogenation and hydrodesulfurization of heavy gas oil using NiMo/γ-Al_2O_3 catalyst containing Boron: Experimental and kinetic studies", J. Ind. Eng. Chem. Res., 45, 544, 2006

Fischer, R.H., Angevine, P.J., "Dependence of resid processing selectivity on catalyst pore size distribution", Appl. Catal., 1986, 27, 275-283

Frank, J.P and J. F. LePage, "Proceedings on the 7th International Congress on Catalysis", 792, 1981

Furimsky, E., Massoth, F.E., "Deactivation of hydroprocessing catalysts", Catal. Today, 52, 381-495, 1999

Furimsky, E., "Catalysts for upgrading heavy petroleum feeds", Volume 169, p.77, 2007

Gary, J. H.; Handwerk, G. E.; Kaiser, M. J. Petroleum Refining, 5th Ed., p.197, 2004

Gates, B.C., Katzer J.R., and Schuit, G.C.A., “Chemistry of Catalytic Processes”, McGraw Hill: New York, 1979

Gaylord Chemical Company, L.L.C.; “An overview of catalyst sulfiding”, Product Information Bulletin, October, 2007.

Germain, A.H., Wauters, M.L., L'Homme, G.A., Lefebvre, A.G., “Obtaining intrinsic kinetic data using a micro trickle bed reactor: the hydrogenation of glucose on supported ruthenium”, Studies in Surface Science and Catalysis, 7 (Pt. B, New Horiz. Catal.), 1492-3, 1981

Gierman H., “Design of laboratory hydrotreating reactors: Scaling Down of Trickle-flow Reactors”, Appl. Catal., 43, 277-286, 1988

Girgis, M.J., and Gates, B.C., “Reactivities, Reaction Networks, and Kinetics in High-Pressure Catalytic Hydroprocessing”, Industrial and Engineering Chemistry Research, 30, 2021-2058, 1991

Gray, M.R., “Upgrading Petroleum Residues and Heavy oils.” Mercel Dekker, Inc. New York, 1994

Gregg S.J., Sing K.S.W., “Adsorption, Surface Area and Porosity”, London; New York Academic Press, 1967

Gruia, A., David S.J., Pujado, P.R., “Handbook of Petroleum Processing”, Springer Netherlands, 2006, Chapter 8.

Guichard, B., Roy-Auberger, M., Devers, E., Pichon, C., Legens, C., “Characterization of aged hydrotreating catalysts. Part II: The evolution of the mixed phase. Effects of deactivation, activation and/or regeneration”, Appl. Catal. A: General, 9-22, 367, 2009

Han, Y., Xiao, F.S., Wu, S., Sun, Y., Meng, X., Li, D., Lin, S., Deng, F., Ai, X., " A Novel Method for Incorporation of Heteroatoms into the Framework of Ordered Mesoporous Silica Materials Synthesized in Strong Acidic Media", J. Phys. Chem. B., 105, 7963-7966, 2001

Hanika, J., Sporka, K., Ruzicka, V. and Hrstka, J., "Measurement of Axial Temperature Profiles in an Adiabatic Trickle Bed Reactor," Chem. Eng. J., 12, 193-197, 1976

Hanika, J., Vosecki, V., Ruzicka, V., "Diffusion of gases in liquids. II. Dissolution of a stationary gas bubble in a liquid", Chem. Eng. J., 21, 108, 1981

Hensen, E.J.M., "Hydrodesulfurization Catalysis and Mechanism of Supported Transition Metal Sulfides," PhD dissertation, Eindhoven University of Technology, The Netherlands, 2000

Ho T.C., "Hydrodenitrogenation catalysis", Catalysis Reviews, Science and Engineering, 117-160, 30, 1988

Hubaut, R., Rives, A., Luis, M., Scott, C.E., "Surface characterization of bulk Fe–Mo mixed sulfide catalysts", Catal. Comm.,134–139, 2003

Hughes, R., "Deactivation of catalysts," Academic Press, New York, 1984

Inoguchi, M. "Control of Pore Size of Supports", Shokubai, 20, 144-154, 1978

Kabe, K., Ishihara, A., Qian, W., "Hydrodesulfurization and Hydrodenitrogenation", Kodansha, Tokyo, 1999

Kooyman, P.J., P. Waller, A.D. van Langeveld, C.S. Song, K.M. Reddy and J.A.R. van Veen. "Stability of MCM-41-supported CoMo Hydrotreating Catalysts", Catal. Letters, 90 (3-4), 131-135, 2003

Kruk, M., and Jaroniec, M., "Characterization of the Porous Structure of SBA-15", Chem. Mater. 2000, 12, 1961-1968

Kruk, M., and Cao, L., "Pore size tailoring in large-pore SBA-15 silica synthesized in the presence of hexane", Langmuir, 23, 7247–7254, 2007

Kwak, C., Kim, M.Y., Choi, K., Moon, S.H., "Effect of phosphorus addition on the behavior of $CoMoS/Al_2O_3$ catalyst in hydrodesulfurization of dibenzothiophene and 4,6-dimethyldibenzothiophene" Appl. Catal. A, 185, 19-27, 1999

Kwak, C., Lee, J.J., Bae, J.S., Choi, K., Moon, S.H., "Hydrodesulfurization of DBT, 4-MDBT, and 4,6-DMDBT on fluorinated $CoMoS/Al_2O_3$catalysts", Appl. Catal. A, 200, 233-242, 2000

Landau, M. V. "Deep desulfurization of diesel fuels: kinetic modeling of model compounds in trickle-bed", Catal. Today, 36, 393, 1997

La Parola, V., Deganello, G., Tewell, C.R., Venezia, A.M., "Structural characterisation of silica supported CoMo catalysts by UV Raman spectroscopy, XPS and X-ray diffraction techniques", Appl. Catal. Gen. A, 235, 171, 2002

Lauritsen J.V., Kibsgaard J., Olesen G.H., Moses P.G., Hinnemann B., Helveg S., Nørskov J.K., Clausen B.S., Topsøe H., Lægsgaard E., Besenbacher F., "Location and coordination of promoter atoms in Co- and Ni-promoted MoS_2-based hydrotreating catalysts", J. Catal., 220-233, 249, 2007

Ledoux M.J., Hantzer S., "Hydrotreatment catalyst poisoning by vanadium and nickel porphyrin. ESR and NMR", Catalysis Today, 479-496, 7, 1990

Lee, J.J., Kim, H., Koh, J.H., Jo, A., Moon, S.H., "Performance of $CoMoS/Al_2O_3$ prepared by sonochemical and chemical vapor deposition methods in the

hydrodesulfurization of dibenzothiophene and 4,6-dimethyldibenzo-thiophene", Appl. Catal. B: Environ. 58, 89-95, 2005

Leffler, William, "Petroleum Refining in Nontechnical Language", 3rd ed., PennWell Corporation, 2000.

Linares, C.F., Amezqueta, P., Scott, C., "Mo/MCM-41-Type Mesoporous Materials Doubly Promoted With Fe and Ni for Hydrotreating Reactions", Fuel 87, 2817–2823, 2008

Lizama, L., and Klimova, T., "Highly Active Deep HDS Catalysts Prepared Using Mo and W Heteropolyacids Supported on SBA-15", Appl. Catal. B: Environ., 82, 139, 2008

Luck F., "A review of support effects on the activity and selectivity of hydrotreating catalysts", Bulletin des Sociétés Chimiques Belges, 781-800, 100, 1991

Maity S.K., Ancheyta J., Alonso F., Vazquez J.A., "Study of accelerated deactivation of hydrotreating catalysts by vanadium impregnation method", Catalysis Today, 405-410, 130, 2008

Mapiour, M.L., "Effect of hydrogen partial pressure on hydroprocessing of heavy gas oil derived from oil-sands bitumen", MSc. Thesis, University of Saskatchewan, Saskatoon, 2009

Muller, B., Van Langeveld, A.D., Moulijn, J.A., Knozinger, H., " Characterization of Sulfided Mo/Al2O 3 Catalysts by Temperature Programmed Reduction and Low Temperature Fourier Transform Infrared Spectroscopy of Adsorbed Carbon Monoxide", J. Phys. Chem. 97, 9028-9033, 1993

Netzel D.A., Miknis F.P., Mitzel J.M., Zhang T., Jacobs P.D., Haynes Jr. H.W., "Carbon-13 solid-state NMR investigation of coke deposits on spent catalysts used in coal liquefaction", Fuel, 1397-1405, 75, 1996

Niemantsverdriet, J.W., "Spectroscopy in Catalysis – An Introduction, 2nd Completely Revised Ed.", Weinheim, Wiley-VCH, 2000

Okamoto, Y., Breysse, M., Dhar, G. M., Song, C., "Effect of support in hydrotreating catalysis for ultra clean fuels", Catal. Today, 861–3, 2003

Owusu-Boakye, A., "Two-stage aromatics hydrogenation of bitumen-derived light gas oil", MSc. Thesis, University of Saskatchewan, Saskatoon, 2005

Podlubny, J.; "Alberta's Oil Sands – Resourceful, Responsible", JWP Publishing, September, 2008

Pozas, R., Morales, M.P., Serna, C.J., Ocana, M., "Acicular iron Nanoparticles protected against sintering with aluminium oxide", Bol. Soc. esp. Ceram. V., 43, (4), 796-800, 2004

Prada, S.R., Fierro, J.L.G., Grange, P., and Delmon, B., in: Delmon, B., Grange, P., Jacobs, P.A., and Poncelet, G., (Eds.), "Preparation of Catalysts IV", Elsevier, Amsterdam, p. 605, 1987

Ramirez, L.F., Escobar, J., Galvan, E., Vaca, H., Murrieta, F.R., and Luna, M.R.S., "Evaluation of diluted and undiluted trickle-bed hydrotreating reactor with different catalyst volume" Petroleum Science and Technology, 22, (1-2), 157-175, 2004

Rana, M.S., Srinivas, B.N., Maity, S.K., Dhar, G.M., Prasada, T.S.R., in: B. Delmon, G.F. Froment, P. Grange (Eds.), "Hydrotreatment and Hydrocracking of Oil Fractions", Stud. Surf. Sci. Catal. 127, 397, 1999

Ratnasamy, P., and Sivasanker, S., "Structural Chemistry of Co-Mo/Al_2O_3 Catalysts", Catal. Rev.-Sci. Eng., 22, 401, 1980

Ryoo, R.; Ko, C. H.; Kruk, M.; Antochshuk, V.; Jaroniec, M., "Block-Copolymer Templated Ordered Mesoporous Silica: Array of Uniform Mesopores or Mesopore−Micropore Network?", Journal of Physical Chemistry B, 104, (48), 11465-11471, 2000

Satterfield C.N., "Chapter 9: Processing of petroleum and hydrocarbons", Heterogeneous Catalysis in Industrial Practice, 339-417, New York: McGraw-Hill, 1991

Schmidt-Winkel, P., Lukens, W.W., Zhao, D., Yang, P., Chmelka, B.F, Stucky, G.D., "Mesocellular Siliceous Foams with Uniformly Sized Cells and Windows", J. Am. Chem. Soc., 121, 254-255, 1999

Seki. H.; Yoshimoto, M., "Deactivation of HDS catalyst in two-stage RDS process II. Effect of crude oil and deactivation mechanism", Fuel Processing Technology 69, 229–238, 2001

Shimada, H., Sato, T., Yoshimura, Y., Hiraishi, J., Nishijima, A., "Support effect on the catalytic activity and properties of sulfided molybdenum catalysts", J. Catal., 110, (2), 275-284, 1988

Sigurdson, S.K., "Hydrotreating of light gas oil using carbon nanotube supported NiMoS catalysts: Influence of pore diameters", MSc. Thesis, University of Saskatchewan, Saskatoon, 2009

Smith, J. M., "Chemical Engineering Kinetics", McGraw-Hill Book Company, Inc., 1956

Song, C.S., Nihonmatsu, T., Nomura, M., "Effect of pore structure of nickel-molybdenum/alumina catalysts in hydrocracking of coal-derived and oil sand derived asphaltenes", Ind. Eng. Chem. Res., 30, 1726-1734, 1991

Song, C.S., "Fuel processing for low-temperature and high-temperature fuel cells: Challenges, and opportunities for sustainable development in the 21st century", Catal. Today, 77, (1-2), 17-49, 2002

Sørensen O., Clausen B., Candia R., Topsøe H., "HREM and AEM studies of HDS catalysts: Direct evidence for the edge location of cobalt in Co-Mo-S", Appl. Catal., 363-372, 13, 1985

Speight, J. G., The Desulfurization of Heavy Oils and Residua, Marcel Dekker Inc., New York, 1981

Speight, J. G. "The Desulfurization of Heavy Oils and Residua", Marcel Dekker Inc., New York, 2000

Stanislaus, A., and Cooper, B.H., "Aromatic Hydrogenation Catalysis: A Review", Catal. Rev. Sci. Eng. 36, 75-123, 1994

Suman, K. J., Reiichi, N., Kazuya, S., Tsuyoshi, K., Seitaro, N., "Pore size control of mesoporous molecular sieves using different organic auxiliary chemicals" J. Micro. & Meso. Mater., 68, 133-142, 2004

Sun, J., Zhang H., Ma, D., Chen, Y., Bao, X., Klein-Hoffmann, A.. Pfanderb N., Sheng, D., "Alkanes-assisted low temperature formation of highly ordered SBA-15 with large cylindrical mesopores", Chem. Comm, 5343-5345, 2005

Sundaramurthy, V., Eswaramoorthi, I., Dalai, A.K., Adjaye, J. "Hydrotreating of gas oil on SBA-15 supported NiMo catalysts", J. Micro. & Meso. Mater., 111, 560, 2008

Takahashi, T., Higashi, H., Kai, T., Department of Applied Chemistry & Chemical Eng, Kagoshima University, 2003

Takeuchi, C., "Hydrotreating Catalysts for Heavy Oils", Kagaku Kogaku, 50, 598-603, 1986

Ternan, M., "Catalytic hydrogenation and asphaltene conversion of Athabasca bitumen", Can. J. Chem. Eng., 61, 689-696, 1983

Topsoe H., Clausen B.S., Massoth F.E., "Hydrotreating Catalysis - Science and Technology", New York: Springer-Verlag, 1996

Topsøe, N.Y., and Topsøe, H., "Characterization of the structures and active sites in sulfided $CoMo/Al_2O_3$ and $NiMo/Al_2O_3$ catalysts by NO chemisorption" J. Catal. 84, 386-401, 1983

Topsøe, H., Clausen, B.S., "Importance of Co-Mo-S Type Structures in Hydrodesulfurization", Catal. Rev. Sci. Eng., 26, 395, 1984

Trong On, D., Desplantier-Giscard, C., Danumah and Kaliaguine, S., "Perspectives in catalytic applications of mesostructured materials", Appl. Catal. A, 222, 299-357, 2001

Toulhoat, H., "Hydrotreating Catalysts: Where are the limits, as expectations keep growing?", Symposium 20 – Hydrotreating catalysis, 2001

van Veen, J.A.R., Gerkema, E., van der Kraan, A.M., Hendriks, P.A.J.M., and Beens, H., "A ^{57}Co Mössbauer emission spectrometric study of some supported CoMo hydrodesulfurization catalysts", J. Catal., 133, 112-123, 1992

van Veen, J.A.R., Colijn, H.A., Hendriks, P.A.J.M., and van Welsenes, A.J., "On the formation of type I and type II nickel molybdenum sulfide phases in nickel-

molybdenum/alumina hydrotreating catalysts and its catalytic implications", Fuel. Proc. Technol. 35, 137 (1993).

van Santen, R.A., and Niemantsverdriet, J.W., "Chemical Kinetics and Catalysis", Plenum, New York, 1995

Vishwakarma, S.K, "Sonochemical and impregnated Co-W/γ-Al_2O_3 catalysts: Performances and kinetic studies on hydrotreatment of light gas oils", MSc. Thesis, University of Saskatchewan, Saskatoon, 2007

Voorhoeve, R.J.H., and Stuiver, J.C.M., "Kinetics of hydrogenation on supported and bulk nickel-tungsten sulfide catalysts", J. Catal. 23, 228 (1971).

Vradman, L., Landau, M. V., Herskowitz, M., Ezersky, V., Talianker, M., Nikitenko, S., Koltypin, Y., Gedanken, A., "High Loading of Short WS_2 Slabs inside SBA-15: Promotion with Nickel and Performance in Hydrodesulfurization and Hydrogenation", J. Catal., 213, 163, 2003

Vradman, L. Landau, M.V. Kantorovich, D. Koltypin, Y. Gedanken, A., "Evaluation of metal oxide phase assembling mode inside the nanotubular pores of mesostructured silica", Microp. Mesop. Mater., 70 307-318, 2005

Whitehurst, D. D. Takaaki, I. Mochida, "Present State of the Art and Future Challenges in the Hydrodesulfurization of Polyaromatic Sulfur Compounds", Adv. Catal., 42, 344-368, 1998

Wivel C., Candia R., Clausen B.S., Mørup S., Topsøe H., "On the catalytic significance of a Co-Mo-S phase in Co-Mo/Al_2O_3 hydrodesulfurization catalysts: Combined in situ Mössbauer emission spectroscopy and activity studies", Journal of Catalysis, 453-463, 68, 1981

Wivel, C., Clausen, B.S., Candia, R., Mørup, S., and Topsøe, H., "Mössbauer emission studies of calcined CoMo/Al_2O_3 catalysts: Catalytic significance of Co precursors", J. Catal. 87, 497-513, 1984

Wu, Z., Chu, S.Y., Yang, Z., Wei, C., Li, Q., Xin, "Sulfur Effect on Mo_2N/γ-Al_2O_3 Catalyst Studied by in Situ FT-IR Spectroscopy", J. Catal., 194, 23-32, 2000

Wypych, F., Sollmann K., and Schöllhorn, R., "Metastable layered chalcogenides 1T-MoS_2, 2M-S_2 and 1T-$Mo_{1/2}W_{1/2}S_2$: Electrochemical study on their intercalation reactions", Materials Research Bulletin, Volume 27, Issue 5, 545-553, 1992

http://en.wikipedia.org/wiki/Pluronic_P-123 (Accessed on January 10, 2011)

http://en.wikipedia.org/wiki/Sol-gel (Accessed on January 10, 2011)

http://eetd.lbl.gov/ecs/aerogels/sa-thermal.html (Accessed on Feb 28, 2011)

http://www.sciencedaily.com/releases/2010/03/100310134255.htm (Accessed on 19th May, 2010)

http://www.ec.gc.ca/CEPARegistry/Regulations/DetailReg.cfm?intReg=9 (Accessed on 4th January, 2009)

http://www.saocl.com/html_image/Bitumen%20Definition.htm (Accessed on 27th May, 2010)

Yong-Jin Han et al., "Synthesis and Inclusion Chemistry of Mesoporous Silicate SBA-15 and related Materials," Ph. D Thesis, University of Santa Barbara, California, September, 2002

Zandbergen, H.W. and Traeholt, C., in "Handbook of microscopy. Applications in materials science, solid–state physics and chemistry" (S. Amelinx, D. van

Dyck, J. van Landuyt, and G. van Tendeloo, Eds.), p. 719. VCH, Weinheim, 1997

Zepeda, T.A., Pawelec, B., Fierro, J.L.G., Halachev, T., "Effect of Ti on the catalytic properties of CoMo/Ti(x)-HMS catalysts in the reaction of hydrodesulfurization of 4-ethyl-6-methyl dibenzothiophene", J. Catal., 242, 254-269, 2006

Zeuthen P., Knudsen K.G., Whitehurst D.D., "Organic nitrogen compounds in gas oil blends, their hydrotreated products and the importance to hydrotreatment", Catalysis Today, 307-314, 65, 2001

Zhao, D., Huo, Q., Feng, J., Chmelka, B.F., Stucky, G.D., "Nonionic triblock and star diblock copolymer and oligomeric sufactant syntheses of highly ordered, hydrothermally stable, mesoporous silica structures" Journal of the American Chemical Society, 120, (24), 6024-6036, 1998

Zhao, S., Kotlyar, L.S., Woods, R.R., Sparks, B.D., Chung, K.H., "Molecular Nature of Athabasca Bitumen", Petroleum Science and Technology, 18 (5-6), 587, 2000

APPENDIX A1: Heavy gas oil characteristics for hydrotreating experiment

Characteristics	Quantities	
	Pore Diameter Variation Studies (Phase I)	**Metals Optimization & Long-term Deactivation Studies (Phases II & III)**
Nitrogen content (wt.%)	0.36	0.37
Sulfur content (wt.%)	4.23	4.16
Density (reported, g/mL)	0.99	0.98
Simulated Distillation (ºC)		
Initial Boiling Point	210.8	208.5
Final Boiling Point	597.3	591.6
Hydrocarbon Content	**Fraction distilled off (wt.%)**	
IBP-205	0	0
205-260	1	2
260-315	5	7
315-425	39	40
425-600	55	51

APPENDIX A2: Distillates boiling ranges and carbon numbers of typical hydrocarbon fractions present in heavy gas oil.

Fraction boiling range (ºC)	Distillate	Carbon number	HGO Feedstock (wt.%)
IBP-205	Gasoline (G)	$\leq C_{11}$	0
205-260	Kerosene (K)	C_{12}-C_{14}	1
260-315	LGO	C_{15}-C_{18}	5
315-425	HGO	C_{18}-C_{28}	39
425-600	VGO	C_{28}-C_{60}	55

APPENDIX B:

Calculating molar product concentrations of N/S & reaction rates of HDN/HDS

The sulfur and nitrogen concentrations in the feed and product gas oil liquids are found via the following equations:

$$C_S = \frac{(ppm_{wt}) \cdot \rho_L}{(10^6) \cdot M_S} = \frac{(ppm_{wt}) \cdot \left(0.99 \times 10^3 \frac{g}{L}\right)}{(10^6) \cdot \left(32.0640 \frac{g}{mol}\right)} \quad [B.1]$$

$$C_N = \frac{(ppm_{wt}) \cdot \rho_L}{(10^6) \cdot M_N} = \frac{(ppm_{wt}) \cdot \left(0.99 \times 10^3 \frac{g}{L}\right)}{(10^6) \cdot \left(14.0067 \frac{g}{mol}\right)} \quad [B.2]$$

$\boldsymbol{\rho_L}$ = Density of HGO feedstock and product (averaged) = 0.99 g/mL

$\boldsymbol{C_{S/N}}$ = Sulfur/nitrogen heteroatom concentration, mol/L (M)

$\boldsymbol{M_{S/N}}$ = Sulfur/nitrogen molecular weight, g/mol

The global rates of both the HDS and HDN reactions were found from the following equations:

$$\{R_{HDS}\} = \frac{\left([C_O]_S - [C_P]_S\right) \cdot LHSV}{\left(3600 \frac{s}{h}\right) \cdot \rho_{CAT}} \quad [B.3]$$

$$\{R_{HDN}\} = \frac{\left([C_O]_N - [C_P]_N\right) \cdot LHSV}{\left(3600 \frac{s}{h}\right) \cdot \rho_{CAT}} \quad [B.4]$$

$\boldsymbol{\{R_{HDS/HDN}\}}$ = Global rate of the HDS/HDN reaction, mol/(s·kg-cat)

$\boldsymbol{[C_{O/P}]_{S/N}}$ = Feedstock/product concentration of sulfur/nitrogen, mol/L

$\boldsymbol{LHSV}$ = Liquid hourly space velocity, h^{-1}

$\boldsymbol{\rho_{CAT}}$ = Catalyst pellet density = 0.31 ± 0.01 g/mL (FeW/SBA-15 catalyst)

APPENDIX C:

Product concentrations and conversions of N/S from the kinetics study of HDS/HDN for the optimum FeW/SBA-15 catalyst

Run time (days)	T (°C)	LHSV (h^{-1})	P (MPa)	G/L (mL/mL)	$[C_p]_S$ (ppm)	$[C_0 - C_p]_S/[C_0]_S$ (no units)	$[C_p]_N$ (ppm)	$[C_0 - C_p]_N/[C_0]_N$ (no units)
1	375	1.0	8.8	600	15747.5	0.628	1927.9	0.467
2	375	1.0	8.8	600	22758.3	0.462	2241.2	0.380
3	375	1.0	8.8	600	24423.5	0.423	2351.2	0.350
4	375	1.0	8.8	600	24320.2	0.425	2569.0	0.289
5	375	1.0	8.8	600	24681.9	0.417	2581.2	0.286
6	375	1.0	8.8	600	20950.3	0.505	2652.7	0.266
7	375	1.0	8.8	600	20232.0	0.522	2530.8	0.300
8	388	1.0	8.8	600	17993.9	0.575	2512.2	0.305
9	388	1.0	8.8	600	17649.9	0.583	2536.3	0.298
10	388	1.0	8.8	600	17532.1	0.586	2487.2	0.312
11	400	1.0	8.8	600	14287.6	0.662	2235.9	0.381
12	400	1.0	8.8	600	10669.9	0.748	1881.7	0.479
13	400	1.0	8.8	600	11045.7	0.739	1921.7	0.468
14	375	1.0	8.8	600	20287.6	0.520	2597.1	0.282
15	375	1.0	8.8	600	21065.7	0.502	2627.9	0.273
16	375	1.0	8.8	600	20684.2	0.511	2600.9	0.281
17	388	0.5	8.8	600	9152.5	0.784	2412.8	0.333
18	388	0.5	8.8	600	8789.0	0.792	2064.9	0.429
19	388	0.5	8.8	600	8241.3	0.805	2052.6	0.432
20	388	1.5	8.8	600	18156.7	0.571	2713.6	0.249
21	388	1.5	8.8	600	18398.2	0.565	2797.0	0.226
22	388	1.5	8.8	600	18987.5	0.551	2676.3	0.260
23	388	2.0	8.8	600	24656.7	0.417	2823.3	0.219
24	388	2.0	8.8	600	24903.7	0.411	2791.7	0.228
25	388	2.0	8.8	600	24996.5	0.409	2884.8	0.202

26	388	1.0	7.6	600	22730.9	0.463	3176.9	0.121
27	388	1.0	7.6	600	23736.4	0.439	3183.6	0.119
28	388	1.0	7.6	600	24703.7	0.416	3186.1	0.119
29	388	1.0	8.3	600	14579.3	0.655	2756.8	0.237
30	388	1.0	8.3	600	15671.4	0.630	2648.7	0.267
31	388	1.0	8.3	600	15979.1	0.622	2794.7	0.227
32	388	1.0	9.6	600	10207.8	0.759	2499.5	0.309
33	388	1.0	9.6	600	10129.8	0.761	2534.7	0.299
34	388	1.0	9.6	600	10621.3	0.749	2372.6	0.344
35	388	1.0	8.8	400	22418.7	0.470	2878.3	0.204
36	388	1.0	8.8	400	21738.8	0.486	2822.5	0.219
37	388	1.0	8.8	400	20976.4	0.504	2865.1	0.207
38	388	1.0	8.8	800	14993.9	0.646	2296.2	0.365
39	388	1.0	8.8	800	14649.9	0.654	2292.2	0.366
40	388	1.0	8.8	800	14513.2	0.657	2296.3	0.365
41	388	1.0	8.8	1000	10649.9	0.748	2167.2	0.400
42	388	1.0	8.8	1000	11406.9	0.730	2021.4	0.441
43	388	1.0	8.8	1000	11668.6	0.724	2084.9	0.423
Run time (days)	**T (ºC)**	**LHSV (h^{-1})**	**P (MPa)**	**G/L (mL/mL)**	**$[C_p]_S$ (ppm)**	**$[C_0 - C_p]_S/[C_0]_S$ (no units)**	**$[C_p]_N$ (ppm)**	**$[C_0 - C_p]_N/[C_0]_N$ (no units)**
1	388	1.0	8.8	600	16074.3	0.620	2671.2	0.2610
2	388	1.0	8.8	600	16652.6	0.606	2709.1	0.2506
3	388	1.0	8.8	600	16991.7	0.598	2754.5	0.2380
4	388	1.0	8.8	600	16760.3	0.604	2711.2	0.2500
5	388	1.0	8.8	600	16767.3	0.604	2765.9	0.2349
6	388	1.0	8.8	600	16969.8	0.599	2719.1	0.2478
7	388	1.0	8.8	600	16493.7	0.610	2692.7	0.2551
8	388	1.0	8.8	600	16359.8	0.613	2727.2	0.2455
9	388	1.0	8.8	600	16695.5	0.605	2715.7	0.2487
10	388	1.0	8.8	600	16778.9	0.603	2720.3	0.2475

11	388	1.0	8.8	600	16797.2	0.603	2740.7	0.2418
12	388	1.0	8.8	600	16614.8	0.607	2799.2	0.2256
13	388	1.0	8.8	600	17002.9	0.598	2715.0	0.2489
14	388	1.0	8.8	600	17071.0	0.596	2675.8	0.2598
15	388	1.0	8.8	600	16635.7	0.607	2689.2	0.2561
16	388	1.0	8.8	600	17038.9	0.597	2697.0	0.2539
17	388	1.0	8.8	600	17184.0	0.594	2727.0	0.2456
18	388	1.0	8.8	600	16679.1	0.606	2659.9	0.2642
19	388	1.0	8.8	600	16342.8	0.614	2685.4	0.2571
20	388	1.0	8.8	600	17481.4	0.587	2743.6	0.2410
21	388	1.0	8.8	600	16127.5	0.619	2704.8	0.2517
22	388	1.0	8.8	600	16916.1	0.600	2737.1	0.2428
23	388	1.0	8.8	600	16519.8	0.609	2698.8	0.2534
24	388	1.0	8.8	600	16205.9	0.617	2719.2	0.2478
25	388	1.0	8.8	600	16988.6	0.598	2808.1	0.2232
26	388	1.0	8.8	600	16619.7	0.607	2763.7	0.2354
27	388	1.0	8.8	600	16904.1	0.600	2740.2	0.2419
28	388	1.0	8.8	600	16732.3	0.604	2763.3	0.2356
29	388	1.0	8.8	600	16964.7	0.599	2707.4	0.2510
30	388	1.0	8.8	600	17425.8	0.588	2758.1	0.2370
31	388	1.0	8.8	600	16420.1	0.612	2692.3	0.2552
32	388	1.0	8.8	600	17285.7	0.591	2804.7	0.2241
33	388	1.0	8.8	600	16937.8	0.600	2701.3	0.2527
34	388	1.0	8.8	600	17315.5	0.591	2714.0	0.2492
35	388	1.0	8.8	600	16102.0	0.619	2753.9	0.2382
36	388	1.0	8.8	600	16783.6	0.603	2682.2	0.2580
37	388	1.0	8.8	600	16651.7	0.606	2715.0	0.2489
38	388	1.0	8.8	600	16333.9	0.614	2692.7	0.2551
39	388	1.0	8.8	600	16934.5	0.600	2713.5	0.2494
40	388	1.0	8.8	600	16778.9	0.603	2668.4	0.2618

41	388	1.0	8.8	600	16691.7	0.605	2686.4	0.2568
42	388	1.0	8.8	600	16509.7	0.610	2717.6	0.2482
43	388	1.0	8.8	600	16868.3	0.601	2697.0	0.2539
44	388	1.0	8.8	600	17260.7	0.592	2712.7	0.2496
45	388	1.0	8.8	600	16741.6	0.604	2659.9	0.2642
46	388	1.0	8.8	600	16466.5	0.611	2737.0	0.2429
47	388	1.0	8.8	600	17837.4	0.578	2786.2	0.2292
48	388	1.0	8.8	600	16626.1	0.607	2701.3	0.2527
49	388	1.0	8.8	600	16884.2	0.601	2678.5	0.2590
50	388	1.0	8.8	600	17342.9	0.590	2689.9	0.2559
51	388	1.0	8.8	600	16153.2	0.618	2716.3	0.2486
52	388	1.0	8.8	600	17023.8	0.598	2706.3	0.2513
53	388	1.0	8.8	600	15964.8	0.623	2778.2	0.2314
54	388	1.0	8.8	600	17035.8	0.597	2775.1	0.2323
55	388	1.0	8.8	600	16880.8	0.601	2687.0	0.2567
56	388	1.0	8.8	600	16619.7	0.607	2703.4	0.2521
57	388	1.0	8.8	600	17342.9	0.590	2721.9	0.2470
58	388	1.0	8.8	600	16936.8	0.600	2675.2	0.2600
59	388	1.0	8.8	600	17078.2	0.596	2763.3	0.2356
60	388	1.0	8.8	600	16671.2	0.606	2770.8	0.2335

APPENDIX D:

Evaluating the external mass transfer resistances for the HDS & HDN reactions

A criterion developed by Charles N. Satterfield (1969) was used for determining if the rate of hydrogen diffusion within petroleum distillates as part of HDS and HDN reactions was the rate determining step. The criterion is defined as:

$$\left(\frac{10 d_P}{3 C_{H2}}\right) \cdot \left(\frac{-1}{V_C} \cdot \frac{dn}{dt}\right) > k_{OVR} \qquad [D.1]$$

The variables are defined as:

k_{OVR} = Overall mass transfer coefficient for hydrogen, cm/s

C_{H2} = Hydrogen concentration in the liquid phase at equilibrium, mol/mL

$\left(\frac{-1}{V_C} \cdot \frac{dn}{dt}\right)$ = Rate of hydrogen conversion in the reaction, mol/(s·mL)

V_C = Volume of loaded catalyst = 5 mL

d_P = Average diameter of the catalyst particles = 0.17 cm*

*Average particle diameter is between 10 and 14 mesh (US) in size.

The validation of the Satterfield criterion would indicate that hydrogen conversion was dominant over hydrogen mass transfer in the overall reaction.

Estimation of the overall mass transfer coefficient (k_{OVR}):

The overall mass transfer coefficient was found by the following equation:

$$\frac{1}{k_{OVR}} = \frac{1}{k_L} + \frac{1}{k_S} \qquad [D.2]$$

The variables are defined as:

k_L = H_2/HGO mass transfer coefficient – gas/liquid side, cm/s

k_S = H_2/HGO mass transfer coefficient – liquid/solid side, cm/s

Calculation of the gas/liquid mass transfer coefficient (k_L):

The gas/liquid mass transfer coefficient was estimated using a correlation by Goto and Smith (1975):

$$k_L = \alpha_1 \cdot \left(\frac{L_A}{\mu_L}\right)^{\alpha_2} \left(\frac{D_L}{a_L}\right) \cdot \sqrt{\frac{\mu_L}{\rho_L \cdot D_L}} \qquad [D.3]$$

The variables are defined as:

a_L = Interfacial surface area over unit volume $\approx \left(\frac{6(1-\varepsilon)}{d_P}\right)^{*}$ = 24.7 cm^{-1}

*This assumes the interfacial surface area is equal to the catalyst pellet surface area.

ε = Bed porosity = 0.3 (Wijngaarden et al., 1998)

L_A = Liquid mass flow over cross-sectional area, g/(s·cm^2)

μ_L = Viscosity of HGO at the operating temperature, g/(s·cm)

D_L = Diffusivity of hydrogen in HGO, cm^2/s

ρ_L = Density of HGO at the operating conditions, g/mL

α_1 = Constant based on the catalyst particle properties* = 7

α_2 = Constant based on the catalyst particle properties* = 0.4

* α_1 and α_2 values found by Korsten and Hoffman (1996) for d_P = 0.17 cm.

Calculation of HGO viscosity (μ_L):

A correlation developed by Glasso (Ahmed, 1989) was used for estimating the viscosity of HGO at the operating temperatures:

$$\mu_L = 3.141\times10^{10}\cdot(T-460)^{-3.444}\left(\log^{\circ} API\right)^{a} \quad [D.4]$$

$$a = 10.313\cdot\log(T-460)-36.447 \quad [D.5]$$

The variables are defined as:

$\boldsymbol{T}$ = Operating temperature, °R

$$\boldsymbol{^{\circ}API} = \frac{141.5}{SG}-131.5$$

$\boldsymbol{SG}$ = Specific gravity of HGO at 15.6°C = 1.023

$\boldsymbol{^{\circ}API} \approx 11.42$

$\boldsymbol{a}$ = -7.06 to -6.79 (for temperatures ranging from 375°C to 400°C)

$\boldsymbol{\mu_L}$ = 2.809 cP to 2.319 cP (for temperatures ranging from 375°C to 400°C)

Calculation of HGO average molecular weight (M_{AVE}):

A correlation developed by Winn (Sim and Daubert, 1980) was used for calculating the average molecular weight of gas oil:

$$M_{AVE} = m_1\cdot T_b^{\,m_2}\cdot\rho_{15.6}^{\,\beta} \quad [D.6]$$

The variables are defined as:

$\boldsymbol{M_{AVE}}$ = Average molecular weight of HGO, g/mol

$\boldsymbol{T_b}$ = Average boiling point of HGO = 370°C = 698°F

$\boldsymbol{\rho_{15.6}}$ = Density of HGO at 15.6°C = 1.023 g/mL

m_1 = Empirical constant* = 2.41×10^{-6}

m_2 = Empirical constant* = 2.847

β = Empirical constant* = -2.13

*Modified Winn values for gas oil fractions provided by Trytten et al. (1990).

M_{AVE} = 2867.1 g/mol

Calculation of diffusivity of hydrogen in gas oil (D_L):

A correlation by Wilke and Chang (1955) was used for calculating the effective diffusivity of hydrogen:

$$D_L = \left(7.4\times10^{-8}\right)\cdot\frac{T\sqrt{X\cdot M_{AVE}}}{\mu_L\cdot V_b^{0.6}} \qquad [D.7]$$

The variables are defined as:

X = Association parameter = 1 for hydrocarbon mixtures

V_b = Hydrogen molar volume at the normal boiling point

V_b = 14.3 mL/mol (Wiljngaarden et al., 1998)

D_L = 2.89×10^{-4} cm^2/s to 3.65×10^{-4} cm^2/s
(for temperatures ranging from 375°C to 400°C)

Calculation of HGO density at reaction temperatures and pressures:

A correlation by Standing and Katz (Jiménez et al., 2007) was found for determining the density of gas oils at reactor operating conditions:

$$\rho_L = \rho_{15.6} - \Delta\rho_T + \Delta\rho_P \qquad [D.8]$$

$\Delta\rho_T$ = Temperature density correlation, lbs/ft^3

$\Delta\rho_P$ = Pressure density correlation, lbs/ft^3

$$\Delta\rho_P = \left[0.167 + \left(16.181\times10^{-0.0425\rho_{15.6}}\right)\right]\cdot\left[\tfrac{P}{1000}\right] - 0.01\cdot\left[0.299 + \left(263\times10^{-0.603\rho_{15.6}}\right)\right]\cdot\left[\tfrac{P}{1000}\right]^2 \quad [D.9]$$

$$\Delta\rho_T = \left[0.0133 + \left(152.4\cdot(\rho_{15.6}+\Delta\rho_P)^{-2.45}\right)\right]\cdot[T-520] - \left[8.10\times10^{-6} - \left(0.0622\times10^{-0.764(\rho_{15.6}+\Delta\rho_P)}\right)\right]\cdot[T-520]^2 \quad [D.10]$$

The values applied to these equations were:

$\boldsymbol{P}$ = 1100 psia to 1400 psia

$\boldsymbol{T}$ = 1158°R to 1212°R (370°C to 400°C)

From these pressure and temperature values:

$\boldsymbol{\Delta\rho_P}$ = 18.17 lbs/ft^3 to 20.77 lbs/ft^3

$\boldsymbol{\Delta\rho_T}$ = 8.60 lbs/ft^3 to 9.20 lbs/ft^3

$\boldsymbol{\rho_L}$ = 60.72 lb/ft^3 to 62.72 lb/ft^3 = 973 kg/m^3 to 1050 kg/m^3

Finally, from the previously calculated values:

$\boldsymbol{k_L}$ = 1.56×10^{-2} cm/s to 1.72×10^{-2} cm/s

Calculation of the liquid/solid mass transfer coefficient (k_S):

The liquid/solid mass transfer coefficient was estimated using a correlation by Van Krevelen and Krekels (Froment and Bishoff, 1990):

$$k_S = 1.8\cdot D_L\cdot a_S\sqrt{\frac{L_A}{a_S\cdot\mu_L}}\cdot\left(\frac{\mu_L}{\rho_L\cdot D_L}\right)^{1/3} \quad [D.11]$$

The variables are defined as:

$\boldsymbol{a_S}$ = Liquid/solid interfacial surface area = $\boldsymbol{a_L}$ = 24.7 cm^{-1}

Using the previously determined terms:

k_S = 4.48×10^{-1} cm/s to 5.42×10^{-1} cm/s

Calculation of the equilibrium concentration of hydrogen in gas oil (C_{H2}):

The equilibrium concentration of hydrogen in gas oil was calculated by applying Henry's constant with the assumption of limited solubility:

$$C_{H2} = \frac{P}{H_{H2}} \qquad [D.12]$$

The variables are defined as:

H_{H2} = Henry's constant for hydrogen in HGO, MPa·m^3/mol

P = Operating pressure = 7.6 MPa to 10 MPa

Henry's constant can be calculated using the equation below:

$$H_{H2} = \frac{v_N}{\lambda_{H2} \cdot \rho_L} \qquad [D.13]$$

The variables are defined as:

v_N = Hydrogen molar volume at standard conditions = 22.4 L/mol

ρ_L = Density of HGO at the operating conditions = 973 kg/m^3 to 1050 kg/m^3

λ_{H2} = Hydrogen solubility in HGO, mL/(kg·MPa)

A correlation established by Korsten and Hoffmann (1996) was applied to estimate the solubility of hydrogen in gas oil fractions:

$$\lambda_{H2} = z_0 + z_1 \cdot T + z_2 \cdot \frac{T}{\rho_{20}} + z_3 \cdot T^2 + z_4 \cdot \frac{1}{(\rho_{20})^2} \qquad [D.14]$$

The parameters are defined as:

z_0 = -0.55973

$z_1 = -0.42947\times10^{-3}$

$z_2 = 3.07539\times10^{-3}$

$z_3 = 1.94593\times10^{-6}$

$z_4 = 0.83578$

T = Operating temperature = 370°C to 400°C

ρ_{20} = Density of HGO at 20°C = 0.99 g/mL

For the operating conditions, the following value ranges were found:

λ_{H2} = 6.09 mL/(kg·MPa) to 6.42 mL/(kg·MPa)

$H_{H2} = 6.06\times10^{-2}$ MPa·m^3/mol to 5.56×10^{-2} MPa·m^3/mol

$C_{H2} = 1.19\times10^{-4}$ mol/mL to 1.72×10^{-4} mol/mL

Calculating the hydrogen conversion rate for HDS and HDN:

The following simplified stoichiometric equations were used for finding the rate of hydrogen conversion for both hydrodesulfurization and hydrodenitrogenation:

$$\boxed{\left|R-S\right| \; + \; \underline{x_{HDS}} H_2 \xrightarrow{CATALYST} \left|R-H\right|_{[2x_{HDS}-2]} + \; H_2S} \qquad [D.15]$$

$$\boxed{\left|R-N\right| \; + \; \underline{x_{HDN}} H_2 \xrightarrow{CATALYST} \left|R-H\right|_{[2x_{HDN}-3]} + \; NH_3} \qquad [D.16]$$

The rates of nitrogen and sulfur removal for varying operating conditions applied to the hydrotreating process were determined from section 4.4 and Appendix C of the report. Equations D.15 and D.16 allow for the following substitutions:

HDS:

$$\left(\frac{-1}{V_C}\cdot\frac{dn}{dt}\right)=\frac{x_{HDS}\cdot r_{HDS}}{V_C} \qquad [D.17]$$

HDN:

$$\left(\frac{-1}{V_C}\cdot\frac{dn}{dt}\right)=\frac{x_{HDN}\cdot r_{HDN}}{V_C} \qquad [D.18]$$

Where r_{HDS} is the molar rate of sulfur removal and r_{HDN} is the molar rate of nitrogen removal achieved from the hydrotreating catalyst (mol/s). Assuming the hydrogenation of a 5-membered thiophenic ring for sulfur removal and a 6-membered basic pyridinic ring for nitrogen removal, the following stoichiometric values were assumed for the HDS and HDN reactions of heavy gas oil:

$x_{HDS} = 4.0$; $x_{HDN} = 5.0$

Given these assumed values for each reaction, the following value ranges were found for each side of the Satterfield inequality:

Hydrodesulfurization Reaction:

Left hand side of Satterfield's criterion = 3.89×10^{-4} cm/s to 5.43×10^{-4} cm/s

Right hand side of Satterfield's criterion = 1.95×10^{-3} cm/s to 2.72×10^{-3} cm/s

Hydrodenitrogenation Reaction:

Left hand side of Satterfield's criterion = 1.61×10^{-4} cm/s to 2.53×10^{-4} cm/s

Right hand side of Satterfield's criterion = 6.45×10^{-4} cm/s to 1.01×10^{-3} cm/s

A summary of all the operating conditions and estimated parameters contributing to these results can be found in Table D.1 on the following page.

Table D.1
Summary of the external mass transfer resistances study performed for a trickle bed hydrotreating reactor loaded with SBA-15-supported FeW catalyst.

Parameter	Symbol	Value	Units	Value Range
Pressure	**P**	8.8	MPa	7.6 to 10
Temperature	**T**	388	°C	375 to 400
Average boiling point temperature of HGO	$\mathbf{T_b}$	698	°F	-
Liquid hourly space velocity	**LHSV**	1.0	h^{-1}	0.5 to 2.0
Feed flow rate	**L**	5.0	g/h	2.5 to 10.0
Particle size	$\mathbf{d_P}$	0.17	cm	-
Bed porosity (Wijngaarden et al., 1998)	**ε**	0.3	-	-
Interfacial surface area per unit volume	$\boldsymbol{\alpha_L}$	24.7	cm^{-1}	-
Liquid mass flow per unit area	$\mathbf{L_A}$	1.38	$\times 10^{-3}$ g/(cm^2·s)	0.69 to 2.76
HGO density under operating conditions	$\boldsymbol{\rho_L}$	990	kg/m^3	973 to 1050
HGO density at 15.6°C	$\boldsymbol{\rho_{15.6}}$	1023	kg/m^3	-
HGO density at 20°C	$\boldsymbol{\rho_{20}}$	987	kg/m^3	-
Pressure density correlation	$\boldsymbol{\Delta\rho_P}$	19.48	lbs/ft^3	18.17 to 20.77
Temperature density correlation	$\boldsymbol{\Delta\rho_T}$	8.91	lbs/ft^3	8.60 to 9.20
HGO specific gravity at 60°F	**SG**	1.023	-	-
API density rating	**°API**	11.42	-	-
Constant in viscosity correlation (Ahmed, 1989)	**α**	-7.36	-	-7.61 to -7.12
HGO average molecular weight	$\mathbf{M_{AVE}}$	2867.1	kg/mol	-
HGO viscosity at operating temperature	$\boldsymbol{\mu_L}$	2.926	cP	2.809 to 2.319
Henry's constant	$\mathbf{H_{H2}}$	0.058	MPa-m^3/gmol	0.0606 to 0.0556
Hydrogen molecular volume, standard conditions	$\mathbf{v_N}$	22400	cc/mol	-
Concentration of H_2 in HGO	$\mathbf{C_{H2}}$	1.45	$\times 10^{-4}$ mol/cc	1.19 to 1.72
Solubility of H_2 in HGO (Hoffman et al., 1996)	$\boldsymbol{\lambda_{H2}}$	6.26	$\times 10^{3}$ cc/kg	6.09 to 6.42
Bulk diffusivity of hydrogen	$\mathbf{D_L}$	3.27	$\times 10^{-4}$ cm^2/s	2.89 to 3.65
Particle properties constant (Goto & Smith, 1975)	$\boldsymbol{\alpha_1}$	7.0	-	-
Particle properties constant (Goto & Smith, 1975)	$\boldsymbol{\alpha_2}$	0.4	-	-
Liquid side: H_2/HGO mass transfer coefficient	$\mathbf{k_L}$	1.65	$\times 10^{-2}$ cm/s	1.56 to 1.72
Solid side: H_2/HGO mass transfer coefficient	$\mathbf{k_S}$	4.95	$\times 10^{-1}$ cm/s	4.48 to 5.42
Overall mass transfer coefficient	$\mathbf{k_{OVR}}$	1.59	$\times 10^{-2}$ cm/s	1.51 to 1.67
Rate of H_2 consumption for the HDS reaction	$\mathbf{(x_{HDS}\cdot r_{HDS})/V_C}$	2.32	$\times 10^{-4}$ mol·H_2/(s·cc)	1.95 to 2.72
Rate of H_2 consumption for the HDN reaction	$\mathbf{(x_{HDN}\cdot r_{HDN})/V_C}$	8.31	$\times 10^{-4}$ mol·H_2/(s·cc)	6.45 to 10.1
Satterfield's criterion for HDS, left-side value	$\mathbf{S_{HDS}}$	4.56	$\times 10^{-4}$	3.89 to 5.43
Satterfield's criterion for HDN, left-side value	$\mathbf{S_{HDN}}$	1.87	$\times 10^{-4}$	1.61 to 2.53

APPENDIX E:

Evaluating the internal mass transfer resistances for the HDS & HDN reactions

The preliminary calculations performed as part of this evaluation was to see if isothermality could be assumed within the catalyst pellets. The determination of each pellet's degree of isothermality was performed in two ways: by finding both the highest potential temperature rise between the core and the surface of the pellet (Fogler, 2006), as well as by confirming Anderson's criterion (1963).

Maximum temperature rise (ΔT_{MAX}):

$$\beta = \frac{\Delta T_{MAX}}{T_S} = \frac{\Delta H_{R,i} \cdot D_i \cdot [C_i]_S}{k_t \cdot T_S} \qquad [E.1]$$

The variables are defined as:

$\Delta H_{R,i}$ = Heat of HDS/HDN reaction, kJ/mol

$[C_i]_S$ = Catalyst surface concentration of sulfur/nitrogen species, mol/mL

k_t = Thermal conductivity of the FeW/SBA-15 catalyst pellet.

k_t = 0.17 W/(cm·K) (assuming a pure SBA-15 pellet;

[http://eetd.lbl.gov/ecs/aerogels/sa-thermal.html, accessed February, 2011])

T_S = Pellet surface temperature = 648.15 K to 673.15 K (reaction temperatures)

Calculation of the HDS/HDN heats of reaction:

The hydrodesulfurization heat of reaction for heavy gas oil from Athabasca bitumen was approximated by using the heat of reaction range for most thiophene molecules; 63 to 66 kJ/mol of hydrogen consumed (Ancheyta and Speight, 2007). The hydrodenitrogenation heat of reaction for HGO from Athabasca bitumen was

approximated by using the heat of reaction range for most quinoline molecules; 65 to 68 kJ/mol of hydrogen consumed (Satterfield and Cocchetto, 1981). These values were converted to units of kJ/mol of sulfur/nitrogen removed by using the stoichiometric coefficients (x_{HDS} and x_{HDN}) discussed in Appendix D.

$\Delta H_{R,HDS}$ = 63 to 66 kJ/mol of H_2 consumed

$\Delta H_{R,HDS}$ = 252 to 264 kJ/mol of sulfur

$\Delta H_{R,HDN}$ = 65 to 68 kJ/mol of H_2 consumed

$\Delta H_{R,HDN}$ = 260 to 272 kJ/mol of nitrogen

Calculating the effective diffusivities of organosulfur and organonitrogen compounds in HGO ($[D_S]_E/[D_N]_E$):

The effective diffusivity of sulfur compounds was estimated by the following equation:

$$\left[D_i\right]_E = \frac{\varepsilon_P \cdot D_i}{\gamma_P} \qquad \text{[E.2]}$$

The variables are defined as:

ε_P = Porosity of the catalyst pellets

γ_P = Tortuosity of the catalyst pellets

D_i = Bulk diffusivity of organosulfur compounds, cm^2/g

A correlation by Probst and Wohlfahrt (1979) was used to find the ratio of porosity and tortuosity of pelletized catalysts:

$$\frac{\varepsilon_P}{\gamma_P} = \left[\frac{{\varepsilon_P}^m}{\left(2-\varepsilon_P\right)^{m+1}}\right] \qquad \text{[E.3]}$$

Values of ***m*** were found to range from 0.70 to 1.65 for porous compressed catalysts (group D). It was recommended to use an ***m*** value of 1.05 when not otherwise determined (Wijngaarden et al., 1998). Porosity values were found to range from 0.05 to 0.65 (average value was used, 0.35). Based on these conditions, the porosity/tortuosity values were found:

$$\frac{\varepsilon_P}{\gamma_P} = 0.1190 \quad (0.0012 \text{ to } 0.4441)$$

Calculating the bulk diffusivities of organosulfur and organonitrogen compounds in HGO (D_S/D_N):

The assumption was made that the organosulfur and organonitrogen compounds held the same density, average boiling point, average molecular weight and average molar volume as the heavy gas oil feedstock. The bulk diffusivities of each species were found using the Tyn-Calus correlation (Reid et al., 1987):

$$D_i = \left(8.93\times10^{-8}\right)\cdot\left(\frac{v_L^{\,0.267}}{v_i^{\,0.433}}\right)\cdot\left(\frac{T}{\mu_L}\right) = \left(8.93\times10^{-8}\right)\cdot\left(\frac{T}{\mu_L\cdot v_i^{\,0.166}}\right) \quad \text{[E.4]}$$

The variables are defined as:

T = Operating temperature = 643 K to 693 K

μ_L = HGO viscosity at operating conditions = 2.809 cP to 2.319 cP (see Appendix D)

v_i = Molar volume of sulfur/nitrogen molecules under standard conditions, mL/mol

v_L = Molar volume of HGO under standard conditions = 2802.61 mL/mol

The molar volume of the gas oil was found by the following:

$$v_i = (0.285) \cdot v_C^{1.048} \qquad \text{[E.5]}$$

v_C = Critical specific molar volume of HGO, mL/mol

The critical specific molar volume is given by:

$$v_C = v_C^m \cdot M_{AVE} \qquad \text{[E.6]}$$

M_{AVE} = 2867.1 g/mol (determined in Appendix D)

v_C^m = Critical specific mass volume, mL/g

The critical specific mass volume of liquid was calculated using a correlation by Raizi and Daubert (Ahmed, 1989):

$$v_C^m = (7.5214 \times 10^{-3}) \cdot T_b^{0.2896} \cdot SG^{-0.7666} \qquad \text{[E.7]}$$

The variables are defined as:

v_C^m = Critical specific mass volume, ft^3/lb

T_b = Average boiling point temperature = 370°C = 1158°R

$SG_{15.6}$ = Specific gravity at 15.6°C = 1.023

These values lead to the following results:

$v_C^m = 5.70 \times 10^{-2}$ mL/g

v_C = 163.46 mL/mol

v_i = 59.49 mL/mol

$D_i = D_S = D_N = 4.56 \times 10^{-5}$ cm^2/g to 5.76×10^{-5} cm^2/g

$[D_S]_E = [D_N]_E = 5.42 \times 10^{-6}$ cm^2/g to 6.86×10^{-6} cm^2/g

The effective diffusivity values lead to isothermality ratios of:

$\boldsymbol{\beta_{HDS}} = 2.78\times10^{-5}$ to 3.59×10^{-5}

$\boldsymbol{\beta_{HDN}} = 4.67\times10^{-5}$ to 4.74×10^{-5}

Because the HDS and HDN reactions are occurring simultaneously, the sum of the beta values would give the overall maximum temperature change with respect to the catalyst surface temperature. This gives a highest possible $\boldsymbol{\Delta T_{MAX}}$ value of 0.018 K, which can be considered negligible.

Anderson's Criterion:

$$\frac{\left|\Delta H_{R,i}\right| \cdot \{R_i\} \cdot d_P^{\,2}}{k_t \cdot T_S} < \frac{3 \cdot T_S \cdot R}{E_i} \qquad \text{[E.8]}$$

The variables are defined as:

$\boldsymbol{\{R_i\}}$ = Global reaction rate: HDS/HDN, mol/(s·mL)

$\boldsymbol{k_t}$ = Catalyst thermal conductivity = 0.17 W/(cm·K)

$\boldsymbol{R}$ = Universal gas constant = 8.314 J/(mol·K)

$\boldsymbol{E_i}$ = Energy of activation: HDS/HDN, J/mol

The range of operating conditions tested, the values for the left and right hand side of Anderson's criterion were as follows:

Left hand side of Anderson's criterion (HDS) = 1.32×10^{-4} to **1.77×10^{-4}**

Right hand side of Anderson's criterion (HDS) = 1.25×10^{-1} to **1.30×10^{-1}**

Left hand side of Anderson's criterion (HDN) = 5.63×10^{-5} to **8.49×10^{-5}**

Right hand side of Anderson's criterion (HDN) = 9.75×10^{-2} to **1.02×10^{-1}**

The results confirm that isothermal behavior can be assumed when examining the internal mass transfer resistances of the hydrotreating process. Table E.1 at the end of this appendix provides a summary of the pertinent parameters and results of the catalyst pellet isothermality study.

Calculation of Φ:

A dimensionless modulus (Φ), analogous to the Thiele modulus found without knowledge of the intrinsic reaction rate, was found for each collected sample in the kinetic study. The dimensionless modulus was used to represent an estimation of the pore diffusion resistance (Satterfield, 1970):

$$\Phi = \frac{{d_P}^2}{4 \cdot [D_i]_E} \cdot \frac{\{R_i\}}{[C_i]_S} \qquad [E.9]$$

The variables are defined as:

d_P = Average diameter of the catalyst particles = 0.17 cm

$\{R_i\}$ = Global reaction rate: HDS/HDN, mol/(s·mL)

$[D_i]_E$ = Effective diffusivity of sulfur/nitrogen compounds, cm^2/g

$[C_i]_S$ = Catalyst surface concentration of sulfur/nitrogen species, mol/mL

The change in the global reaction rate and the change in surface concentration of sulfur and nitrogen heteroatoms allow the dimensionless modulus to be calculated at both the inlet and outlet of the reactor. In finding the dimensionless modulus, a rough approximation of the effectiveness factor (η) could be determined by applying the following equations in unison (Satterfield, 1970):

$$\Phi = (\phi)^2 \cdot \eta \qquad [E.10]$$

$$\eta = \frac{3}{\phi}\left[\frac{1}{\tanh(\phi)} - \frac{1}{\phi}\right] \qquad \text{[E.11]}$$

Solving for the effectiveness factor using equations [E.10] and [E.11] will only provide a rough estimate of both η and φ, the true Thiele modulus. This is because equation E.10 only applies to integer-power rate equations for spherical catalyst pellets. Additionally, equation E.11 only applies to isothermal first-order reactions for spherical catalysts. Nonetheless, these equations provide a measure of comparison between the effectiveness factors for each collected sample.

Table E.2 provides a summary of all the dimensionless modulus values for the inlet and outlet ($[\Phi_O]_S$ and $[\Phi_P]_S$), as well as all the determined effectiveness factors ($[\eta_O]_S$ and $[\eta_P]_S$), for the hydrodesulfurization kinetic study.

Table E.3 provides a summary of all the dimensionless modulus values for the inlet and outlet ($[\Phi_O]_N$ and $[\Phi_P]_N$), as well as all the determined effectiveness factors ($[\eta_O]_N$ and $[\eta_P]_N$), for the hydrodenitrogenation kinetic study.

Table E.1
Summary of the isothermality study performed for FeW/SBA-15 catalyst pellets loaded in a trickle bed hydrotreating reactor.

Parameter	Symbol	Value	Units	Range
Pressure	P	8.8	MPa	7.6 to 10
Temperature	T	388	°C	375 to 400
Average boiling point temperature of HGO	T_b	698	°F	-
Liquid hourly space velocity	$LHSV$	1.0	h^{-1}	0.5 to 2.0
Feed flow rate	L	5.0	g/h	2.5 to 10.0
Particle size	d_P	0.17	cm	-
HGO viscosity at operating temperature	μ_L	2.926	cP	2.809 to 2.319
Critical molar volume of HGO molecules	v_L	2802.61	cc/mol	-
Heat of HDS reaction	ΔH_{HDS}	258	kJ/mol	252 to 264
Heat of HDN reaction	ΔH_{HDN}	266	kJ/mol	260 to 272
Effective diffusivity of sulphur	$(D_E)_S$	6.14	$\times 10^{-6} cm^2/s$	5.42 to 6.86
Effective diffusivity of nitrogen	$(D_E)_N$	6.14	$\times 10^{-6} cm^2/s$	5.42 to 6.86
Porosity of catalyst pellet	ε_P	0.35	-	0.05 to 0.65
Parameter m (Probst and Wohlfahrt, 1979)	m	1.05	-	0.70 to 1.65
Porosity/tortuosity ratio	ε_P/γ_P	0.119	-	0.444 to 1.20×10^{-3}
Diffusivity of sulfur compounds	D_S	5.16	$\times 10^{-5} cm^2/s$	4.56 to 5.76
Diffusivity of nitrogen compounds	D_N	5.16	$\times 10^{-5} cm^2/s$	4.56 to 5.76
Surface concentration in HGO	$C_{S,S}$	1.77	$\times 10^{-4}$mol/cc	2.06 to 1.20
Surface concentration in HGO	$C_{N,S}$	0.251	$\times 10^{-4}$mol/cc	0.26 to 0.20
Thermal conductivity of SBA-15 catalyst pellet	k_t	0.17	J/(cm·K)	0.14 to 0.35
Activation energy of HDS	E_{HDS}	129.6	kJ/mol	125.7 to 133.6
Activation energy of HDN	E_{HDN}	165.8	kJ/mol	160.8 to 170.9
β value for HDS	β_{HDS}	3.12	$\times 10^{-5}$	2.78 to 3.59
β value for HDN	β_{HDN}	2.95	$\times 10^{-5}$	4.60 to 4.74
Global rate of HDS reaction	$\{R_{HDS}\}$	2.08	$\times 10^{-3}$mol/s.cc	1.95 to 2.19
Global rate of HDN reaction	$\{R_{HDN}\}$	8.56	$\times 10^{-4}$mol/s.cc	8.10 to 8.60
Anderson's criterion, left-side value (HDS)	$(A_{HDS})_{LEFT}$	1.49	$\times 10^{-4}$	1.32 to 1.77
Anderson's criterion, right-side value (HDS)	$(A_{HDS})_{RIGHT}$	0.127	-	0.125 to 0.131
Anderson's criterion, left-side value (HDN)	$(A_{HDN})_{LEFT}$	6.76	$\times 10^{-5}$	5.63 to 8.49
Anderson's criterion, right-side value (HDN)	$(A_{HDN})_{RIGHT}$	0.935	-	0.0975 to 0.102

Table E.2
Summary of the dimensionless modulus values and effectiveness factors for the internal mass transfer resistances study of HGO hydrodesulfurization.

Run time (days)	T (ºC)	LHSV (h^{-1})	P (MPa)	G/L (mL/mL)	$[\Phi_0]_{HDS}$	$[\Phi_P]_{HDS}$	$[\eta_0]_{HDS}$	$[\eta_P]_{HDS}$
1	375	1.0	8.8	600	0.671	0.931	0.804	0.637
2	375	1.0	8.8	600	0.513	0.820	0.936	0.921
3	375	1.0	8.8	600	0.437	0.728	0.953	0.988
4	375	1.0	8.8	600	0.441	0.742	0.952	0.984
5	375	1.0	8.8	600	0.426	0.694	0.955	0.999
6	375	1.0	8.8	600	0.609	1.353	0.913	0.848
7	375	1.0	8.8	600	0.651	1.531	0.903	0.819
8	388	1.0	8.8	600	0.713	1.801	0.886	0.743
9	388	1.0	8.8	600	0.737	1.911	0.880	0.728
10	388	1.0	8.8	600	0.745	1.950	0.878	0.724
11	400	1.0	8.8	600	0.926	1.417	0.827	0.600
12	400	1.0	8.8	600	0.700	1.092	0.697	0.448
13	400	1.0	8.8	600	0.668	1.018	0.713	0.464
14	375	1.0	8.8	600	0.324	1.517	0.903	0.821
15	375	1.0	8.8	600	0.301	1.326	0.915	0.852
16	375	1.0	8.8	600	0.312	1.417	0.909	0.837
17	388	0.5	8.8	600	0.478	0.996	0.819	0.378
18	388	0.5	8.8	600	0.503	1.085	0.804	0.363
19	388	0.5	8.8	600	0.545	1.237	0.780	0.340

20	388	1.5	8.8	600	0.526	1.168	0.791	0.749
21	388	1.5	8.8	600	0.514	1.125	0.798	0.759
22	388	1.5	8.8	600	0.486	1.025	0.814	0.784
23	388	2.0	8.8	600	0.378	1.995	0.875	0.872
24	388	2.0	8.8	600	0.369	1.912	0.880	0.881
25	388	2.0	8.8	600	0.365	1.881	0.882	0.884
26	388	1.0	7.6	600	0.227	0.783	0.949	0.938
27	388	1.0	7.6	600	0.206	0.652	0.957	0.980
28	388	1.0	7.6	600	0.188	0.545	0.964	0.874
29	388	1.0	8.3	600	0.502	1.080	0.805	0.602
30	388	1.0	8.3	600	0.448	1.343	0.835	0.647
31	388	1.0	8.3	600	0.435	1.273	0.843	0.660
32	388	1.0	9.6	600	0.829	1.163	0.634	0.421
33	388	1.0	9.6	600	0.838	1.011	0.630	0.418
34	388	1.0	9.6	600	0.787	1.079	0.654	0.438
35	388	1.0	8.8	400	0.234	0.828	0.946	0.925
36	388	1.0	8.8	400	0.250	0.936	0.939	0.897
37	388	1.0	8.8	400	0.268	1.071	0.931	0.866
38	388	1.0	8.8	800	0.480	1.006	0.817	0.619
39	388	1.0	8.8	800	0.498	1.067	0.807	0.605
40	388	1.0	8.8	800	0.505	1.093	0.803	0.599
41	388	1.0	8.8	1000	0.784	1.074	0.655	0.440
42	388	1.0	8.8	1000	0.714	1.126	0.689	0.471

43	388	1.0	8.8	1000	0.692	1.075	0.701	0.482
Run time (days)	**T (ºC)**	**LHSV (h^{-1})**	**P (MPa)**	**G/L (mL/mL)**	**$[\Phi_0]_{HDS}$**	**$[\Phi_P]_{HDS}$**	**$[\eta_0]_{HDS}$**	**$[\eta_P]_{HDS}$**
1	388	1.0	8.8	600	0.430	1.253	0.845	0.663
2	388	1.0	8.8	600	0.406	1.134	0.859	0.687
3	388	1.0	8.8	600	0.393	1.070	0.866	0.701
4	388	1.0	8.8	600	0.402	1.113	0.861	0.692
5	388	1.0	8.8	600	0.402	1.112	0.862	0.692
6	388	1.0	8.8	600	0.394	1.074	0.866	0.700
7	388	1.0	8.8	600	0.413	1.166	0.855	0.681
8	388	1.0	8.8	600	0.418	1.193	0.852	0.675
9	388	1.0	8.8	600	0.405	1.126	0.860	0.689
10	388	1.0	8.8	600	0.401	1.110	0.862	0.693
11	388	1.0	8.8	600	0.401	1.106	0.862	0.693
12	388	1.0	8.8	600	0.408	1.142	0.858	0.686
13	388	1.0	8.8	600	0.392	1.068	0.867	0.702
14	388	1.0	8.8	600	0.390	1.055	0.868	0.705
15	388	1.0	8.8	600	0.407	1.138	0.859	0.687
16	388	1.0	8.8	600	0.391	1.061	0.867	0.703
17	388	1.0	8.8	600	0.386	1.035	0.870	0.709
18	388	1.0	8.8	600	0.405	1.129	0.860	0.688
19	388	1.0	8.8	600	0.419	1.196	0.852	0.675
20	388	1.0	8.8	600	0.375	0.983	0.877	0.722
21	388	1.0	8.8	600	0.428	1.241	0.847	0.666

22	388	1.0	8.8	600	0.396	1.084	0.865	0.698
23	388	1.0	8.8	600	0.412	1.160	0.856	0.682
24	388	1.0	8.8	600	0.425	1.225	0.849	0.669
25	388	1.0	8.8	600	0.393	1.071	0.866	0.701
26	388	1.0	8.8	600	0.408	1.141	0.858	0.686
27	388	1.0	8.8	600	0.396	1.086	0.865	0.698
28	388	1.0	8.8	600	0.403	1.119	0.861	0.691
29	388	1.0	8.8	600	0.394	1.075	0.866	0.700
30	388	1.0	8.8	600	0.377	0.993	0.875	0.719
31	388	1.0	8.8	600	0.416	1.181	0.854	0.678
32	388	1.0	8.8	600	0.382	1.017	0.873	0.713
33	388	1.0	8.8	600	0.395	1.080	0.865	0.699
34	388	1.0	8.8	600	0.381	1.012	0.873	0.715
35	388	1.0	8.8	600	0.429	1.247	0.846	0.665
36	388	1.0	8.8	600	0.401	1.109	0.862	0.693
37	388	1.0	8.8	600	0.406	1.134	0.859	0.687
38	388	1.0	8.8	600	0.419	1.198	0.852	0.674
39	388	1.0	8.8	600	0.395	1.081	0.865	0.699
40	388	1.0	8.8	600	0.401	1.110	0.862	0.693
41	388	1.0	8.8	600	0.405	1.127	0.860	0.689
42	388	1.0	8.8	600	0.412	1.162	0.856	0.681
43	388	1.0	8.8	600	0.398	1.093	0.864	0.696
44	388	1.0	8.8	600	0.383	1.022	0.872	0.712

45	388	1.0	8.8	600	0.403	1.117	0.861	0.691
46	388	1.0	8.8	600	0.414	1.171	0.855	0.680
47	388	1.0	8.8	600	0.362	0.925	0.883	0.736
48	388	1.0	8.8	600	0.407	1.139	0.858	0.686
49	388	1.0	8.8	600	0.397	1.090	0.864	0.697
50	388	1.0	8.8	600	0.380	1.007	0.874	0.716
51	388	1.0	8.8	600	0.427	1.236	0.847	0.667
52	388	1.0	8.8	600	0.392	1.064	0.867	0.703
53	388	1.0	8.8	600	0.435	1.277	0.843	0.659
54	388	1.0	8.8	600	0.391	1.062	0.867	0.703
55	388	1.0	8.8	600	0.397	1.091	0.864	0.697
56	388	1.0	8.8	600	0.408	1.141	0.858	0.686
57	388	1.0	8.8	600	0.380	1.007	0.874	0.716
58	388	1.0	8.8	600	0.395	1.080	0.865	0.699
59	388	1.0	8.8	600	0.390	1.054	0.868	0.705
60	388	1.0	8.8	600	0.406	1.131	0.859	0.688

Table E.3
Summary of the dimensionless modulus values and effectiveness factors for the internal mass transfer resistances study of HGO hydrodenitrogenation.

Run time (days)	T (ºC)	LHSV (h^{-1})	P (MPa)	G/L (mL/mL)	$[\Phi_0]_{HDN}$	$[\Phi_P]_{HDN}$	$[\eta_0]_{HDN}$	$[\eta_P]_{HDN}$
1	375	1.0	8.8	600	0.613	0.946	0.804	0.291
2	375	1.0	8.8	600	0.429	0.907	0.935	0.393
3	375	1.0	8.8	600	0.377	0.871	0.981	0.437
4	375	1.0	8.8	600	0.285	0.820	0.857	0.538
5	375	1.0	8.8	600	0.281	0.803	0.861	0.544
6	375	1.0	8.8	600	0.254	0.704	0.885	0.581
7	375	1.0	8.8	600	0.300	0.876	0.845	0.519
8	388	1.0	8.8	600	0.272	0.769	0.855	0.556
9	388	1.0	8.8	600	0.263	0.738	0.863	0.568
10	388	1.0	8.8	600	0.281	0.803	0.847	0.544
11	400	1.0	8.8	600	0.342	0.884	0.775	0.471
12	400	1.0	8.8	600	0.510	0.832	0.652	0.341
13	400	1.0	8.8	600	0.488	0.790	0.666	0.354
14	375	1.0	8.8	600	0.275	0.780	0.867	0.552
15	375	1.0	8.8	600	0.263	0.737	0.877	0.568
16	375	1.0	8.8	600	0.273	0.775	0.868	0.554
17	388	0.5	8.8	600	0.308	0.907	0.821	0.508
18	388	0.5	8.8	600	0.465	0.895	0.703	0.369
19	388	0.5	8.8	600	0.471	0.910	0.699	0.364

20	388	1.5	8.8	600	0.206	0.786	0.924	0.661
21	388	1.5	8.8	600	0.181	0.652	0.952	0.708
22	388	1.5	8.8	600	0.217	0.850	0.911	0.641
23	388	2.0	8.8	600	0.174	0.612	0.961	0.722
24	388	2.0	8.8	600	0.183	0.660	0.950	0.705
25	388	2.0	8.8	600	0.157	0.522	0.982	0.757
26	388	1.0	7.6	600	0.074	0.566	0.811	0.927
27	388	1.0	7.6	600	0.072	0.548	0.813	0.929
28	388	1.0	7.6	600	0.072	0.542	0.813	0.930
29	388	1.0	8.3	600	0.182	0.875	0.938	0.706
30	388	1.0	8.3	600	0.213	0.827	0.902	0.648
31	388	1.0	8.3	600	0.171	0.800	0.951	0.727
32	388	1.0	9.6	600	0.301	0.880	0.851	0.517
33	388	1.0	9.6	600	0.288	0.829	0.863	0.534
34	388	1.0	9.6	600	0.354	0.922	0.808	0.459
35	388	1.0	8.8	400	0.158	0.850	0.980	0.753
36	388	1.0	8.8	400	0.174	0.981	0.961	0.722
37	388	1.0	8.8	400	0.162	0.880	0.975	0.746
38	388	1.0	8.8	800	0.355	0.812	0.782	0.457
39	388	1.0	8.8	800	0.357	0.817	0.780	0.455
40	388	1.0	8.8	800	0.355	0.812	0.782	0.457
41	388	1.0	8.8	1000	0.413	0.975	0.738	0.406
42	388	1.0	8.8	1000	0.488	0.948	0.688	0.354

43	388	1.0	8.8	1000	0.454	0.872	0.710	0.376
Run time (days)	**T (° C)**	**LHSV (h^{-1})**	**P (MPa)**	**G/L (mL/mL)**	**$[\Phi_0]_{HDN}$**	**$[\Phi_P]_{HDN}$**	**$[\eta_0]_{HDN}$**	**$[\eta_P]_{HDN}$**
1	388	1.0	8.8	600	0.219	0.858	0.682	0.638
2	388	1.0	8.8	600	0.207	0.794	0.692	0.659
3	388	1.0	8.8	600	0.193	0.719	0.703	0.684
4	388	1.0	8.8	600	0.206	0.790	0.692	0.660
5	388	1.0	8.8	600	0.190	0.701	0.706	0.690
6	388	1.0	8.8	600	0.204	0.777	0.694	0.664
7	388	1.0	8.8	600	0.212	0.821	0.687	0.650
8	388	1.0	8.8	600	0.201	0.764	0.696	0.669
9	388	1.0	8.8	600	0.205	0.783	0.693	0.663
10	388	1.0	8.8	600	0.204	0.775	0.695	0.665
11	388	1.0	8.8	600	0.197	0.742	0.700	0.676
12	388	1.0	8.8	600	0.180	0.649	0.715	0.709
13	388	1.0	8.8	600	0.205	0.784	0.693	0.662
14	388	1.0	8.8	600	0.217	0.850	0.683	0.641
15	388	1.0	8.8	600	0.213	0.827	0.687	0.648
16	388	1.0	8.8	600	0.211	0.814	0.689	0.652
17	388	1.0	8.8	600	0.202	0.764	0.696	0.669
18	388	1.0	8.8	600	0.222	0.878	0.679	0.632
19	388	1.0	8.8	600	0.214	0.834	0.686	0.646
20	388	1.0	8.8	600	0.197	0.737	0.700	0.678
21	388	1.0	8.8	600	0.208	0.801	0.691	0.657

22	388	1.0	8.8	600	0.198	0.747	0.699	0.674
23	388	1.0	8.8	600	0.210	0.811	0.689	0.653
24	388	1.0	8.8	600	0.204	0.777	0.694	0.665
25	388	1.0	8.8	600	0.178	0.635	0.717	0.714
26	388	1.0	8.8	600	0.191	0.704	0.706	0.689
27	388	1.0	8.8	600	0.198	0.742	0.700	0.676
28	388	1.0	8.8	600	0.191	0.705	0.706	0.689
29	388	1.0	8.8	600	0.207	0.797	0.691	0.658
30	388	1.0	8.8	600	0.192	0.713	0.704	0.686
31	388	1.0	8.8	600	0.212	0.822	0.687	0.650
32	388	1.0	8.8	600	0.179	0.640	0.716	0.712
33	388	1.0	8.8	600	0.209	0.807	0.690	0.655
34	388	1.0	8.8	600	0.205	0.785	0.693	0.662
35	388	1.0	8.8	600	0.194	0.720	0.703	0.684
36	388	1.0	8.8	600	0.215	0.839	0.685	0.644
37	388	1.0	8.8	600	0.205	0.784	0.693	0.662
38	388	1.0	8.8	600	0.212	0.821	0.687	0.650
39	388	1.0	8.8	600	0.206	0.786	0.693	0.661
40	388	1.0	8.8	600	0.220	0.863	0.681	0.637
41	388	1.0	8.8	600	0.214	0.832	0.686	0.647
42	388	1.0	8.8	600	0.204	0.780	0.694	0.664
43	388	1.0	8.8	600	0.211	0.814	0.689	0.652
44	388	1.0	8.8	600	0.206	0.788	0.693	0.661

45	388	1.0	8.8	600	0.222	0.878	0.679	0.632
46	388	1.0	8.8	600	0.199	0.748	0.699	0.674
47	388	1.0	8.8	600	0.184	0.669	0.711	0.702
48	388	1.0	8.8	600	0.209	0.807	0.690	0.655
49	388	1.0	8.8	600	0.216	0.846	0.684	0.642
50	388	1.0	8.8	600	0.213	0.826	0.687	0.649
51	388	1.0	8.8	600	0.205	0.782	0.694	0.663
52	388	1.0	8.8	600	0.208	0.798	0.691	0.657
53	388	1.0	8.8	600	0.186	0.681	0.709	0.697
54	388	1.0	8.8	600	0.187	0.686	0.709	0.696
55	388	1.0	8.8	600	0.214	0.831	0.686	0.647
56	388	1.0	8.8	600	0.209	0.803	0.690	0.656
57	388	1.0	8.8	600	0.203	0.772	0.695	0.666
58	388	1.0	8.8	600	0.217	0.852	0.683	0.641
59	388	1.0	8.8	600	0.191	0.705	0.706	0.689
60	388	1.0	8.8	600	0.189	0.693	0.707	0.693